2016

Theory and Utility of the Three Isotope Fractionation Relationship

Justin Alan Hayles
Louisiana State University and Agricultural and Mechanical College

Theory and Utility of the Three Isotope Fractionation Relationship

A dissertation

Submitted to the Graduate Faculty of the
Louisiana State University and
Mechanical College
in partial fulfillment of the
requirements of the degree of
Doctor of Philosophy

in

Department of Geology and Geophysics

by
Justin Alan Hayles
B.S. University of South Alabama, 2010
M.S. Louisiana State University, 2013
July 2016

ACKNOWLEDGEMENTS

Special thanks to my advisor, Dr. Huiming Bao, and committee members, Dr. Jianwei Wang, Dr. Darrell Henry, Dr. Michael Polito, and Dr. Yun Liu for all of their support and expertise in this endeavor. Without Dr. Bao's constant support and diligent mentorship, this dissertation never would have come to fruition.

Very special thanks to my family and friends who made this experience easier. I am very grateful for wife, Jie Shen, for her love, patience, and support through the thick and thin of graduate school as well as listening to me while I rambled about isotopes.

I would like to thank the members of OASIC, past and present. Specifically, I would like to thank Xiaobin Cao, for being patient with me while I learned the theory necessary for this work, Bryan Killingsworth for being a friend, and collaborator while always having free time to give me advice, Tao Sun for guiding me through the first year of my graduate studies and Ziran Wei for the many discussions and for dragging me out of the lab from time to time.

Special thanks to LSU Department of Geology and Geophysics, for their active support of graduate student research.

TABLE OF CONTENTS

ABSTRACT

The field of isotope geochemistry began with the study of oxygen isotope geothermometry, most famously for carbonates. Traditionally oxygen isotope studies are only concerned with the relationship between one rare isotope, oxygen-18, and the common isotope, oxygen-16. In these cases, the abundance of the third stable isotope, oxygen-17 is ignored because for almost all terrestrial processes the ^{17}O-^{16}O relationship roughly scales with the ^{18}O-^{16}O relationship through a fractionation processes and is thought to not provide any new information. However, the discovery of large "mass independent" isotope effects for ozone chemistry has driven a multitude of uses for triple isotope relationships. Triple stable isotope relationships have found uses including, but not limited to, in geochemistry to determine ancient atmospheric pCO_2, atmospheric chemistry to understand the details of ozone cycling, and biochemistry to study enzymatic pathways. These uses rely on a component of "mass-independent" isotope fractionation, previously described by deviation from a "canonical" range of mass-fractionation exponent values. However, recent advances in analytical techniques and precision have allowed for the measurement of small mass dependent variations in three isotope composition that hold information not present in the two isotope composition. The purpose of this work is to re-investigate the generic theoretical boundaries of mass-dependent variations in three isotope composition through fractionation processes and to demonstrate the utility of mass-dependent isotope fractionation.

In the first study presented here, the boundaries and behaviors of mass-dependent isotope fractionation are investigated from a theoretical perspective. Previous approximations to the statistical-mechanical models for predicting isotope effects have led to the notion that mass

fractionation laws are constant, and later, constrained to a "canonical" range of possible values. Despite previous work indicating that these mass fractionation exponents can be highly variable, the concept of a constant relationship remains common. In the first study presented here, it is demonstrated generically that the mass fractionation exponent, θ, can take *any* value for small fractionations, that these deviations are measurable and that the half-reaction mass fractionation exponent, κ, is bounded by upper and lower limits to a close approximation. In addition, we characterize and advocate the use of $\Delta\Delta^{\ddagger}M$ or "change/difference in cap-delta" as a necessary and more reliable descriptor of multiple isotope fractionation relationships. Deviations from the "canonical" range are demonstrated by experimental data in the geochemically relevant hematite-water system. The results of this work are valid for any element where nuclear volume effects are not significant.

In the second study presented here, theoretical calculations for both two and three isotope fractionations between several common minerals and liquid water are presented for the purpose of calibration the three oxygen isotope geothermometer. The three isotope geothermometer concept used here is applied similarly to the more common two oxygen isotope thermometer, but utilizes a somewhat independent assumption. For mineral-water equilibrium systems, because the two-isotope and three-isotope geothermometers can be treated somewhat independently, there is potential to constrain the isotope composition of water with a single analysis. Alternately, without the assumption of equilibrium, the three isotope composition can be used as a test for equilibrium for the more accurate two isotope thermometer. In this study, new theoretical calibrations are presented for both the traditional two-isotope and the recently introduced three-isotope thermometer for pairs of quartz, calcite, dolomite, fluorapatite, hematite, magnetite and liquid water. The results presented here compare well with previous

studies on $^{18}O/^{16}O$ fractionation where data is available. Of the models given here, pairs of quartz, calcite, dolomite and fluorapatite with water, hematite and magnetite show promise as three isotope thermometers with acceptable uncertainties for surface and low-T hydrothermal environments. As an example, the new quartz-water fractionation curves are applied to triple oxygen isotope date from previously published 2.5 Ga marine chert samples. These results indicate that the water which those chert samples formed from had a temperature of < 1°C and a $\delta'^{18}O$ of < -23.8‰.

In the third study presented here, isotope fractionations associated with two key processes for ceria, an important industrial catalyst, are measured using constraints on triple oxygen isotope fractionation. Ceria (CeO_2) is a heavily studied material in catalytic chemistry for use as an oxygen storage medium, oxygen partial pressure regulator, fuel additive, and for the production of syngas, among other applications. Ceria powders are readily reduced and lose structural oxygen when subjected to low pO_2 and/or high temperature conditions. Such dis-stoichiometric ceria can then re-oxidize under higher pO_2 and/or lower temperature by incorporating new oxygen into the previously formed oxygen site vacancies. Despite extensive studies on ceria, the mechanisms for oxygen adsorption-desorption, dissociation-association, and diffusion of oxygen species on ceria surface and within the crystal structure are not well known. We predict that a large kinetic oxygen isotope effect should accompany the release and incorporation of ceria oxygen. As the first attempt to determine the existence and the magnitude of the isotope effect, this study focuses on a set of simple room-temperature re-oxidation experiments that are also relevant to a laboratory procedure using ceria to measure the triple oxygen isotope composition of CO_2. Triple-oxygen-isotope labeled ceria powders are heated at 700°C and cooled under vacuum prior to exposure to air. By combining results from independent

experimental sets with different initial oxygen isotope labels and using a combined mass-balance and triangulation approach, we have determined the isotope fractionation factors for both high temperature reduction in vacuum (~10^{-4} mbar) and room temperature re-oxidation in air. Results indicate that there is a 1.5‰±0.8‰ increase in the $\delta^{18}O$ value of ceria after being heated in vacuum at 700°C for one hour. When the vacuum is broken at room temperature, the previously heated ceria incorporates 3% to 19% of its final structural oxygen from air, with a $\delta^{18}O$ value of 2.1‰ (−4.1‰; +7.7‰) for the incorporated oxygen. The substantial incorporation of oxygen from air supports that oxygen mobility is high in vacancy-rich ceria during re-oxidation at room temperature. The quantified oxygen isotope fractionation factors are consistent with the dissociation of O2 and association of atomic oxygen species at the surface of ceria being the main rate-limiting steps during ceria oxidation and reduction, respectively. While additional parameters may reduce some of the uncertainties in our approach, this study demonstrates that isotope effects can be an encouraging tool for studying oxygen transport kinetics in ceria and other oxides.

CHAPTER 1: STATISTICAL MECHANICAL BASIS OF THE TRIPLE ISOTOPE FRACTIONATION RELATIONSHIP FOR ELEMENTAL PROCESSES

PREFACE

The work presented in Chapter 1 comprises the core of my work at Louisiana State University. This work is a reanalysis of the base concepts in the multidisciplinary field of three isotope relationships. The findings, justified by theory, demonstrate that the previous "canonical" concepts of the field are incorrect. The results given here provide a new and simplified framework for investigating three isotope effects. This work has been accepted in Geochemical Perspectives Letters.

ABSTRACT

Multiple stable isotope relationships have found uses including, but not limited to, in geochemistry to determine ancient atmospheric pCO_2, atmospheric chemistry to understand the details of ozone cycling, and biochemistry to study enzymatic pathways. Approximations to the statistical-mechanical models for predicting isotope effects have led to the notion that mass fractionation laws are constant and later constrained to a "canonical" range of possible values. Despite previous work indicating that these mass fractionation exponents can be highly variable, the concept of a constant relationship remains common. In this study, it is demonstrated generically that the mass fractionation exponent, θ, can take any value for small fractionations, that these deviations are measurable and that the half-reaction mass fractionation exponent, κ, is bounded by upper and lower limits to a close approximation. In addition, we characterize and advocate the use of $\Delta\Delta^{\ddagger}M$ or "change/difference in cap-delta" as a necessary and more reliable

descriptor of multiple isotope fractionation relationships. Deviations from the "canonical" range are demonstrated by experimental data in the geochemically relevant hematite-water system.

1. INTRODUCTION

Despite its roots in physical chemistry, the study of triple isotope relationships has found its most widespread and varied footing in the realm of geochemistry and cosmochemistry. Multiple stable isotope ratios have found utility as tool to elucidate photochemical (Bao et al., 2008; Farquhar et al., 2000) or magnetic isotope effects (Blum et al., 2014), as an identifying marker for extraterrestrial materials (Hulston and Thode, 1965), and as a tracer of hydrogen tunneling (Klinman, 2003). Because of advances in analytical resolution, now more than ever, it is critical to understand the natural range of multiple isotope relationships to further these pursuits. The first accurate model for predicting the separation of isotopes for equilibrium processes was published by Urey (Urey, 1947) and Bigeleisen and Goeppert-Mayer (B-GM-U model) (Bigeleisen and Goeppert-Mayer, 1947). Their development of the concept of the reduced partition function ratio allowed for the calculation, to good approximation, of the isotope fractionation factor (α) for two species using only the harmonic vibrational frequencies for each degree of freedom and temperature.

$$\alpha_{A-B} = \frac{\beta_A}{\beta_B} \quad (1)$$

where A and B indicate different chemical species and θ is the complete half-reaction or one-species fractionation factor representing isotope partitioning for a hypothetical equilibrium between a given species and an unbound atom. For most elements, only molecular vibrations deviate significantly from the classical predictions and these vibrations can be well described as

harmonic. The bulk contribution to isotope partitioning is then expected to be equal to the ratio of the quantum mechanical contributions to the partition function for each isotope or,

$$\beta_h^* = \prod_i^{3n-6(5)} \left(\frac{u_i^*}{u_i}\right)_{TRPR} \left(\frac{e^{-u_i^*/2}}{e^{-u_i/2}}\right)_{ZPE} \left(\frac{1-e^{-u_i}}{1-e^{-u_i^*}}\right)_{EXC} \quad (2)$$

$$u^* = \frac{h\upsilon^*}{k_B T} \quad (3)$$

Here, h is the Planck constant, $k_B T$ is temperature in terms of energy, υ is the harmonic vibrational frequency for a specific vibrational degree of freedom and the product is taken over all vibrational degrees of freedom. The heavy isotope substituted state is indicated by "*" and the lack of a superscript indicates the reference isotope (commonly the most abundant isotope). The harmonic contribution can be separated into the product of three terms: (1) the TRPR term derived from the use of the Teller-Redlich product rule; (2) The zero-point (ZPE) contribution; and (3) non-zero point contributions (EXC) (Wolfsburg, 1972). Importantly, the fractionation factor in equation 2 is modified with a subscript "h" to indicate that this term only represents the contributions to isotope partitioning from the harmonic portions of molecular vibrations. The B-GM-U model has been successful as it gives the dominant contribution to the value of β to a point near or better than analytical precision for most isotope systems. However, for molecules bearing light isotopes, particularly hydrogen, contributions from anharmonicity, non-classical rotations and rotational-vibrational interactions become significant. Modifications of the B-GM-U model in the form of multiplicative terms have been developed to correct these inaccuracies (Richet et al., 1977). Here the term "contribution" is used to specifically indicate multiplicative terms. Each contribution is treated as having its own parameter, such as β, indicated by a subscript which is only a portion of the complete parameter.

2. EXTENSION TO THREE ISOTOPE EFFECTS

Conversion of two isotope model to a three isotope model involves combining two independently calculated models which use the same reference isotope. A key aspect for the B-GM-U model is the mass dependence of isotope fractionation due to the mass dependence of vibrational frequencies. This relationship can be described by an exponent θ where;

$$\theta = \frac{\ln \alpha^{\ddagger}_{A-B}}{\ln \alpha^{*}_{A-B}} \quad (4)$$

where "‡" and "*" indicate the respective parameters for two different isotope ratios of the same element. Due to the use of the "low-u" approximation of equation 2, it was commonly believed that the value of the three isotope exponent was somewhat constant and later thought to be constrained to a finite, canonical, range for mass-dependent processes which remains as an accepted idea (Pack and Herwartz, 2015; Swain et al., 1958; Young et al., 2002; Young et al., 2016). Here, "canonical" refers to a θ value being within certain range represented by most of the observed cases and theoretical justifications (e.g. 0.50-0.5305 for the ^{16}O-^{17}O-^{18}O system).

In 1980, using a theoretical framework which represented strictly mass dependent scenarios Skaron and Wolfsberg (1980) showed theoretically for oxygen isotope partitioning that θ can vary from positive to negative infinity for crossover scenarios, situations where the fractionation factor α transitions from greater than 1 (heavier isotopes partitioned to A) to less than 1 (heavier isotopes partitioned to B) or vise-versa with changing temperature. Studies investigating these scenarios for sulfur (Deines, 2003; Otake et al., 2008) and hydrogen (Kotaka et al., 1992) have come to the same conclusion.

Analogously to the theoretical concept of β, Cao and Liu (2011)first introduced the concept of κ defined as the half-reaction or one species analogue of θ, or:

$$\kappa = \frac{ln\,\beta^{\ddagger}}{\ln \beta^{*}} \qquad (5)$$

where β is the complete half-reaction fractionation factor for the two-isotope relationship. The complete value of κ including corrections can be calculated by:

$$\kappa_{Complete} = \frac{\sum_i \kappa_i ln\beta_i^*}{\sum_i ln\beta_i^*} \qquad (6)$$

where the sums are taken over all contributions whether they are from corrections to the B-GM-U model or from independent vibrational degrees of freedom. As long as all values of $\ln \beta$ have the same sign, the value of κ for a complex molecule is equal to the $\ln \beta$ weighted mean of the κ values from each contribution. The relationship between κ and θ is given by Cao and Liu (2011):

$$\theta = \kappa_A + (\kappa_A - \kappa_B)\frac{\ln \beta_B^*}{\ln \alpha_{A-B}^*} \qquad (7)$$

From equation 6, a large difference in the values of κ between phases A and B allows for a larger potential variability in the value of θ particularly where α is near unity. The only scenario which would not allow the above conditions to occur for any system would be if the values of κ and β were a strict function of one another which could be applied to all species. This hypothetical case is invalid because the relationship between vibrational frequencies of differently substituted molecules is a function of not only the mass of the substituted atom, but also the molecular configuration, bond force constants, and masses of secondary, non-substituted atoms. Interestingly, there is a general, but not strict, relationship between β^* and κ at least for the diatomic special case as shown in Figure 1a for the oxygen triple isotope system. Additional evidence for a non-strict κ - β^* relationship can be found in studies implicating crossovers for θ values approaching infinity (Deines, 2003; Kotaka et al., 1992; Otake et al., 2008). Hirschi and Singleton (2005) additionally showed that deviations from the expected range of θ occur at small values of α for both equilibrium and secondary kinetic isotope effects for hydrogen.

3. THE HARMONIC CONTRIBUTION TO κ

The complete equation for the harmonic contribution to κ for a single degree of freedom is given by;

$$\kappa_h = \frac{(\ln(u^{\ddagger})-\ln(u))_{TRPR}+(u/2-u^{\ddagger}/2)_{ZPE}+(\ln(1-e^{-u})-\ln(1-e^{-u^{\ddagger}}))_{EXC}}{(\ln(u^{*})-\ln(u))_{TRPR}+(u/2-u^{*}/2)_{ZPE}+(\ln(1-e^{-u})-\ln(1-e^{-u^{*}}))_{EXC}} \quad (8)$$

which can be separated into terms that correspond to the contributions from TRPR, ZPE and EXC with each having their own mass dependence. At high temperatures, the terms corresponding to the contribution from energized states (EXC) dominates the harmonic κ. At very high temperatures the values of u become very small and

$$\kappa_{HTL} = \frac{1/m-1/m^{\ddagger}}{1/m-1/m^{*}} \quad (9)$$

which serves as an upper bound of its value for diatomic molecules at all temperatures. At low temperatures, the terms corresponding to the contribution from ZPE dominates the harmonic κ. For a diatomic molecule under these conditions;

$$\kappa_{LT-D} = \frac{1/\sqrt{\mu}-1/\sqrt{\mu^{\ddagger}}}{1/\sqrt{\mu}-1/\sqrt{\mu^{*}}} \quad (10)$$

where μ is the reduced mass (μ = m M / [m + M]). In this case, the value of κ decreases with increasing mass of the non-substituted atom (Cao and Liu, 2011). The limit of equation 10 as the non-substituted mass approaches infinity is then:

$$\kappa_{LL} = \frac{1/\sqrt{m}-1/\sqrt{m^{\ddagger}}}{1/\sqrt{m}-1/\sqrt{m^{*}}} \quad (11)$$

which serves as an unattainable lower boundary of κ for diatomic molecules. Equation 10 is the same as the approximation to the mass fractionation law given by Swain et al. (1958) for triple hydrogen isotope fractionation.

The terms corresponding to the contribution from TRPR has a κ value of;

$$\kappa_{TRPR} = \frac{\ln(u^{\ddagger}) - \ln(u)}{\ln(u^{*}) - \ln(u)} \quad (12)$$

The limits of equation 12 for the diatomic special case are then given by;

$$\kappa_{TRPR-L} = \frac{\ln(m^{\ddagger}) - \ln(m)}{\ln(m^{*}) - \ln(m)} \quad (13)$$

and;

$$\kappa_{TRPR-H} = \frac{1/m - 1/m^{\ddagger}}{1/m - 1/m^{*}} \quad (14)$$

Importantly, the value of equation 12 can exist outside of the values given by equations 9 and 11. Due to the contribution β_{TRPR} being less than unity and independent of temperature, this expanded range may be the reason that κ values for some degrees of vibrational freedoms can exceed the high temperature limit (calculated from vibrational frequencies given in Wang et al. (2004)). However, this is not expressed for diatomic molecules. Because the effects of isotope substitution are dominantly local to the substituted atom, it is expected that the most significant contribution to the isotope effect comes from the bond directly associated with the substituted atom. For all calculated results for hypothetical diatomic molecules, the values of κ_h are found to not exceed the boundaries given by equations 9 and 11.

Figure 1b displays results for equilibrium isotope effects for hypothetical diatomic molecules containing oxygen under the harmonic approximation with an added consideration for temperature. A key finding here is the diatomic model allows for θ to hold any value for sufficiently small fractionations. Polyatomic molecules incorporate additional degrees of freedom which is expected to weaken the relationship between κ and β to some extent. Therefore, this result is a conservative estimates of the distribution of θ. Much like values of α for a two isotope system, the variability of θ becomes greater at lower temperatures.

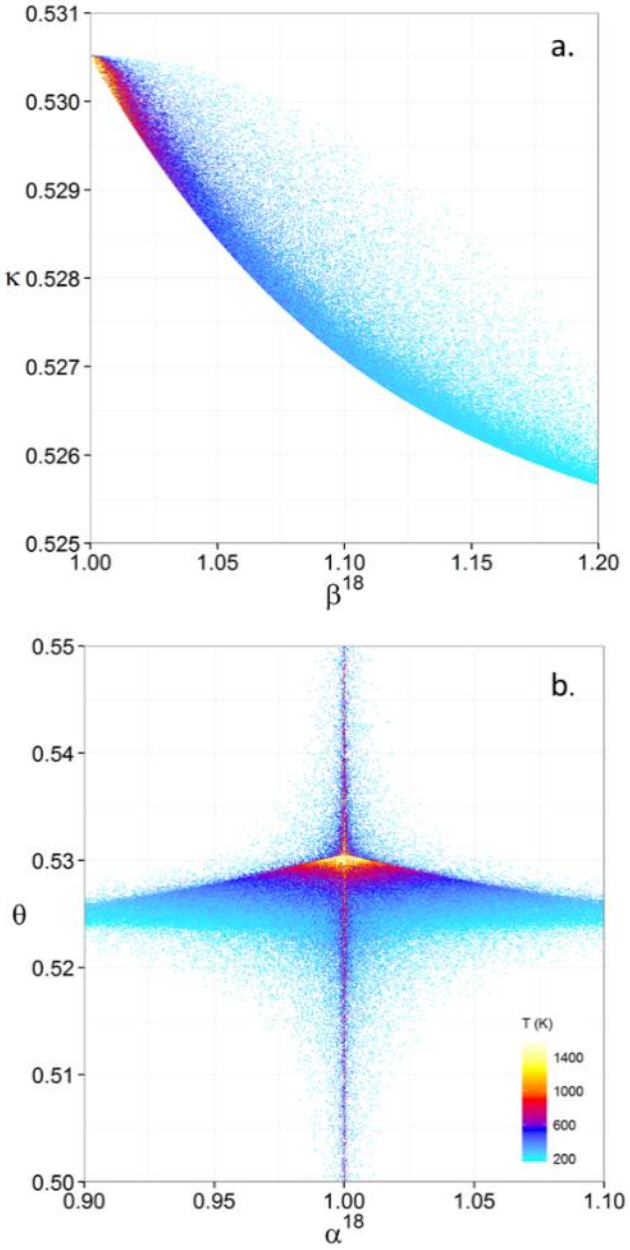

Figure 1. a.) β18 vs. κ and b.) Equilibrium α18 vs. θ plots for randomly selected diatomic molecules under the harmonic approximation in the 16O-17O-18O system. Temperature is plotted as color on the same scale for both plots.

4. KINETIC ISOTOPE EFFECTS

Kinetic isotope effects can be modeled as equilibrium between the relevant reactant and the transition state with the modification that one degree of freedom for the transition state corresponds to the decomposition mode (Bigeleisen and Wolfsberg, 1958). This can be described similarly to a two mass harmonic oscillator with a negative bond force constant and hence an imaginary frequency and is applied by multiplying equation 2 (minus one degree of freedom) by the ratio of the imaginary frequencies (Bigeleisen and Wolfsberg, 1958). The value of κ for the imaginary frequency contribution is then given by:

$$\kappa_{IF} = \frac{\ln(\mu^{\ddagger}) - \ln(\mu)}{\ln(\mu^{*}) - \ln(\mu)} \quad (15)$$

where μ corresponds to the reduced mass of the decomposition fragments. Because the imaginary frequency contribution to β is always less than 1.000, the result of equation 15, on average, results in higher values of κ for transition states, but a higher value is not necessarily the case. Because of this, κ for the transition state including the imaginary frequency contribution does not remain bounded by the harmonic limits described above but should remain within or relatively close to those boundaries for species with large contributions from other vibrational degrees of freedom. The result is that the values of θ for kinetic isotope effects have a wider distribution than equilibrium isotope effects. In addition, as previous research has shown normal kinetic isotope effects are expected to exhibit, on average, lower values of θ (Bao et al., 2015; Young et al., 2002). However, it is emphasized that kinetic isotope effects should not be strictly associated with low θ values.

5. ANHARMONIC CORRECTION

The harmonic approximation yields, by far, the largest contributions to both β and κ for any isotope system. However, for hydrogen bearing molecules, corrections for anharmonicity become significant enough to consider. The complete expression, accounting for anharmonicity, for the vibrational contribution to the energy levels of a diatomic molecule is given by,

$$E_n^* = G_0^* + \left(\frac{1}{2} + n\right) h\omega^* - \left(\frac{1}{2} + n\right)^2 \omega^* x^* + \text{Higher Order Terms} \quad (16)$$

where the second term corresponds to harmonic vibrations (Wolfsburg, 1969). The first and third terms give the anharmonic correction and,

$$G_0^* = \frac{21}{2}\gamma + \frac{1}{2}\delta \quad (17)$$

$$\omega^* x^* = -90\gamma - 2\delta \quad (18)$$

where δ and γ are functions of the parameters of the anharmonic potential, μ and the bond force constant. Because both δ and γ are proportional to 1/μ, both G_0 and ωx are proportional to 1/μ (Wolfsburg, 1969). The value of κ for the G_0 contribution for a diatomic molecule is then simply given by,

$$\kappa_{G_0-D} = \frac{1/\mu - 1/\mu^{\ddagger}}{1/\mu - 1/\mu^*} = \frac{1/m - 1/m^{\ddagger}}{1/m - 1/m^*} \quad (19)$$

Which note has a constant value equal to the high-temperature limit for harmonic vibrations. The zero-point energy of the remaining anharmonic term, which gives the majority of the correction, is given by $\omega x/4$ which yields a κ value also equal to the correction from G_0. The constancy of this value, although treated as the complete correction, was originally determined by Cao and Liu (Cao and Liu, 2011). The κ values for the excited state contributions to this term

as well as higher order corrections are not calculated here but have respective β values that are expected to be small enough to mostly be neglected for any system.

The effect of anharmonic corrections on the value of κ is treated in the same manner as additional vibrational degrees of freedom so that the final κ value is equal to the sum of the ln β weighted contributions from the anharmonic correction and harmonic κ values. Because the anharmonic corrections are small (<5% for hydrogen) relative to the harmonic contribution and have a predictable and equal κ value, incorporation of the anharmonic correction yields only a slightly lower value of κ than the harmonic model.

6. ROTATIONAL CORRECTION

Although the contribution to isotope fractionation from non-classical molecular orbital rotations is small relative to the harmonic contribution for most isotope systems, for hydrogen isotope effects this contribution may be significant enough to be considered. The rotational correction to the B-GM-U model is given by the ratio of the quantum contributions to the rotational partition functions of the two isotopically substituted species (Richet et al., 1977).

$$Q_{rot-qua.} = \frac{Q_{rot}}{\lim_{T\to\infty} Q_{rot}} = \frac{Q_{rot}}{Q_{rot-class.}} \quad (20)$$

This is because the classical rotational partition function has already been considered in the B-GM-U model through the use of the Teller-Redlich product rule. For diatomic molecules, the classical contribution to the rotational partition function is given by;

$$Q_{rot-class.} = \frac{1}{s\sigma} \quad (21)$$

where s is the symmetry number and σ is given by;

$$\sigma^* = \frac{h^2}{8\pi^2 I^* k_B T} \quad (22)$$

where h is the Planck constant, k_B T is temperature in terms of energy and I is the moment of inertia ($I = \mu R^2$). The complete partition function for rotation is given by Richet et al. (1977);

$$Q_{rot} = \sum_J (2J+1) e^{-J(J+1)\sigma} \quad (23)$$

or; (Richet et al., 1977; Viney, 1933),

$$Q_{rot} = \frac{1}{s\sigma}\left(1 + \frac{\sigma}{3} + \frac{\sigma^2}{15} + \frac{4\sigma^3}{315} + \cdots\right) \quad (24)$$

From equations 20, 21 and 24, the quantum mechanical contribution to the rotational partition function is given by;

$$Q_{rot.\ corr.} = \left(1 + \frac{\sigma}{3} + \frac{\sigma^2}{15} + \frac{4\sigma^3}{315} + \cdots\right) \quad (25)$$

then;

$$\beta^*_{rot.\ corr.} = \frac{\left(1+\frac{\sigma^*}{3}+\frac{{\sigma^*}^2}{15}+\frac{4{\sigma^*}^3}{315}+\cdots\right)}{\left(1+\frac{\sigma}{3}+\frac{\sigma^2}{15}+\frac{4\sigma^3}{315}+\cdots\right)} \quad (26)$$

For high temperatures, σ is a small number, and each subsequent term diminishes in importance. Using the first term only as well as the approximation $ln(1+x) \approx x$ if $x \approx 0$, yields a κ value of;

$$\kappa_{rot.corr.} \approx= \frac{1/m - 1/m^{\ddagger}}{1/m - 1/m^{*}} \quad (27)$$

Alternately to the use of equation 24, equation 23 can be calculated iteratively. The values of $\beta^*_{rot.\ corr.}$ from the iterative calculation yield essentially the same results as the corresponding first four terms of equation 24. It is found from both the iterative calculation and the solutions to equation 24 for hypothetical diatomic molecules, that the value of $\kappa_{rot.corr.}$ is equal to the value for equation 27 for all temperatures. However, in the computation there are some values that slightly (<0.02%) exceed equation 27 at very low temperatures but this is interpreted as a computational discretization error. Because equation 27 is equal to the high temperature limit for the vibrational contribution and that the result of ln(β) from equation 26 is negative leads to the conclusion that consideration of rotation yields a higher value of κ for diatomic molecules.

7. CHANGE/DIFFERENCE IN "CAP-DELTA"

Even though κ is expected to be bounded to a first-order approximation by the high temperature and lower limits as described above, the more common mass-dependent fractionation exponent, θ, is not. What is needed is an additional descriptor for multiple isotope fractionation relationships that corrects for small isotope effects.

Measured multiple isotope relationships are commonly expressed in the "cap-delta" notation.

$$\Delta^{\ddagger}M = ln\,(R^{\ddagger}_{sample}/R^{\ddagger}_{standard}) \; - C\; ln\,(R^{*}_{sample}/R^{*}_{standard}) \qquad (28)$$

typically either in ‰ or "permeg", where C is a somewhat arbitrarily set constant that differs between laboratories and R is the molar ratio of one isotope and a reference isotope of the same element. For example, "$\Delta^{\ddagger}M$" becomes "$\Delta^{17}O$" for the ^{16}O-^{17}O-^{18}O system.

The change, or difference in cap-delta through a fractionation process is then:

$$\Delta\Delta^{\ddagger}M = ln\,\alpha^{\ddagger}_{A-B} - C\; ln\,\alpha^{*}_{A-B} \qquad (29)$$

or reduced to more fundamental parameters,

$$\Delta\Delta^{\ddagger}M = (C - \kappa_B)\; ln\,\beta^{*}_{B} - (C - \kappa_A)\; ln\,\beta^{*}_{A} \qquad (30)$$

Current analytical precision for $\Delta^{\ddagger}M$ can be as low as 0.002‰ depending on the element, technique, and species analyzed allowing for the resolution of $\Delta\Delta^{\ddagger}M$ well within the natural range for many commonly explored light elements (e.g. oxygen in Fig. 2). Using the ^{16}O-^{17}O-^{18}O system as an example, if the arbitrary upper limit of β is given to be 1.100 and using the boundaries of κ proposed above (0.5232 to 0.5305), a maximum potential range of $\Delta\Delta^{17}$O is then of ±0.7‰. The ends of this range will likely never be realized for a real system except at very low temperatures where values of β become larger and more variable and the lower boundary of

κ becomes more obtainable. A more realistic range for natural samples is likely in the vicinity of ±0.3‰. (C=0.5305). This value is comparable to measured values for silica-water fractionation near 0°C (Sharp et al., 2016). Kinetic isotope effects should have more variable $\Delta\Delta^{17}O$ values because of their more variable κ values, however the range is expected to be similar to that of equilibrium isotope effects (Bao et al., 2015).

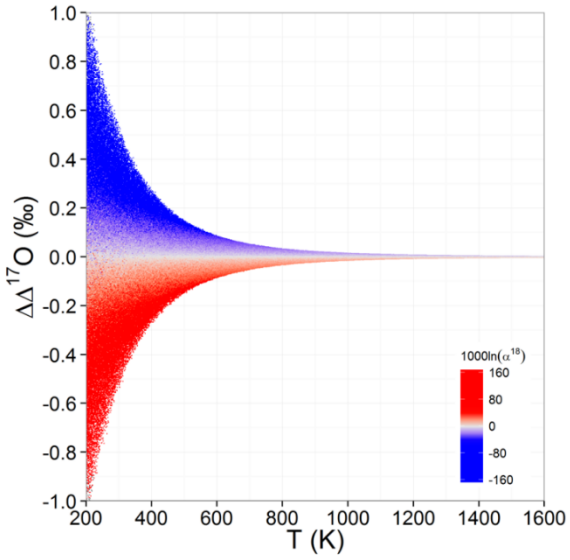

Figure 2. Temperature vs. $\Delta\Delta^{17}O$ plot for equilibrium between randomly selected diatomic molecules under the harmonic approximation in the ^{16}O-^{17}O-^{18}O system. A C value of 0.5305 (HTL) is used for the $\Delta\Delta^{17}O$ definition. $1000\ln\alpha^{18}$ is plotted as color.

Regardless of the value of C, $\Delta\Delta^{\ddagger}M$ will approach a high temperature limit of 0 because both β_A^* and β_B^* approach a high temperature limit of 1.000. Here, we recommend the use of the high temperature limit of κ for C primarily because a value of C equal to the upper bound of κ will ensure that the (C-κ) terms in equation 14 will remain positive with a minimum value of zero. This condition means that for very different β values (i.e. large values of $ln\,\alpha_{A-B}^*$) the sign of $\Delta\Delta^{\ddagger}M$ will be determined by the larger β. For large positive $ln\,\alpha_{A-B}^*$values, $\Delta\Delta^{\ddagger}M$ will tend to

be negative and for large negative $ln\,\alpha^{*}_{A-B}$ values, $\Delta\Delta^{\ddagger}M$ will tend to be positive. This trend is not necessarily expected for α near unity particularly at low temperatures. The use of this value for C was also suggested by Pack & Herwartz (2014, 2015) as well as Bao et al. (2016) although based on different reasoning.

8. HEMATITE-WATER FRACTIONATION

It seems desirable to test the predictions of the work above experimentally. For crossover scenarios, there is a guarantee that the determined α value will be near unity. In Bao and Koch (1999) hematite (Fe_2O_3), which derives oxygen from water, was precipitated at a range of temepratures and measured for $\delta^{18}O$ (Bao and Koch, 1999). Because the water used for the precipitation had a known oxygen isotope composition (-8.0 ‰), fractionation factors for the experiments could be determined which results in the measurement of such a crossover scenario. Nine samples are selected from this study for triple oxygen isotope analysis using CO_2-laser fluorination in a BrF_5 atmosphere. New $\delta'^{18}O$ and $\delta'^{17}O$ values for the hamatite samples are determined by CO_2-laser fluorination in a BrF_5 atmosphere and subsequent analysis on a ThermoFinnigan Mat 253. Further details of the analysis can be found in the Appendix B. The corresponding water triple oxygen isotope data for New Jersey tap water is estimated from recently published modern $\Delta^{17}O$ for Baltimore tap water (0.02‰; C=0.528) given by Li et al. (2015). Despite the speculative nature of our chosen tap water value, the observed trend is not sensitive to the value picked to represent New Jersey tap water because the range of tap waters (~0.04‰) for the continental United States is comparable to the analysis uncertainty (0.03‰) for the hematite $\delta^{18}O$ and $\Delta^{17}O$ values (LI et al., 2015). The results of this analysis along with the

calculated fractionation parameters can be found in Table S-1. The calculated fractionation parameters with their uncertainties and best fits are illustrated in Figure 3.

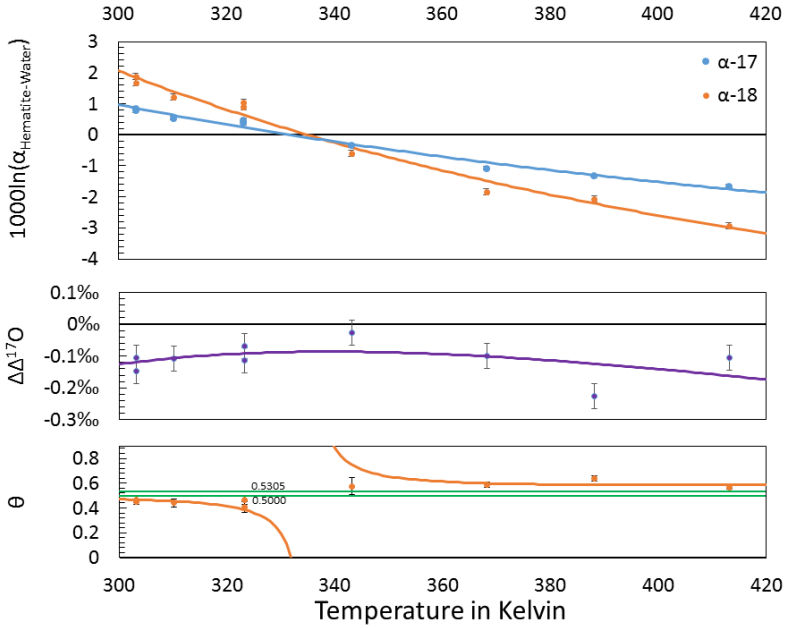

Figure 3. Three isotope fractionation parameters for hematite synthesis conducted by BAO AND KOCH (1999). Values are calculated from newly measured $\delta^{18}O_{Hematite}$ and $\delta^{18}O_{Water}$ values, and an assumed $\Delta^{17}O$ (C=0.528) of 0.02‰ for the water used for the synthesis based on reported Baltimore tap water from LI et al. (2015). $\Delta\Delta^{17}O$ are reported using C=0.5305. The method for calculating uncertainties can be found in Appendix C. Best fit curves for the ln(α) values are second order polynomials of 1/T. The best fit curves for $\Delta\Delta^{17}O$ and θ are calculated from the fits to ln(α).

From the calculated hematite fractionation parameters, it is clear that the crossover temperature is different for α^{17} and α^{18}. As a caveat, the results of the calculated hematite-water fractionation parameters given here assume that the calibrations of Li et al. (2014) and Bao and Koch (1999) for water isotope analysis are consistent with our calibration. Slight differences in calibration to SMOW/VSMOW between studies may have an effect on the calculated values of each parameter but this is not expected to have a significant effect on the range of θ values.

With one exception, every one of the experimentally measured θ values exists outside of the typical "canonical" range of θ (approximately 0.5000 to 0.5305) to beyond 1σ uncertainties. Despite the variability in θ, $\Delta\Delta^{17}O$ values remain within a range of -0.026 ‰ to -0.226 ‰ within the theoretically predicted mass dependent range. Further work along similar lines is needed to experimentally examine what is possible for mass-dependent isotope fractionation for specific systems.

9. HYDROGEN

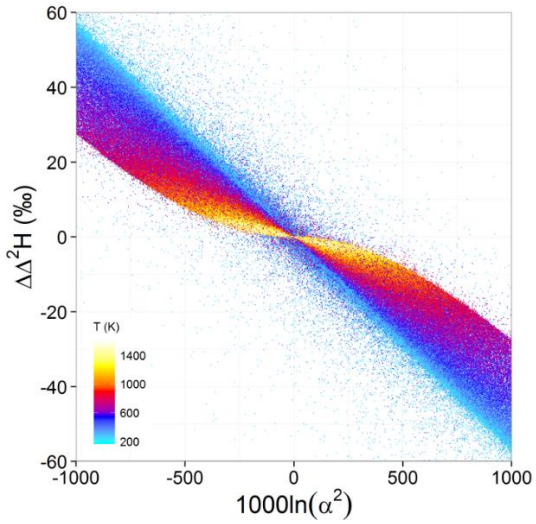

Figure 4. $1000\ln\alpha^2$ vs. $\Delta\Delta^2H$ plot for equilibrium between randomly selected diatomic molecules under the harmonic approximation in the H-D-T system. A C value of 0.7503 (HTL) is used for the $\Delta\Delta^2H$ definition. Temperature is plotted as color.

The treatment of multiple isotope relationships for hydrogen was developed independently from treatments for other elements due to the relevance of three isotope relationship of hydrogen as an unambiguous tracer of quantum mechanical tunneling for kinetic processes. For these studies, the Swain-Schaad Exponent (SSE or χ) an analogous concept to a θ is used as a three isotope relationship descriptor (Swain et al., 1958).

$$SSE = \theta^{-1} = \frac{ln(\alpha^{T}_{A-B})}{ln(\alpha^{D}_{A-B})} = \frac{ln(k_T/k_H)}{ln(k_D/k_H)} \quad (31)$$

Using assumptions equivalent to saying that the transition state has no preference for one isotope over another (β_{TS}=1.000), quantum mechanical tunneling was expected to exhibit via a SSE value greater than the upper limit given by the harmonic model given here by equation 11 (Swain et al., 1958). Consideration for the various corrections, which are most significant for hydrogen isotope fractionation show that this value can be exceeded even if the transition state did not contribute to the fractionation. Consideration of β_{TS} gives an additional avenue to predict SSE values which vary from positive to negative infinity for small fractionations. This work, as well as the work of (Hirschi and Singleton, 2005) suggests that there are no boundaries on the value of SSE. In that study they suggested that the value SSE should not be used without context of the isotope effect, a statement that this work indicates as well (Hirschi and Singleton, 2005). The concept of $\Delta\Delta^{\ddagger}$M, or in the case of hydrogen $\Delta\Delta^{2}$H as a descriptor of mass dependence corrects for small isotope effects and can be implemented for most, if not all, cases in which a value of SSE can be determined. The $\Delta\Delta^{2}$H concept has the key advantage of not deviating from a defined range for given limits of temperature provided that the number of kinetic steps is limited (Bao et al., 2015). The mass-dependent range of $\Delta\Delta^{2}$H can be further constrained with consideration for the deuterium isotope effect (see Figure 3) because larger isotope effects can yield larger $\Delta\Delta^{2}$H values. Since rates for quantum tunneling are much higher for hydrogen as opposed to tritium and deuterium (Klinman, 2003), the contribution from tunneling will cause a decrease in $\Delta\Delta^{2}$H that is not constrained by the limits of mass dependent fractionation.

1. CONCLUSIONS

Using the simplest application of the B-GM-U model, it is shown theoretically that values of the mass fractionation exponent, θ, are unbounded and particularly variable for small fractionations and at low temperatures. This is in contrast to the half-reaction mass-fractionation exponent, κ, which is bounded by upper and lower limits. As a supplemental mass-fractionation descriptor, $\Delta\Delta^{\ddagger}M$ is suggested on a theoretical basis because it remains within a finite range for mass-dependent fractionations. Deviations from the "canonical" range of θ for oxygen are measured for hematite precipitation from water. These deviations are found to be consistent with a finite range of $\Delta\Delta^{17}O$. It is our opinion based on the results of this study that the concept of a "canonical" range of θ values is not well founded or needed.

CHAPTER 2: THEORETICAL CALIBRATION OF THE $\Delta\Delta^{17}O$ THERMOMETER

PREFACE

The work presented in Chapter 2 was completed after the work presented in Chapter 1 and is currently being prepared for publication. The intent is to submit this work to *Geochimica et Cosmochimica Acta.*

ABSTRACT

The field of isotope geochemistry began with the study of oxygen isotope geothermometry, most famously for carbonates. For traditional oxygen isotope geothermometry only the relationship between one rare isotope, oxygen-18, and the common isotope, oxygen-16, is used because for most terrestrial processes the ^{17}O-^{16}O relationship roughly scales with the ^{18}O-^{16}O relationship and is thought to not provide any new information. However, modern instrumentation and techniques now allow for the high precision determination of the oxygen isotope composition for all three oxygen isotopes for a variety of sample types. With sufficient analytical precision, it is possible to extract further information from the three oxygen isotope composition of a sample. In this study, new theoretical calibrations are presented for both the traditional two-isotope and the recently introduced three-isotope thermometer for pairs of quartz, calcite, dolomite, fluorapatite, hematite, magnetite and liquid water. The results presented here compare well with previous studies on $^{18}O/^{16}O$ fractionation where data is available. Of the models given here, pairs of quartz, calcite, dolomite and fluorapatite with water, hematite and magnetite show promise as three isotope thermometers with acceptable uncertainties for surface and low-T hydrothermal environments. As an example, the new quartz-water fractionation curves are applied to triple oxygen isotope date from previously published 2.5 Ga marine chert

samples. These results indicate that the water which those chert samples formed from had a temperature of < 1°C and a $\delta'^{18}O$ of < -23.8‰.

1. INTRODUCTION

The potential for isotope fractionation to be used as a geothermometer dates back to the work of Harold Urey who recognized the temperature dependence of oxygen isotope fractionation between carbonate and water (Urey, 1947). At the time, isotope ratio mass spectrometry was in its infancy and precisions of only one part per thousand were possible for the ratio of the two most abundant isotopes of oxygen, ^{16}O and ^{18}O. For low temperatures, this precision allowed for the carbonate geothermometer, with assumptions on the isotope composition of the water, to have a precision on the order of 6°C (Urey, 1947). Early on, it was assumed that isotope fractionation for the ^{17}O-^{16}O system would be scale with ^{18}O-^{16}O system and so it was thought that measuring the $^{17}O/^{16}O$ ratio would provide no useful further information. The discovery of large non-mass dependent isotope effects associated with ozone chemistry changed this paradigm leading to a newfound need to measure the three isotope composition of various oxygen reservoirs which has led to a robust field in the utility of three oxygen isotope compositions (Bao et al., 2008; Heidenreich and Thiemens, 1983; Killingsworth et al., 2013). Over time, analytical precision and techniques improved to the point where much smaller mass-dependent variations are resolvable and can be related to chemically and geochemically relevant parameters (Pack and Herwartz, 2014; Sharp et al., 2016). What has become apparent is that much like with the two isotope systems, fractionation in three isotope systems is temperature dependent (Bao et al., 2016; Pack and Herwartz, 2014) (Chapter 1). This extra dimension of temperature dependency led to the suggestion by Pack and Herwartz that the

value of the mass dependence exponent, θ, can be used as a separate geothermometer for low temperature systems (Pack and Herwartz, 2014).

For the oxygen three isotope system, θ is given by;

$$\theta = \frac{\ln {}^{17}\alpha_{A-B}}{\ln {}^{18}\alpha_{A-B}} \quad (1)$$

where α is the fractionation factor which for measurement purposes is given by:

$${}^{18}\alpha_{A-B} = \frac{[{}^{18}n/{}^{16}n]_A}{[{}^{18}n/{}^{16}n]_B} \quad (2)$$

where $[{}^{18}n/{}^{16}n]$ is the molar ratio of the rare/heavy isotope ^{18}O and the common/light isotope ^{16}O. In both equations, the superscript indicates the isotope system and the subscript indicates the species involved in the equilibrium (e.g. A-B => Calcite-$H_2O_{(L)}$). Theoretically, α can be calculated by replacing the molar ratio terms by the respective β values for each species. The concept of β can be thought of as a theoretical "affinity" parameter of the rare/heavy isotope relative to the common/light isotope.

Not long after the introduction of the θ based three isotope thermometer, the concept of using the temperature dependence of $\Delta\Delta'^{17}O$, or the change/difference in "Cap-delta-seventeen" as a geothermometer was introduced. This was independently suggested by Bao et al. (2016) based on previous theoretical work for calcite-water equilibrium and Sharp et al. (2016) based on measurements of natural quartz and silica samples. The core concept of "Cap-delta-seventeen" or "Cap-seventeen" is given by the equation:

$$\Delta'^{17}O = \delta'^{17}O - C\delta'^{18}O \quad (3)$$

where $\delta'^{18}O$ is given by:

$$\delta'^{18}O = \ln \frac{[^{18}n/^{16}n]_{sample}}{[^{18}n/^{16}n]_{standard}} \quad (4)$$

and C is an arbitrary constant that, at this time, varies from lab-to-lab but is in the vicinity of 0.5. Based on the arguments put forth by Hayles et al. (Chapter 1) and Bao et al. (2016), here C=0.5305 is used. This value is equal to the high temperature limit of θ for oxygen isotope fractionation under the harmonic approximation and allows for the simplest generic behavior for the temperature dependence of $\Delta\Delta'^{17}O$.

Although they can be shown to be mathematically equivalent, in practice, the use of $\Delta\Delta'^{17}O$ has three primary advantages over the use of θ. (1) Application of the $\Delta\Delta'^{17}O$ thermometer is very similar to the commonly used $\delta^{18}O$ thermometer. (2) Covariance between the measurements of $\delta'^{18}O$ and $\delta'^{17}O$ lead to a higher precision for $\Delta'^{17}O$ than would be expected from the uncertainties of $\delta'^{18}O$ and $\delta'^{17}O$. (3) The temperature dependency of $\Delta\Delta'^{17}O$ is simple and does not deviate from a finite range for small values of $\Delta\delta'^{18}O$. This is as opposed to θ which can be very uncertain and fundamentally hold any value for small enough values of $\Delta\delta'^{18}O$ (Chapter 1).

The purpose of this study is to further investigate the viability of a three isotope thermometer based on the ^{16}O-^{17}O-^{18}O system from a theoretical perspective. Rather than the temperature dependency of θ (Pack and Herwartz, 2014, 2015), here the temperature dependency of $\Delta\Delta'^{17}O$ (Bao et al., 2016; Sharp et al., 2016) is used as a mass-dependent fractionation descriptor for its ease of use and relatively simple temperature dependency. In this study, new theoretical calculations for equilibrium pairs of hematite, magnetite, fluorapatite, calcite, dolomite, quartz and liquid water were carried out for both the $\Delta\delta'^{18}O$ and $\Delta\Delta'^{17}O$ systems. It is found that using the assumption of isotope equilibrium: fluorapatite-$H_2O_{(L)}$, calcite-$H_2O_{(L)}$,

dolomite-$H_2O_{(L)}$, and quartz-$H_2O_{(L)}$ have potential as effective three-isotope thermometers for surface to hydrothermal environments. Both hematite and magnetite can be used in place of $H_2O_{(L)}$ for the above pairs with only minor reduction in temperature sensitivity. The results for quartz-$H_2O_{(L)}$ equilibrium given here are in good agreement with the empirical results of Sharp et al. (2016). As an application example, the quartz-$H_2O_{(L)}$ calibration is applied to previously published triple oxygen isotope results of 2.5 Ga marine chert samples from Levin et al. (2014). Assuming that the chert samples represent equilibrium with coeval seawater, the results indicate that the $\delta'^{18}O$ of the seawater was < -23.8‰ at a temperature <1 °C.

2. METHODS

2.1 Calculation of β_h for Minerals

Periodic boundary conditions are typically used to represent the crystal environment and have been used to predict inter-minerals isotope fractionation factors for many systems (Blanchard et al., 2009; Huang et al., 2013; Schauble, 2011). However, this method is challenged when dealing with the systems involving aqueous species. In order to use consistent methods for the representation of both minerals and aqueous species, molecule-like clusters were introduced to predict mineral-aqueous isotope fractionation factors (Gibbs, 1982; Rustad et al., 2010).

Here, the Volume Variable Cluster Method (Li and Liu, 2015) is used for the calculation of values of β under the harmonic approximation ($\beta_{h)}$ for all minerals. VVCM is similar to the embedded cluster method (Rustad et al., 2010). The original mineral structures are taken from American Mineralogist Crystal Structure Database (http://rruff.info/). The modeled clusters are cut from these mineral structures with the atoms of interest (e.g. O-atoms or PO_4 groups) at the core. For example, if the O or C atoms in carbonate minerals are of interest, a CO_3 group is

placed at the core of the clusters and surrounded by six metal atoms as the second shell, the third shell is made of CO_3 with the O atoms at the edge. As with any cluster model, ideally larger clusters would be used, but computation costs increase exponentially with each additional shell. Cluster size may have effects on the frequencies and therefore the value of β_h, but isotope effects are dominantly local to the substituted atom and each subsequent shell has a diminishing influence on β_h at an increasingly significant computational cost.

In order to maintain the neutral environment for the modeled clusters, for most systems, hundreds of virtual point charges are added at the edge of clusters by bonding to the outer O atoms at certain bond lengths. Rustad et al. (2010) suggested an embedded cluster method with outermost point charges bond to outer fixed O atoms at a distance of 1 Å, however, this distance may significantly influence the β_h values. In addition, in VVCM, the outermost virtual point charges may have different valences which are determined by the bonding environment. For example, in the calcite cluster model, there are 48 point charges each with a valence of 1/6, these charges are bound to the bridging O which connects the Ca atom and outer C atom. There are another 81 point charges each with a valence of 2/9, these point charges are bond to the outer O atoms. All of the point charges are fixed at a certain distance and full-cluster optimizations are performed. By changing the point charge bond length through optimization, the distances which generate the most stable configuration (lowest energy) are found. The calcite cluster has two kinds of point charges, so this searching procedure is conducted twice to find the optimal distance for each.

Once optimal point charge distances are found, the clusters are optimized and the harmonic frequencies are calculated using GAUSSIAN09 to the B3LYP/6-311g* (d) level of theory. β_h

values are calculated from the resulting harmonic frequencies through application of the Bigeleisen-Mayer-Urey model given by (Bigeleisen and Goeppert-Mayer, 1947; Urey, 1947):

$$\beta_h^* = \prod_i^{3n-6(5)} \left(\frac{u_i^*}{u_i}\right)_{TRPR} \left(\frac{e^{-u_i^*/2}}{e^{-u_i/2}}\right)_{ZPE} \left(\frac{1-e^{-u_i}}{1-e^{-u_i^*}}\right)_{EXC} \quad (5)$$

$$u^* = \frac{h\upsilon^*}{k_B T} \quad (6)$$

Further details of VVCM, can also be found in Li et al., (2015). All calculations of β_h from frequencies are conducted in R (R Core Team, 2012). Corrections beyond the harmonic model are expected to be negligible for mineral systems. An example image of a cluster used in the calculation can be found in Figure 5.

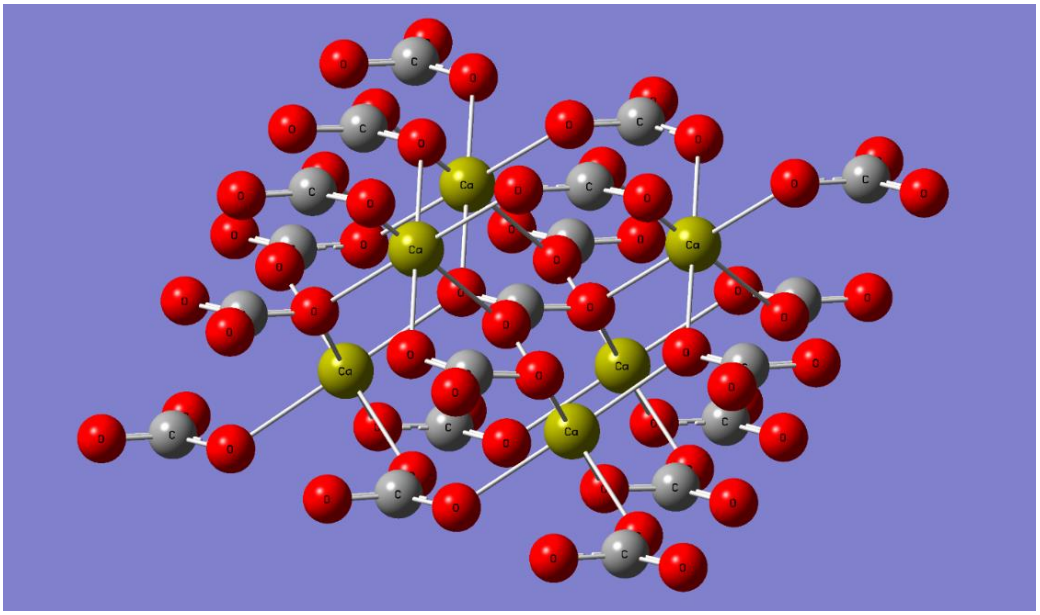

Figure 5. Example image of a calcite cluster after optimization in GAUSSIAN09.

2.2 Calculation of β_h for Liquid Water

The model for β_h of liquid water consists of twenty two water molecules arranged and optimized in a cluster constructed in GAUSSVIEW and optimized to the B3LYP/6-

311+g*(2df,p) level of theory (Figure 6). Individual β_h values from substitutions of each water molecule in the cluster are calculated using the B-GM-U model from harmonic vibrational frequencies for the whole system and averaged to yield the final result (Bigeleisen and Goeppert-Mayer, 1947; Urey, 1947). The anharmonic correction is expected to be significant for oxygen isotope fractionation involving water. Equation 5 can be rewritten as:

$$\beta_h^* = e^{\frac{\Delta ZPE_h}{k_B T}} \prod_i^{3n-6(5)} \left(\frac{u_i^*}{u_i}\right)_{TRPR} \left(\frac{1-e^{-u_i}}{1-e^{-u_i^*}}\right)_{EXC} \quad (7)$$

where the ZPE term from equation 7 is rewritten as a term that is a function of the difference in the zero point energy between the two isotopically substituted states for the harmonic approximation (ΔZPE_h).

The anharmonic correction to zero point energy is applied as a scaling factor (SF) to the ΔZPE_h term in equation 7 to determine ΔZPE_{anh} (=$SF \times \Delta ZPE_h$). The scaling factor used here is determined through the less expensive calculation of the harmonic and anharmonic zero point energies in GAUSSIAN09 for water vapor calculated to the B3LYP/6-311+g*(2df,p) level of theory and is given by $\Delta ZPE_{anh\text{-vapor}}/\Delta ZPE_{h\text{-vapor}}$. Application of a scaling factor in this way is based on the assumption that the $\Delta ZPE_{anh}/\Delta ZPE_h$ ratio is the same for liquid water and water vapor. Values for $\Delta^{18\text{-}16}ZPE_{anh\text{-vapor}}/\Delta^{18\text{-}16}ZPE_{h\text{-vapor}}$ and $\Delta^{17\text{-}16}ZPE_{anh\text{-vapor}}/\Delta^{17\text{-}16}ZPE_{h\text{-vapor}}$ are calculated to be 0.9654045 and 0.9653695 respectively. The application of the anharmonic correction as well as the calculations of β_h from frequencies are conducted in R (R Core Team, 2012). An image of a cluster used in the calculation can be found in Figure 6.

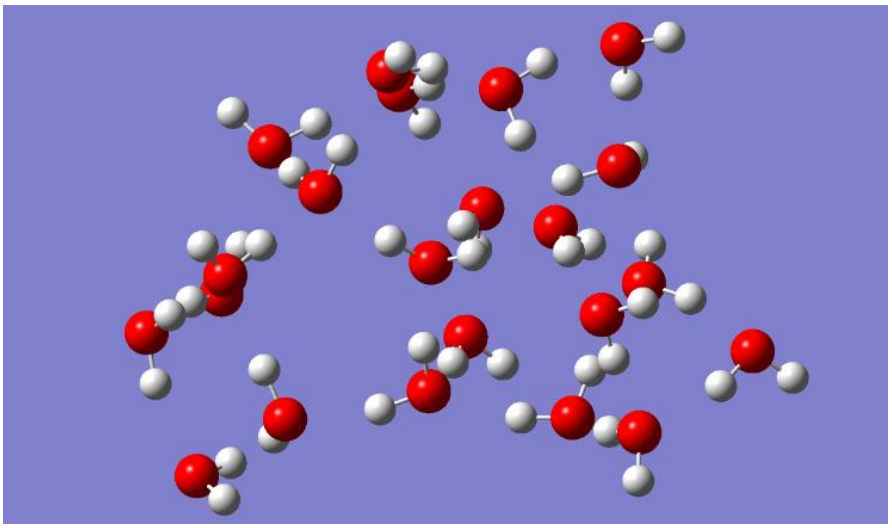

Figure 6. Image of a water cluster after optimization in GAUSSIAN09.

3. RESULTS

Rather than reporting functions for $\ln(^{18}\alpha)$ and θ values as is typical, here high order polynomial fits to functions of 1/T are reported for $\ln(^{18}\beta)$ and κ. These can be converted to $^{18}\alpha$ and θ values using the equations:

$$\alpha_{A-B} = \frac{\beta_A}{\beta_B} \quad (8)$$

and,

$$\theta = \kappa_A + (\kappa_A - \kappa_B)\frac{ln\,\beta_B^*}{ln\,\alpha_{A-B}^*} \quad (9)$$

Fits to these parameters are used in order to avoid complications with crossover scenarios which are exhibited for all mineral-water exchange models given here at some temperature. The fits presented here are accurate to the models for temperatures ranging from -100°C to 1400°C. The standard deviation of the residuals for all seventh-order polynomial fits to $\ln(^{18}\beta)$ is $5\text{x}10^{-6}$ or better which amounts to a precision of the fits to the models of 0.005 or better for $1000*\ln(^{18}\alpha)$. The standard deviation of the residuals for the fifth-order polynomial fits for κ or liquid water is the largest at $4.5\text{x}10^{-6}$ with other fits having standard deviations one to two magnitudes smaller.

Table 1: Parameters for fitting functions for ln($^{18}\beta$). The fitting function is a seventh order polynomial of the form $\frac{A}{T^7} + \frac{B}{T^6} + \frac{C}{T^5} + \cdots + Intercept.$

Material	A	B	C	D	E	F	G	Intercept
Quartz	7.000001E+14	-1.739669E+13	1.706601E+11	-7.528721E+08	4.018715E+05	1.197103E+04	5.064246E-02	7.219831E-07
Calcite	7.001567E+14	-1.625985E+13	1.456028E+11	-5.370606E+08	-4.651662E+05	1.307834E+04	-5.480925E-01	1.349371E-04
Dolomite	6.949136E+14	-1.616523E+13	1.451118E+11	-5.377717E+08	-4.557284E+05	1.320722E+04	-5.394747E-01	1.328654E-04
Fluorapatite	3.924514E+14	-1.028326E+13	1.077840E+11	-5.190680E+08	3.669489E+05	9.616497E+03	1.254418E-01	-2.165897E-05
Hematite	-5.137358E+12	-3.477822E+11	1.112701E+10	-1.066888E+08	7.191433E+04	6.667820E+03	4.288981E-02	-9.477480E-06
Magnetite	-1.196623E+12	-4.535106E+11	1.220762E+10	-1.113924E+08	7.719903E+04	6.638126E+03	4.550466E-02	-1.001796E-05
Liquid Water	-2.354608E+15	5.633400E+13	-5.609674E+11	3.022021E+09	-9.631112E+06	1.947708E+04	2.183388E-01	-6.862985E-04

Table 2: Parameters for fitting functions for κ. The fitting function is a fifth order polynomial of the form $\frac{A}{T^5} + \frac{B}{T^4} + \frac{C}{T^3} + \cdots + Intercept.$

Material	A	B	C	D	E	Intercept
Quartz	7.841629E+08	-1.908666E+07	1.727186E+05	-6.500919E+02	2.038661E-01	5.305547E-01
Calcite	1.018997E+09	-2.115747E+07	1.683596E+05	-5.764615E+02	1.481431E-01	5.305221E-01
Dolomite	9.941968E+08	-2.068635E+07	1.651185E+05	-5.685489E+02	1.452858E-01	5.305295E-01
Fluorapatite	3.121793E+08	-9.639767E+06	1.037679E+05	-4.525304E+02	1.323896E-01	5.305167E-01
Hematite	-1.366207E+08	1.555290E+06	5.848571E+03	-1.349643E+02	1.055602E-02	5.307719E-01
Magnetite	-1.413876E+08	1.431480E+06	8.548909E+03	-1.480068E+02	1.469748E-02	5.310537E-01
Liquid Water	-2.565022E+09	4.479775E+07	-3.036283E+05	1.010421E+03	-1.809941E+00	5.316386E-01

As can be seen in table 2, best fit curves of κ for most species have an intercept very near the high temperature limit for oxygen isotopes of 0.5305. The exceptions to this are liquid water, hematite and magnetite. For liquid water, this can be attributed to the incorporation of the anharmonic correction scaling factor.

4. DISCUSSION

4.1 Mineral pairs with $H_2O_{(L)}$

By far, the most common aplication of oxygen isotope geothermometers relates to equilibrium between minerals and liquid water. Most commonly mineral-$H_2O_{(L)}$ thermometers utilize carbonate minerals, but geothermometers have been proposed using silicate and phosphate minerals as well (Lecuyer et al., 2013; Longinel.A and Nuti, 1973; Pack and Herwartz, 2014; Sharp et al., 2016). Figure 7a illustrates the theoretical relationship between $\Delta\delta'^{18}O$ ($=1000‰\ln(^{18}\alpha)$) and temperature for mineral-$H_2O_{(L)}$ equilibrium calculated by the VVCM method for quartz, fluorapatite, calcite, dolomite, hematite and magnetite. As expected based on previous literature, the predicted difference between the $\delta'^{18}O$ values of quartz and liquid water is the greatest, followed by dolomite, calcite and fluorapatite. Previous research has found only small fractionations for oxygen isotopes between hematite and water which is in at least rough agreement with the new theoretical results presented here (Bao and Koch, 1999).

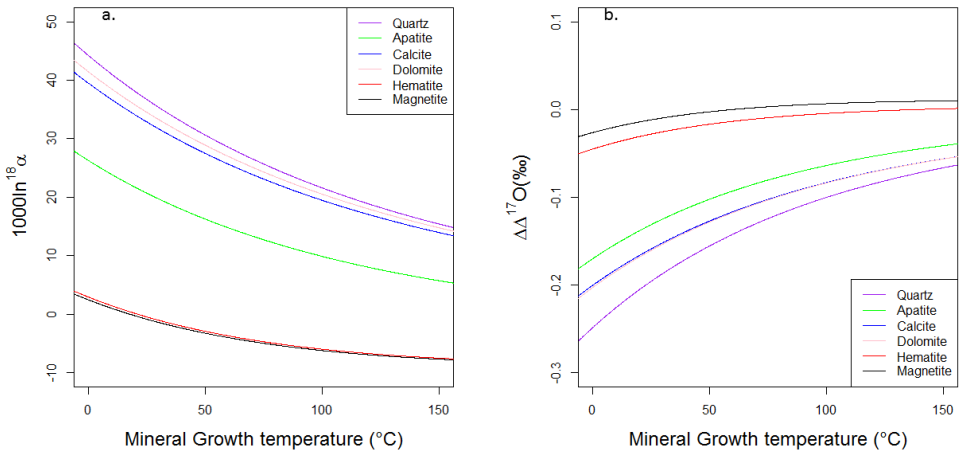

Figure 7. Theoretical results for (a.) $\Delta'\delta^{18}O$ and (b.) $\Delta\Delta^{17}O$ temperature dependence for Mineral-$H_2O_{(L)}$ equilibrium. The temperature ranges displayed are restricted to the geologically relevant temperatures where $\Delta\Delta^{17}O$ has the most variability.

Similarly to the $\delta^{18}O$ based mineral-water geothermometer, the $\Delta'^{17}O$ based geothermometer requires knowledge or assumptions on the isotope composition of the water that the mineral precipitates from. However, the assumptions that these require are different. The $\delta^{18}O$ thermometer requires knowledge of the $\delta^{18}O$ of the water whereas the $\Delta^{17}O$ thermometer requires knowledge of the $\Delta'^{17}O$ of the water. As the most geologically significant water reservoir, the variability of $\delta^{18}O$ of seawater has been an important topic of study but currently little has been determined about the variability of the $\Delta'^{17}O$ of seawater. Pack and Herwartz (2014) argued that the three isotope composition of seawater should not be constant through geologic time and that it is controlled by two dominant processes (1) low temperature mineral interaction during chemical weathering, which should in concept include terrestrial weathering and (2) high temperature hydrothermal exchanges. In both cases, seawater is assumed to be interacting with minerals with a composition similar to MORB glass ($\delta^{18}O$=5.60‰; $\Delta^{17}O$=0.01‰, C=0.5305) (Pack and Herwartz, 2014). It is argued that high temperature exchanges would have a higher value of θ (assumed 0.527) and will lead to higher seawater $\delta^{18}O$ values and that the low temperature exchanges would have a lower value of θ (assumed 0.523) and will lead to lower seawater $\delta^{18}O$ (Pack and Herwartz, 2014). The expectation of high θ values for high temperature processes and low θ can be justified theoretically in a general, but not absolute, way (Cao and Liu, 2011) (Chapter 1). As a result of these two general processes, the triple oxygen isotope composition of seawater at any given time exists in a steady state dictated by the relative contributions of high and low temperature mineral-water interactions. Although this is a simple model representing a truly complex system, it is a first step toward determining the history of seawater $\Delta'^{17}O$.

For meteoric waters, $\Delta'^{17}O$ is determined by equilibrium between liquid water and vapor, the kinetic isotope effect contribution to evaporation which is a function of relative humidity, the effects of Rayleigh distillation and the isotope composition of seawater (Bao et al., 2016). Generally this leads to the relationship $\Delta\delta'^{17}O=0.528\ \Delta\delta'^{18}O$ for the average comparison of any two meteoric waters with meteoric waters having a higher $\Delta'^{17}O$ value than seawater relative to VSMOW (Bao et al., 2016). This relationship is valid for the modern Earth system, but is a function of climate particularly for times of very low global mean average temperatures. The most dominant factor controlling the $\Delta'^{17}O$ of meteoric waters is the $\Delta'^{17}O$ of seawater for that time period. The history of the triple-isotope composition of seawater, which allows for estimates of the triple isotope composition of all terrestrial waters is a critical endeavor that needs to be undertaken to reduce uncertainties related to the three-isotope geothermometer.

Analytical precisions for $\Delta^{17}O$ have recently been significantly improved due to newly adopted methods of sample processing and purification. For silicates and most simple oxides, fluorination using BrF_5 vapor or F_2 gas is the preferred technique as it can generate 100% yield of O_2 from the sample. Purification of this O_2 to remove NF_3 has allowed modern mass spectrometers to achieve precisions of 0.005‰ for $\Delta^{17}O$. Phosphate minerals can be analyzed in the same manner as simple oxides, but give incomplete oxygen yields for fluorination. As a result, uncertainties in $\Delta^{17}O$ from phosphate minerals are larger than for simple oxides, but have been reported as low as 0.010‰ (Pack et al., 2013). For carbonates, the minerals are first converted to CO_2 using phosphoric acid digestion (Passey et al., 2014). The carbonate from acid digestion is then reacted with hydrogen gas to generate methane and water vapor (Passey et al., 2014). The resulting water vapor is then reacted with CoF_3 to yield O_2 which is then purified and

analyzed (Passey et al., 2014). Precisions for this technique are on the order of 0.010‰ (Passey et al., 2014).

Because the $\Delta\Delta^{17}O$-Temperature curve is approximately linear on the scale of these analytical uncertainties, the uncertainty of temperature determined by the three isotope thermometer can be estimated by simply multiplying the analytical uncertainty by the derivative of $\Delta\Delta'^{17}O$ with respect to temperature. This assumes that the $\Delta'^{17}O$ of water can be constrained with a greater precision than analytical uncertainty. For the carbonate and phosphate mineral thermometers this amounts to an uncertainty of about ±8°C for minerals precipitated at equilibrium near 25°C and larger uncertainties of about ±20°C for minerals precipitated at equilibrium near 100°C. For quartz-$H_2O_{(L)}$, the higher precision for analysis combined with the greater temperature dependence of the three isotope effect allows for precisions of ±3°C for minerals precipitated at equilibrium near 25°C and ±7°C for minerals precipitated at equilibrium near 100°C. This result makes the quartz-$H_2O_{(L)}$ pair the most promising of the three isotope geothermometers.

4.2 Mineral pairs with Hematite and Magnetite

Because of the much smaller values of β exhibited by Hematite and Magnetite, if available, the triple oxygen isotope composition of hematite or magnetite can be used as an alternate to that of water. This method has the primary advantage over the mineral-water technique in that it removes the need for the hard to constrain assumptions on the triple oxygen isotope composition of water and their associated uncertainties. Theoretical calibrations for mineral-magnetite and mineral-hematite geothermometers can be found in figure 9.

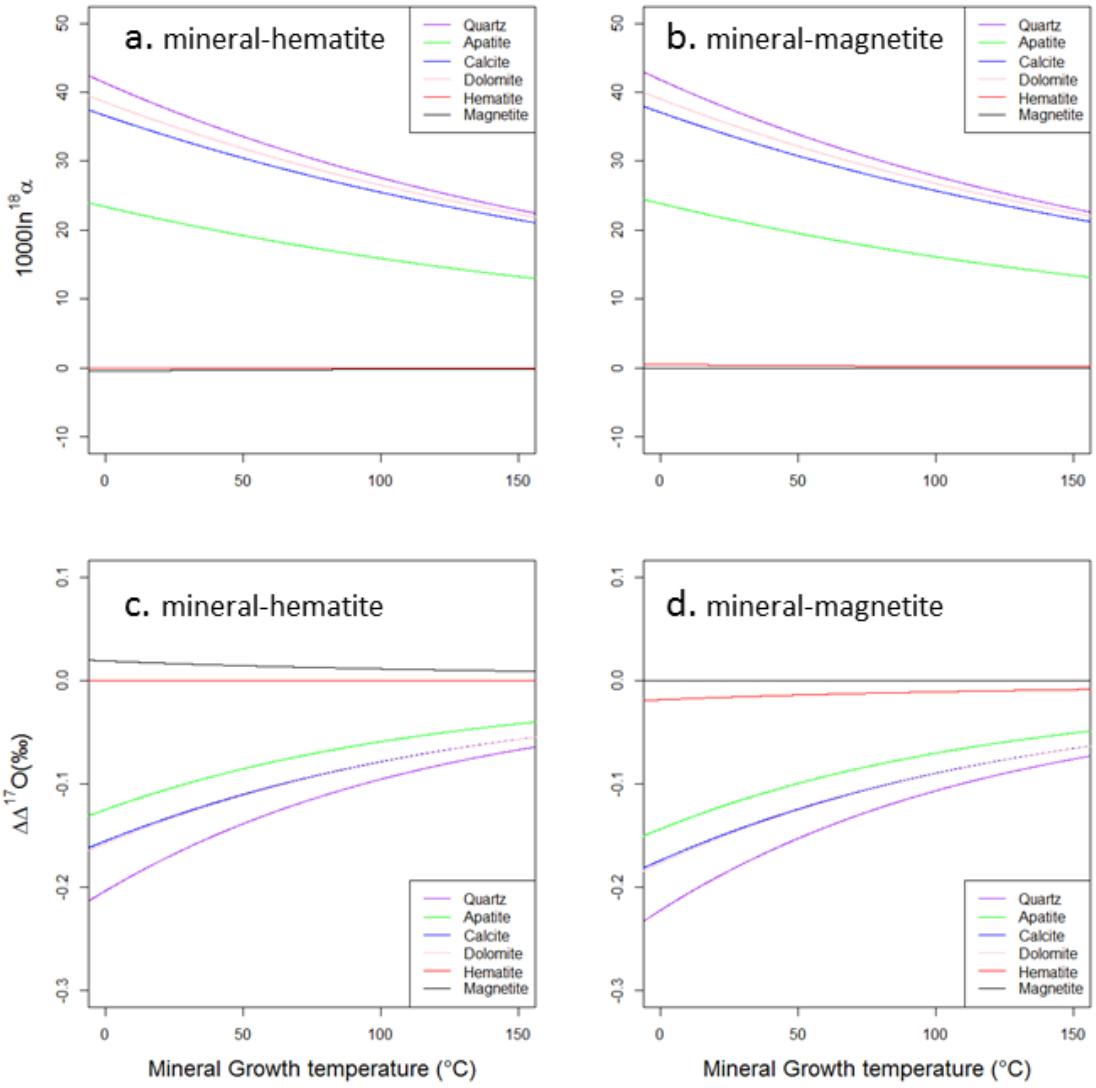

Figure 9. Theoretical results for $\Delta\delta^{18}O$ temperature dependence for a.) Mineral-hematite and b.) Mineral-Magnetite equilibrium; and $\Delta\Delta^{17}O$ temperature dependence c.) Mineral-Hematite equilibrium and d.) Mineral-Magnetite equilibrium

As with any other exchange based mineral-mineral geothermometer, a major concern is on the needed assumption of equilibrium between the two phases. Because the isotopic equilibrium state is very approximately a co-equilibrium for $^{18}O/^{16}O$ and $^{17}O/^{16}O$ (i.e. when $\delta'^{18}O$ is in equilibrium then $\Delta'^{17}O$ is in equilibrium) the theoretical predictions given here can be used as an indicator for equilibrium. This can be done because for a given temperature and mineral pair,

there is only one allowable $\Delta\Delta'^{17}O$ and $\Delta\delta'^{18}O$. If a mineral pair does not yield $\Delta\Delta'^{17}O$ and $\Delta\delta'^{18}O$ values that are valid for any temperature, then it can be confidently stated that these two minerals are not in equilibrium with one another. This is a particular concern with simple oxides like magnetite which can exchange with its environment at relatively low hydrothermal to metamorphic temperatures.

4.3 Comparison of Quartz- $H_2O_{(L)}$ model to previous literature

Currently, fractionation curves for three isotope relationships are rare in the literature. The most robust work to date on the three isotope fractionation relationship for a mineral-water system is the work of Sharp et al. (2016) which provided a calibration for the three-isotope silica-water thermometer based on measurements of natural samples of quartz, amorphous silica sinter and diatoms (opaline silica). Using results from previous work as well as new samples with temperature constraint, Sharp et al. (2016) calculated a curve for silica-water $^{18}O/^{16}O$ fractionation as a function of temperature. Figure 8 shows a comparison our new theoretical results for quartz-water equilibrium with the results of Sharp et al. (2016) as well as curves from Sharp and Kirschner (1994), Meheut et al. (2007) and Zheng (1993). There is a near perfect fit between the new theoretical prediction and the results of Sharp et al. (2016) for $^{18}O/^{16}O$ fractionation even well beyond the temperature range shown. The good fit between the new theoretical results and the curve given by Sharp et al. (2016) is only made possible by the incorporation of the anharmonic correction to the model for liquid water.

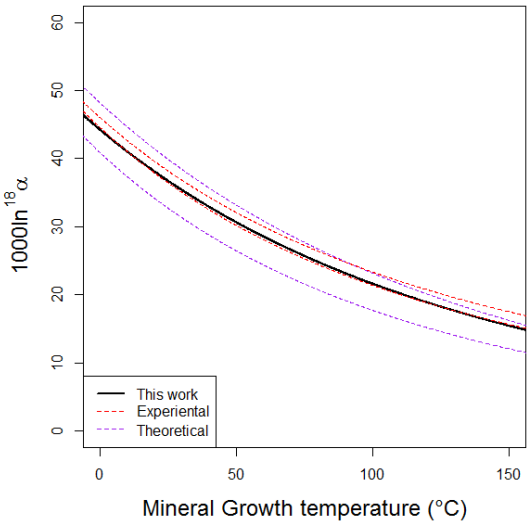

Figure 8. Theoretical results for 1000ln($^{18}\alpha$) temperature dependence for Quartz-H2O$_{(L)}$ equilibrium (Black solid line) with the empirical curves (red dotted lines) from Sharp et al. (2016) and Sharp and Kischner (1994) as well as theoretical curves (purple dotted lines) from Meheut et al. (2007) (upper) and Zheng (1993) (lower). The new theoretical results are a near exact fit to the empirical curve given by Sharp et al. (2016).

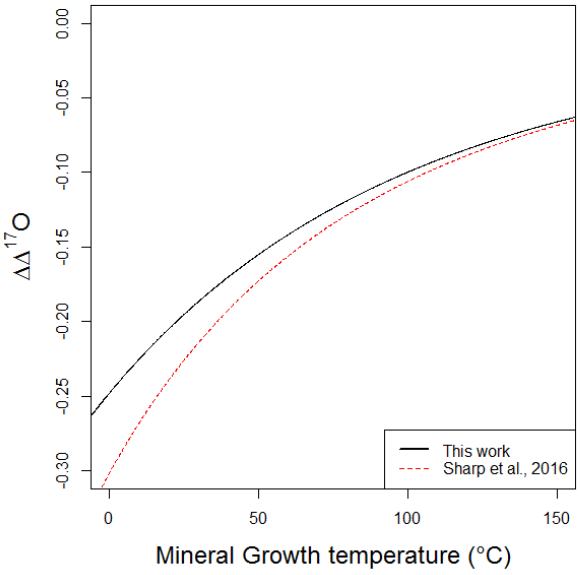

Figure 9. Theoretical results for 1000ln($^{18}\alpha$) temperature dependence for Quartz-H2O$_{(L)}$ equilibrium (Black solid line) with the empirical curves from Sharp et al. (2016) (red dotted line)

The fit of the new quartz-water theoretical results to the $\Delta\Delta^{17}O$-T relationship from results from Sharp et al. (2016) is not quite as good as for $^{18}O/^{16}O$ fractionation (Figure 9). This is likely because their θ-T curve is based on five samples, three diatom samples, a sinter sample and one chert sample. Because the temperatures for all but one of these samples was determined based on the temperature given by the $^{18}O/^{16}O$ ratio, there is an inherent assumption that these samples were precipitated in equilibrium. The discrepancy between the two can be explained if the $\delta^{18}O$ values of the samples used for the θ-T relationship in Sharp et al. (2016) were partially influenced by a normal kinetic isotope effect rather than having been precipitated in true equilibrium with its environment. The inclusion of a small partial normal kinetic isotope effect would cause the calculated temperatures of the samples to be artificially high. However, this would not explain the results for their hydrothermal sinter sample which has a measurement of the water temperature (47 °C) and gives a calculated $\Delta\Delta^{17}O$ value lower than the values predicted here. It is possible that this sample's value could instead be explained by variability in the $\Delta^{17}O$ of the hydrothermal water which it precipitated from (Sharp et al., 2016).

4.4 Implications for 2.5 Ga Seawater

In an attempt to determine the variability of small $\Delta^{17}O$ deviations in sedimentary rocks, Levin et al. (2014) analyzed a collection of chert, oxide and whole rock samples for triple oxygen isotope compositions. Among these samples, six were 2.5 Ga cherts from the Kamden Iron formation in the Transvaal Supergroup, South Africa (Levin et al., 2014). They noted that these samples stood out from the other younger chert samples in that they yielded much lower $\delta^{18}O$ values (~21‰ VSMOW as opposed to ~31‰) but similar $\Delta^{17}O$ (~ -0.25‰ VSMOW) values (Levin et al., 2014). These samples are particularly important for Earth's history because the oxygen isotope composition of similar chert samples have been used to justify extremely

high ocean temperatures (52°C-85°C) for parts of the Archean to Mid-Proterozoic (Knauth and Epstein, 1976; Knauth and Lowe, 2003).

Based only on the $\delta^{18}O$ values of the 2.5 Ga chert samples, an unreasonably high sample average temperature of 100.5°C for the 2.5 Ga ocean is calculated using the calibration provided here assuming that the cherts precipitated in equilibrium with seawater and that the 2.5 Ga seawater isotope composition is similar to the modern ocean ($\delta^{18}O \approx 0‰$ VSMOW). Although the idea of boiling 2.5 Ga oceans is interesting, two explanations are more likely: (1) the oxygen isotope composition of these samples is the result of later alteration which was noted as one of four possibilities in Levin et al (2014). (2) The chert samples were in equilibrium with seawater but the oxygen isotope composition of the 2.5 Ga seawater was far from that of modern seawater. Indeed, with the new theoretical calibration for quartz-water equilibrium, it can be shown that the assumptions that the chert samples reflect equilibrium with the 2.5 Ga seawater and that the 2.5 Ga seawater has an isotope composition similar to the modern oceans are incompatible. Rather than interpret that the oxygen isotope composition of these samples is the result of later alteration, here the possibility is investigated that these chert samples do reflect equilibrium with the 2.5 Ga ocean under the assumption that the chert-water fractionation curve is effectively equivalent to the quartz-water fractionation curve. This assumption is justified using the work of (Sharp et al., 2016). Using these assumptions, possible combinations of temperature and triple oxygen isotope composition of 2.5 Ga seawater can be determined.

Table 1: Results from 2.5 Ga cherts from Levin et al. (2014). The values given in the original study are calibrated to VSMOW for the $\delta^{18}O$ and Gore Mountain Garnet (UWG-2) for the $\Delta^{17}O$. Their results have been recalibrated to VSMOW using their analysis of UWG-2 and the underlined values given in Bao et al. (2016). The bolded average values are used for estimates of 2.5 Ga seawater parameters

Sample Name	**Description**	**$\delta'^{17}O$ (‰) VSMOW**	**$\delta'^{18}O$ (‰) VSMOW**	**$\Delta'^{17}O$ (‰) VSMOW**
GKF-896.22	2.5 Ga Chert	10.606	20.456±0.6	-0.246±0.05
GKF-896.38	2.5 Ga Chert	11.063	21.305±0.2	-0.239±0.015
GKF-896.51g	2.5 Ga Chert	11.314	21.815±0.57	-0.259±0.067
GKF-896.51Y	2.5 Ga Chert	10.709	20.679±0.61	-0.261±0.01
GKF-897.10	2.5 Ga Chert	11.142	21.508±0.84	-0.268±0.055
GKF-897.42	2.5 Ga Chert	11.575	22.347±0.03	-0.28±0.005
Average		**11.0680**	**21.352±-0.26**	**-0.259±0.034**
UWG-2	Garnet	2.986	5.825	-0.104±0.052

The equations used to constrain the values for 2.5 Ga seawater using the averaged chert results are simple to apply. These are given by:

$$\delta'^{18}O_{water} = \delta'^{18}O_{chert} - \Delta\delta'^{18}O_{quartz-water} \quad (10)$$

$$\Delta'^{17}O_{water} = \Delta'^{17}O_{chert} - \Delta\Delta'^{17}O_{quartz-water} \quad (11)$$

$$\Delta\delta'^{18}O_{quartz-water} = \ln(^{18}\beta_{quartz}) - \ln(^{18}\beta_{water}) \quad (12)$$

$$\Delta\Delta'^{17}O_{quartz-water} = \Delta\delta'^{17}O_{quartz-water} - 0.5305 * \Delta\delta'^{18}O_{quartz-water} \quad (13)$$

In these equations, $\delta'^{18}O_{chert}$ and $\Delta'^{17}O_{water}$ are taken to be the averages of the respective values and the β values are functions of temperature given above. Using the combination of these equations, the calibration given in this study and the results from Levin et al. (2014), it is possible to constrain allowable combinations of $\delta'^{18}O_{water}$, $\Delta'^{17}O_{water}$ and temperature Plots of the curves giving these constraints are given in figure 10.

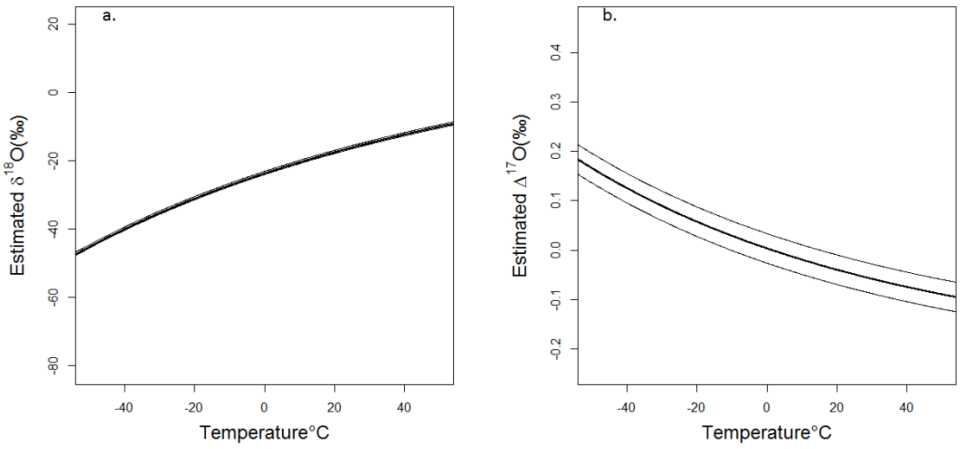

Figure 10. Estimated constraints for the $\delta^{18}O$ and $\Delta^{17}O$ of 2.5 Ga seawater as a function of possible temperatures based on the analysis of chert samples from Levin et al. (2014) and the quartz-water equilibrium model presented here. Secondary lines give the uncertainty of the constraint calculated from the 1σ analytical uncertainty.

The $\delta^{18}O$, $\Delta^{17}O$ of 2.5 Ga seawater can be further constrained with consideration of the Earth system in the late Archean. Based on REE patterns, Kamber (2010) suggests that the Archean Earth's surface was composed of 20% reactive volcanic plateaus, as opposed to the modern 3%. Using the model of Pack and Herwartz (2014), this additional amount of weatherable material would lead to a dramatically higher contribution to from low temperature weathering relative to the modern scenario and as a result, a higher $\Delta'^{17}O_{water}$ than modern oceans. Calculating how much higher is a more in depth exercise, but at this basic level, this rules out temperatures above 1°C (15°C considering analytical uncertainty) for the 2.5 Ga

seawater which these chert samples are assumed reflect equilibrium with. This temperature is significantly lower than previous estimated based on the $\delta^{18}O$ alone for similar chert samples (Knauth and Epstein, 1976; Knauth and Lowe, 2003). This in turn can be used to determine that the $\delta'^{18}O$ of 2.5 Ga seawater must be less than -23.8‰ (-19.6‰ considering analytical uncertainty). These are constraints that are provided by the $\Delta^{17}O$ results but not the more traditional $\delta^{18}O$ results. At this stage, the model for determining the three isotope composition in this manner is under-constrained. With the addition of more results for different minerals (e.g. hematite, magnetite, calcite, dolomite, apatite etc.) it will be possible to constrain the three isotope composition as well as the temperature of seawater for any time period.

5. CONCLUSION

In this study, calibrations for several potential mineral-water and mineral-mineral three isotope thermometers are presented. The results presented here compare well with previous for $^{18}O/^{16}O$ fractionation where data is available. Of the models given here, pairs of quartz, calcite, dolomite and fluorapatite with water, hematite and magnetite show promise as three isotope thermometers with acceptable uncertainties for earth surface and low-T hydrothermal environments. The calibrations provided here, when used in conjunction with the $\Delta\delta^{18}O$ calibrations, can help to determine if a sample is not in isotopic equilibrium with its environment. When combined with the assumption of equilibrium, with this concept it is possible to constrain the temperature and $\delta^{18}O$ of seawater for any time in Earth's history. It is roughly shown here using previous measurements of 2.5 Ga chert samples and the assumption that these chert samples reflect equilibrium with seawater that the temperature of that seawater is lower than 1°C with a $\delta'^{18}O$ lower than -23.8‰.

There is a critical need to determine the history of seawater $\Delta'^{17}O$ on geological timescales. At this time there is a lack of research on this front. The calibrations provided here with appropriate marine samples, make it possible to start constraining seawater. The process of determining the history of seawater $\Delta'^{17}O$ using the presented calibrations will incidentally result in a history of seawater $\delta'^{18}O$ that is better constrained and more reliable than two-isotope techniques alone.

CHAPTER 3: KINETIC ISOTOPE EFFECTS ASSOCIATED WITH REDUCTION AND RE-OXIDATION OF CERIUM OXIDE UNDER CONTROLLED CONDITIONS

PREFACE

This work was completed prior to the developments in Bao et al. (2015) and Chapter 1. As a result this work utilized the concept of a "canonical" range of θ as an assumption to constrain mass dependence rather than a finite range of $\Delta\Delta^{17}O$. In addition, it is also assumed that the θ value for the kinetic processes described in this study is lower than would be expected for equilibrium processes which should not strictly be true according to the work in Chapter 1. The result of this work is that the associated fractionations are large. Because of this, modification of the equations is not critical and the results should still be valid within uncertainty. This work was published in *Geochimica et Cosmochimica Acta*.

ABSTRACT

Ceria (CeO_2) is a heavily studied material in catalytic chemistry for use as an oxygen storage medium, oxygen partial pressure regulator, fuel additive, and for the production of syngas, among other applications. Ceria powders are readily reduced and lose structural oxygen when subjected to low pO_2 and/or high temperature conditions. Such dis-stoichiometric ceria can then re-oxidize under higher pO_2 and/or lower temperature by incorporating new oxygen into the previously formed oxygen site vacancies. Despite extensive studies on ceria, the mechanisms for oxygen adsorption-desorption, dissociation-association, and diffusion of oxygen species on ceria surface and within the crystal structure are not well known. We predict that a large kinetic oxygen isotope effect should accompany the release and incorporation of ceria oxygen. As the first attempt to determine the existence and the magnitude of the isotope effect, this study

focuses on a set of simple room-temperature re-oxidation experiments that are also relevant to a laboratory procedure using ceria to measure the triple oxygen isotope composition of CO_2.

Triple-oxygen-isotope labeled ceria powders are heated at 700°C and cooled under vacuum prior to exposure to air. By combining results from independent experimental sets with different initial oxygen isotope labels and using a combined mass-balance and triangulation approach, we have determined the isotope fractionation factors for both high temperature reduction in vacuum ($\sim 10^{-4}$ mbar) and room temperature re-oxidation in air. Results indicate that there is a 1.5‰±0.8‰ increase in the $\delta^{18}O$ value of ceria after being heated in vacuum at 700°C for one hour. When the vacuum is broken at room temperature, the previously heated ceria incorporates 3% to 19% of its final structural oxygen from air, with a $\delta^{18}O$ value of 2.1‰ (−4.1‰; +7.7‰) for the incorporated oxygen. The substantial incorporation of oxygen from air supports that oxygen mobility is high in vacancy-rich ceria during re-oxidation at room temperature. The quantified oxygen isotope fractionation factors are consistent with the dissociation of O_2 and association of atomic oxygen species at the surface of ceria being the main rate-limiting steps during ceria oxidation and reduction, respectively. While additional parameters may reduce some of the uncertainties in our approach, this study demonstrates that isotope effects can be an encouraging tool for studying oxygen transport kinetics in ceria and other oxides. In addition, our finding warns of the special cares and limits in using ceria as an exchange medium for laboratory triple oxygen isotope analysis of CO_2 or other oxygen-bearing gases.

1. INTRODUCTION

Ceria (CeO_2) is a fluorite-type oxide that has been studied and used extensively as an oxygen storage media in three-way catalysts (Trovarelli et al., 1999), as an oxygen partial

pressure regulator (Laachir et al., 1991; Perrichon et al., 1994; Trovarelli et al., 2001), as a fuel additive for the reduction of soot (Lahaye et al., 1996), for the removal of organics from wastewater (Matatov-Meytal and Sheintuch, 1998), and as a fluid cracking catalyst (Trovarelli et al., 1999). In addition, ceria is used in solid oxide fuel cells (SOFCs) (Chueh, 2011) and has shown potential for the production of syn-gas from water and CO_2 (Chueh et al., 2010; Chueh and Haile, 2010). It has been known for over half a century that exposing ceria to low pO_2 and/or high temperature conditions will partially reduce ceria (Bevan, 1955; Bevan and Kordis, 1964). At temperatures above 626°C ceria can undergo thermal decomposition to a more reduced state (Paparazzo et al., 1991). In addition, storage under ultra-high vacuum condition is known to induce the formation of oxygen site vacancies in ceria (Zhang et al., 2004). Oxygen vacancies in ceria are thought to be dominantly in the form of anion site Frenkel defects created through the generalized reaction:

$$O_O \rightarrow V_O^{\cdot\cdot} + O_i'' \quad (1)$$

where O_O is an oxygen atom in an oxygen site, $V_O^{\cdot\cdot}$ is a positively charged vacancy in the oxygen sub-lattice, and O_i'' is a negatively charged interstitial oxygen atom (Walsh et al., 2011). The key to ceria's behavior is a ready conversion between its Ce^{4+} and Ce^{3+} oxidation states (Demoulin et al., 2007; Graciani et al., 2011; Perrichon et al., 1994). To maintain overall electroneutrality, each newly formed oxygen vacancy and loss of an oxygen atom is balanced by the reduction of two Ce^{4+} atoms to Ce^{3+} (Chueh, 2011).

$$2Ce_{Ce} + O_O \leftrightarrow 2Ce'_{Ce} + V_O^{\cdot\cdot} + \frac{1}{2}O_{2(g)} \quad (2)$$

When exposed to a lower temperature or higher pO_2 environment, partially reduced ceria will re-oxidize and fill its oxygen vacancies. When the oxidants are H_2O or CO_2, H_2 or CO will

be generated, respectively (Sharma et al., 2000; Singh and Hegde, 2010). This remarkable redox reversibility has resulted in ceria being one of the most studied oxide materials.

Multiple kinetic steps have been proposed for the dynamic redox processes involving ceria or mixed ceric oxides and gaseous O_2 or CO_2 (Duprez, 2006; Galdikas et al., 2004; Holmgren and Andersson, 1998; Holmgren et al., 1999; Madier et al., 1999; Sadovskaya et al., 2007). Two key sets of kinetic steps involved in the reduction and re-oxidation of ceria are: (1) dissociative adsorption and associative desorption of the oxygen-bearing oxidant molecule (commonly O_2) on ceria surface, and (2) diffusion of atomic oxygen within the bulk structure of ceria through a vacancy hopping mechanism (Figure 1). At higher temperatures, surface reactions are believed to be much slower than the bulk oxygen diffusion and are therefore the rate limiting steps (Chueh, 2011; Chueh and Haile, 2010; Duprez, 2006; Holmgren et al., 1999).

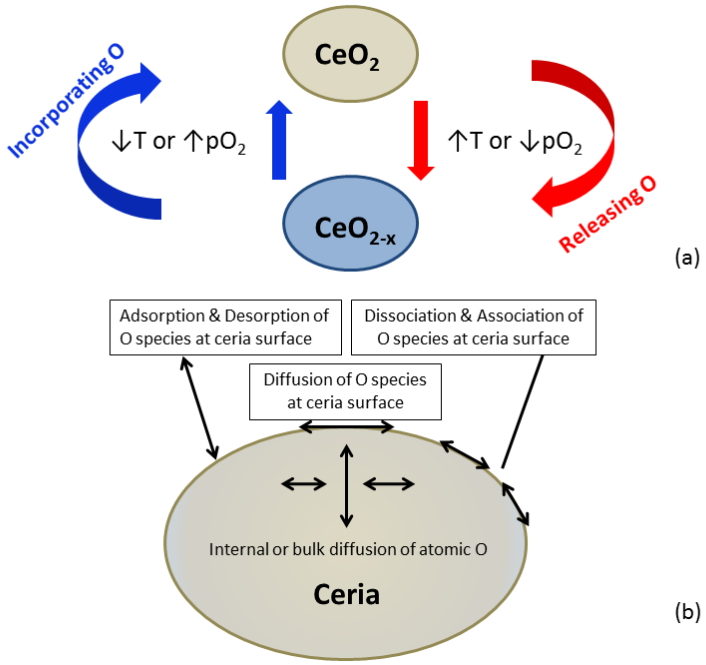

Figure 1. (a) Ceria redox cycle and (b) potential kinetic steps involved.

Studies on oxygen transport kinetics between ceria or mixed ceric oxides and O_2 or CO_2 have been conducted for decades. The methods employed include (1) stable oxygen isotope labeling with either subsequent depth profiling and imaging of ^{18}O tracer diffusion in oxides by Secondary Ion Mass Spectrometry (SIMS) (De Souza et al., 2005; Fielitz and Borchardt, 2001; Kilner et al., 2011; Lane and Kilner, 2000; Manning et al., 1997; Perkins et al., 2001; Salazar-Villalpando, 2012; Yashiro et al., 2002) or by subsequent isotope analysis of the evolving O-bearing gases (Anan'ev et al., 2012; Bedrane et al., 2005; Bouwmeester et al., 2009; Cunningham et al., 1999a; Cunningham et al., 1999b; Dong et al., 2004; Duprez, 2006; Gorelov and Kurumchin, 1987; Madier et al., 1999), (2) measuring electrical and ionic conductivity (Park and Choi, 2008; Waldhausl et al., 2012; Wang et al., 2012), and (3) gravimetric methods (Katsuki et al., 2002; Stan et al., 2004). The different methods have their own merits. Even within the oxygen isotope labeling approach, gas-phase analysis has a purported advantage over depth profiling because it offers mechanistic information on oxygen exchange at the oxide surface (Anan'ev et al., 2012; Bouwmeester et al., 2009).

Thus far, the stable isotope studies on oxygen transport kinetics involve the use of a highly enriched ^{18}O or ^{17}O tracer (Klier et al., 1963). In these studies isotope fractionation or the isotope effect, a small enrichment of one isotope relative to another in a chemical or physical process, is ignored. The present study, however, examines the degree and sign of these small enrichments or the oxygen isotope effects during the redox cycling of ceria. The isotope effect reveals reaction mechanisms at a quantum chemical level, providing independent mechanistic insights that an enriched ^{18}O tracer often cannot reveal, as demonstrated in the study of O_2 coordination to reduced transition metals and cleavage of the O-O bond in biochemical processes (Ashley et al., 2010). In this study, we focus on a simple set of room-temperature re-oxidation (RTRO)

experiments starting with triple-oxygen-isotope labeled ceria powders. Combining the results from independent sets of experiments with different initial oxygen isotope labels and applying a combined mass-balance and triangulation approach, we have determined the fraction of new oxygen being incorporated and the apparent non-equilibrium isotope fractionation factors for both the reduction and re-oxidation of ceria. Our study is the first to quantify oxygen isotope effects for the redox processes of ceria. The magnitudes of isotope fractionation, as determined here, can act as a guidepost for future exploration of the isotope effect involving oxygen transport in ceria, in diverse mixed oxides, or in material sciences in general.

Here we specifically focus on ceria's reduction at 700°C and re-oxidation at room temperature (i.e. 22°C or 295K), a temperature much lower than that used in most previous experimental studies on ceria-gas exchange. This choice of experimental conditions is due to a newfound utility for ceria within the stable isotope community as an oxygen exchange medium for the triple oxygen isotope measurement of an oxygen-bearing gas such as CO_2 (Assonov and Brenninkmeijer, 2001; Hofmann et al., 2012; Hofmann and Pack, 2010; Mahata et al., 2012). If re-oxidation of ceria can indeed occur at room temperature, as proposed by many earlier studies (Bevan and Kordis, 1964; Laachir et al., 1991; Namai et al., 2003; Perrichon et al., 1994; Staudt et al., 2010), we suspect that the high-temperature state of interest from the oxygen exchange procedure, and its associated oxygen isotope composition, will not remain intact after handling of ceria in air at room temperature. Therefore, there is a practical urgency to verify this suspicion.

2. THE ROOM TEMPERATURE REOXIDATION (RTRO) EXPERIMENT, PROPOSED MODEL, AND EXPECTED ISOTOPE EFFECTS

2.1 Experiment

There have been many experiments involving reduction and re-oxidation of ceria that normally occur, as a necessity, in non-isothermal conditions. Quantification of isotope fractionation during non-isothermal processes involves additional assumptions and complex mathematical treatments that often have no simple analytical solutions (Flynn, 1997; Vyazovkin and Wight, 1998). Here we focus our test on one particular experiment design with a minimum number of non-isothermal steps involved. In this room-temperature re-oxidation (RTRO) experiment (Fig. 2), ceria powder is heated at 700°C for one hour under vacuum while continuously pumping and then cooled to room temperature (22°C) under vacuum prior to exposure to air. The heating process is inevitably non-isothermal because heating must progress from 22°C to 700°C, but this period is relative short compared to the total 1 hour heating duration. After cooling to 22°C in vacuum, the ceria is exposed to a sudden increase of pO_2 upon the break of vacuum and exposure to ambient air, during which re-oxidation may occur to ceria isothermally at 22°C. This RTRO experiment is similar to the cooling procedure for the ceria-CO_2 isotope exchange experimental method developed as an easier means for measuring triple oxygen isotope composition of CO_2, an otherwise difficult gas to analyze (Hofmann and Pack, 2010). Thus, this experiment will allow us to examine if re-oxidation occurs to ceria upon the break of vacuum at room temperature in the laboratory.

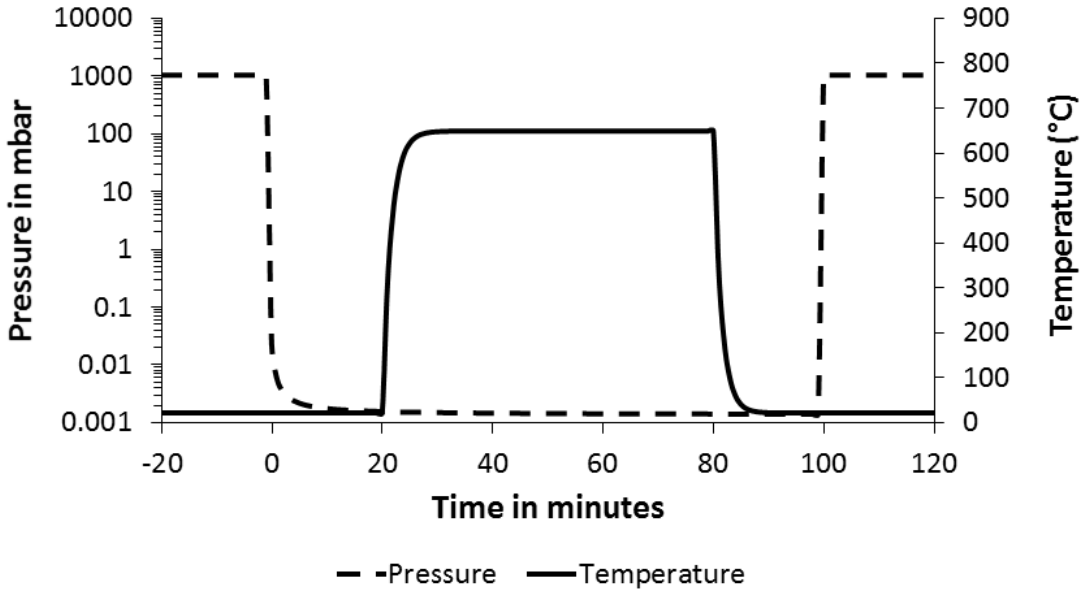

Figure 2. Pressure & Temperature vs. Time in the RTRO experiment. Heating and cooling rates are approximated based on measured changes in the external temperature of the quartz-glass reaction chamber.

2.2 Model and Predictions

During the heating stage, oxygen is released from the ceria crystal structure. Once at 700°C, there may be a release of oxygen initially but the net release will decreases to zero once ceria reaches equilibrium with the residual oxygen in the vacuum. At this state, oxygen exchange with residual oxygen species in the vacuum cannot cause a change in the oxygen isotope composition of the ceria because the amount of oxygen present in the vacuum is magnitudes less than the amount of oxygen present in the ceria powder (~60 μmol). The partial loss of structural oxygen during the effectively unidirectional reduction reaction will produce a mass-dependent

change in the triple oxygen isotope composition of the remaining ceria structural oxygen. During cooling in a high vacuum, negligible oxygen gain or loss is expected and the oxygen isotope composition of the ceria will be unchanged. Once cooled and stabilized at 22°C, the vacuum is broken, and pO_2 increases several magnitudes. The thermodynamic drive at this step favors the re-oxidation of ceria and new oxygen is incorporated into the crystal structure from air. Similar to the reduction step, the oxygen utilized for re-oxidation of the ceria is expected to be mass dependently fractionated from its source.

If heating and cooling steps are conducted above the exchange closure temperature in an oxygen-bearing gas, given sufficient time, forward and reverse fluxes would eventually balance and result in oxygen isotope equilibrium between solid ceria and the oxygen-bearing gas. However, when heating and cooling are conducted in vacuum, like in the RTRO experiment, forward and reverse fluxes will not be balanced and the rate-limiting step(s) will play a pronounced role in the rate of oxygen transport, resulting in an isotope effect which may change with the heating and cooling rates. As the first attempt to explore the isotope effect in ceria's redox processes, our model and its predictions are largely qualitative.

3. TESTING STRATEGY --THE MASS-BALANCE AND TRIANGULATION APPROACHES

The predicted isotope effect can be tested by monitoring the triple oxygen isotope composition of ceria before and after the RTRO experiment. Quantitatively, we can implement a natural-abundance triple-oxygen isotope label for the initial ceria. The fraction of new oxygen incorporated into the ceria structure after the RTRO experiment can be solved for by mass balance. With multiple experimental sets of the measured triple oxygen isotope composition for the initial and the final ceria, we can solve for the apparent isotope fractionation factors

associated with (1) ceria reduction or the release of O species from ceria powders during heating up to and at 700°C and (2) ceria re-oxidation or the incorporation of O species at room temperature once the vacuum is broken. The mathematical treatment is illustrated by a graphical triangulation approach in a $\delta^{17}O$-$\delta^{18}O$ plane (Fig. 3) where $\delta^{17}O$ and $\delta^{18}O$ describe the per-mil difference between the sample and the standard (VSMOW). Notation used in the present study can be found in Appendix F.

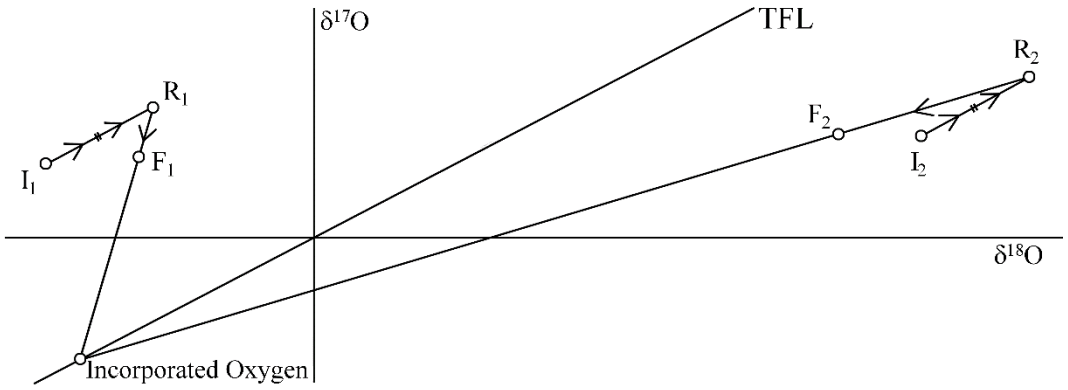

Figure 3. Graphic depiction of the triangulation approach. "I" represents the initial powder, "R" represents the reduced ceria after heating at 700°C in vacuum and "F" the final ceria after re-oxidation in air at 22°C. Two hypothetical sets (1 and 2) are shown in the $\delta^{17}O$-$\delta^{18}O$ plane. Arrows indicate the proposed path that the $\delta^{18}O$ and $\delta^{17}O$ of the ceria powders follow during the RTRO experiment. The TFL as displayed is the terrestrial fractionation line. The incorporated oxygen by ceria during re-oxidation is sourced from air, with incorporated oxygen on or very close to the TFL.

Three variables can be determined from a combined mass balance and triangulation approach: (1) $f_{incorporated}$, the fraction of oxygen incorporated into ceria from the air in final ceria, (2) $\Delta\delta^{18}O_{reduction}$, the $\delta^{18}O$ difference between reduced ceria at 700°C and the initial ceria, and (3) $\delta^{18}O_{incorporated}$, the $\delta^{18}O$ of the incorporated oxygen from air at 22°C. By starting with a ceria of a non-zero $\Delta^{17}O$ value ($\Delta^{17}O = \delta^{17}O - C * \delta^{18}O$), $f_{incorporated}$ can be obtained through mass balance using the $\Delta^{17}O$ values of the initial and final ceria (Eq. 3):

$$f_{incorporated} = \frac{\Delta^{17}O_{Final} - \Delta^{17}O_{Initial}}{\Delta^{17}O_{air} - \Delta^{17}O_{Initial}} \quad (3)$$

Equation 3 is derived from the mixing equations for the $\delta^{18}O$ and $\delta^{17}O$. Derivation and discussion on this equation can be found in Appendix G. Mixing using $\Delta^{17}O$ values is valid because of (1) the mass dependent nature of thermally driven reactions (Young et al., 2002) and (2) the near linearity of $\delta^{18}O$ and $\delta^{17}O$ mixing over the ranges utilized in our experiments. Both $\delta^{18}O$ and $\delta^{17}O$ may change because of potential loss of structural oxygen from ceria during heating in vacuum. However, the $\delta^{18}O$ and $\delta^{17}O$ will change in a predictable, mass-dependent manner, such that any oxygen loss during vacuum heating will not change ceria's $\Delta^{17}O$ value. In contrast, because the incorporated oxygen can only be sourced from air, and air's components have $\delta^{18}O$ and $\delta^{17}O$ values that lie on or near the terrestrial fractionation line (TFL), the incorporation of new oxygen is capable of changing the $\Delta^{17}O$ of the final ceria toward the $\Delta^{17}O$ value of air oxygen. This change in $\Delta^{17}O$ can be observed if the initial ceria is labeled with an oxygen isotope composition that does not lie near the TFL line (i.e. $\Delta^{17}O \neq 0$). Here we deliberately use the unspecific term "air oxygen" because our experiment does not conclusively exclude any of the three major oxygen-bearing species in air, O_2, CO_2, and water vapor, as the source of the O incorporated into ceria after vacuum is broken at 22°C. For the calculations as presented in the main text, air O_2 ($\Delta^{17}O$=-0.23‰ for C=0.52) is the assumed sole oxidizer (Bao et al., 2008).

For each sample pair of initial and final ceria data, one equation can be written with two unknowns, $\Delta\delta^{18}O_{reduction}$ and $\delta^{18}O_{incorporated}$:

$$\frac{\delta^{17}O_{Final} - (\lambda_{incorporation} * \delta^{18}O_{incorporated} + \Delta^{17}O_{air})}{\delta^{18}O_{Final} - \delta^{18}O_{incorporated}} = \frac{(\lambda_{reduction} * \Delta\delta^{18}O_{reduction} + \delta^{17}O_{Initial}) - \delta^{17}O_{Final}}{(\Delta\delta^{18}O_{reduction} + \delta^{18}O_{Initial}) - \delta^{18}O_{Final}} \quad (4)$$

To constrain these two unknowns, two sets of identical experiments that have different triple oxygen isotope compositions for the initial ceria powders are required. Detailed derivation of equation (4) for solving $\Delta\delta^{18}O_{reduction}$ and $\delta^{18}O_{incorporated}$ can be found in Appendix H. Sample sets that utilize the same starting powders are not used together for solving the two variables because the related equations are not independent. The values of $\delta^{18}O_{incorporated}$ and $\Delta\delta^{18}O_{reduction}$ are unknown prior; therefore, initial ceria powders are generated to cover different quadrants of the $\delta^{17}O$-$\delta^{18}O$ space.

Once multiple sets of experimental data are obtained, a finite number of two-pair combinations can be achieved, and thus a finite number of solutions for $\delta^{18}O_{incorporated}$ and $\Delta\delta^{18}O_{reduction}$ are obtained. A Monte Carlo method is used to analyze the calculation errors.

4. METHODS

The experiment involves preparing ^{17}O-labeled ceria, heating and cooling ceria in vacuum followed by breaking vacuum at room temperature (RTRO), measuring triple oxygen isotope composition of ceria, and Monte Carlo error analysis.

4.1 Preparation of ^{17}O-labeled CeO_2

^{17}O-labeled ceria powder is generated by exchanging micron-size ceria powder (Aldrich, <5μm, 99.9% trace metals basis) at 700°C with the ^{17}O-labeled CO_2 gas prepared by 48-hour room temperature exchange with ^{17}O-anomalous water. The sole purpose of this procedure is to achieve a ^{17}O-anomalous triple oxygen isotope label on the resulting ceria powder. Specifically, ~40 mg of ceria powder is placed on a gold boat in a 480 mL quartz glass vacuum tube connected to a vessel containing ^{17}O-labeled water. The ^{17}O-labeled water is degassed using a vacuum pump and frozen in an ethanol trap maintained at −40°C to −50°C. The apparatus,

including the tube furnace with ceria powder and the water vessel, are evacuated to baseline pressure with a roughing pump. The apparatus is closed to the pump and the temperature of the ethanol trap is verified to be above the freezing point of CO_2 at 1 bar. CO_2 (99.8% purity) is then released into the apparatus at a pressure of ~650 mbar. The ethanol trap is removed to allow the water to thaw and the apparatus is left at room temperature for 48 hours in order to allow for CO_2-H_2O oxygen isotope exchange.

After 48 hours, the valve to the water vessel is sealed and, to the side, a tube furnace is preheated to 700°C. Once the tube furnace reaches 700°C it is positioned onto the quartz glass vacuum tube over the gold boat and ceria powder, and is left for one hour with periodic pressure and temperature monitoring. At the end of one hour, the CO_2 is pumped to waste and the tube furnace is moved off the quartz glass tube. The ceria powder is allowed to cool to room temperature under vacuum. Once the powder is cool, the reaction chamber is opened to air and the ^{17}O-labeled ceria powder is removed. The resulting ceria powder is placed in a sealed glass bottle and agitated prior to weighing for oxygen isotope analysis and transfer to a gold boat for RTRO experiments.

4.2 Room temperature re-oxidation experiment (RTRO)

Approximately 5 mg of cerium oxide powder with a known triple oxygen isotope composition is placed on a <1mm thick gold boat in a quartz tube in the vacuum line. The triple oxygen isotope composition of the ceria powder is determined by measuring a sample of ceria powder labeled in the same batch. The tube is evacuated with an Edwards air-cooled diffusion pump to below 5×10^{-3} mbar as measured by capacitance manometer. This pressure measurement is at the bottom of the measurement range of the manometer used here. Actual operating pressure is likely more than a magnitude lower than the 5×10^{-3} mbar reading on the gauge. A tube

furnace, which has been preheated to 700°C, is positioned onto the quartz tube containing the ceria powder. After heating under vacuum for one hour, the tube furnace is removed and the powder is allowed to cool to 22°C for 20 minutes prior to exposure to air. This cooling duration is expected to be sufficient to return the ceria to room temperature because the glass vacuum tube reaches room temperature after 8 minutes. The additional time for cooling of the powder is to compensate for the lack of heat loss by convection within the tube. The procedure outlined above is the standard RTRO procedure. Exceptions to this procedure are sample sets 6 and 7, which are allowed to cool for 2 hours and 1.5 hours respectively and sample sets 8, 9 and 10, which utilized a glazed alumina crucible rather than a gold boat.

4.3 Triple Oxygen Isotope Analysis of ceria

Ceria samples, initial and final, are converted to O_2 gas by laser fluorination with bromine pentafluoride (BrF_5) vapor. Prior to oxygen isotope analysis, the ceria powder is subjected to a prefluorination procedure. The ceria is loaded into a reaction chamber, and the chamber is evacuated to below 10^{-3} mbar and heated to 70°C. After 1.5 hours, the heater is turned off and the reaction chamber is allowed to cool to 22°C. Once the chamber is cool, BrF_5 vapor is introduced to the chamber in order to oxidize surface water and organics. The BrF_5 vapor is then frozen in a liquid-nitrogen cooled u-trap and any evolved non-condensable gases from this step are pumped to waste. This is followed by introducing 13 to 20 mbar of BrF_5 to the chamber and leaving the chamber sealed for greater than 8 hours. This prefluorination step ensures that any residual adsorbed water or other removable impurities such as reduced carbon species are eliminated prior to measurement. BrF_5 vapor does not significantly react with cerium oxide at 22°C over this timescale; however, there is a slight but noticeable decrease in final oxygen yield if the ceria powder is stored under these conditions for longer than a week. After the

prefluorination procedure, the BrF_5 remaining in the chamber is collected as waste in a cryogenic trap and any evolved non-condensable gases are pumped away. For conversion to O_2, ~25 mbar of BrF_5 vapor is introduced to the evacuated laser chamber. Energy for the reaction is provided by a New Wave Mir10 CO_2 laser system. This reaction occurs readily at low powers with a consistent oxygen yield at or near 100%. Condensable gases, including unreacted BrF_5, are removed from the resulting gas with a series of liquid nitrogen-cooled u-traps that allow oxygen gas to pass through. The resulting purified O_2 is collected into prepared 5A molecular-sieve sample tube for transfer to an isotope-ratio mass spectrometer (Finnigan MAT 253). The $\delta^{18}O$ and $\delta^{17}O$ are obtained by running in dual inlet mode. A more thorough discussion of this method can be found in (Bao and Thiemens, 2000). The results of oxygen isotope analysis for both the initial and final ceria powders for each experimental set can be found in Table 1. All experiments and analysis were conducted at Louisiana State University.

Table 2: Fourteen sets of measured $\delta^{17}O$ and $\delta^{18}O$, and calculated $\Delta^{17}O$ values (λ=.52) for the initial and final ceria in the LTRO experiments.

	Initial			Final				
Experiment Set	**$\delta^{18}O$**	**$\delta^{17}O$**	**$\Delta^{17}O$**	**$\delta^{18}O$**	**$\delta^{17}O$**	**$\Delta^{17}O$**	**Cooling Duration**	**Crucible material**
Set 1	30.24‰	10.91‰	-4.64‰	28.51‰	10.53‰	-4.14‰	20 min	Gold
Set 2.1	-0.19‰	-0.20‰	-0.10‰	2.11‰	0.99‰	-0.11‰	20 min	Gold
Set 2.2	-0.19‰	-0.20‰	-0.10‰	2.22‰	1.10‰	-0.05‰	20 min	Gold
Set 3.1	-1.29‰	-0.40‰	0.27‰	0.84‰	0.70‰	0.26‰	20 min	Gold
Set 3.2	-1.29‰	-0.40‰	0.27‰	0.96‰	0.81‰	0.31‰	20 min	Gold
Set 4.1	2.09‰	2.06‰	0.97‰	3.58‰	2.79‰	0.92‰	20 min	Gold
Set 4.2	2.09‰	2.06‰	0.97‰	3.67‰	2.86‰	0.95‰	20 min	Gold
Set 5.1	12.54‰	13.83‰	7.26‰	13.43‰	14.11‰	7.08‰	20 min	Gold
Set 5.2	12.54‰	13.83‰	7.26‰	13.12‰	13.54‰	6.67‰	20 min	Gold
Set 6	12.48‰	13.85‰	7.30‰	12.59‰	12.48‰	5.90‰	120 min	Gold
Set 7	7.35‰	2.62‰	-1.19‰	7.94‰	2.94‰	-1.18‰	120 min	Gold
Set 8	30.48‰	10.95‰	-4.73‰	30.25‰	10.91‰	-4.65‰	20 min	Alumina
Set 9	30.48‰	10.95‰	-4.73‰	26.49‰	9.71‰	-3.93‰	20 min	Alumina
Set 10	31.76‰	11.33‰	-4.99‰	29.56‰	10.91‰	-4.30‰	20 min	Alumina

4.4 Monte Carlo calculation and error analysis

Several sets of 7000 normally distributed pseudo-random numbers with an assigned standard deviation and mean are generated using the open source program R (RCoreTeam, 2012). The random numbers are assigned a mean that is equal to the value of the measured sample and a standard deviation of 0.03 for $\delta^{18}O$ and 0.06 for $\delta^{17}O$. These standard deviations are typical of the measurement error and are conservative. In addition, random numbers corresponding to expected values of λ are generated with a mean of .515 and a standard deviation of .005. The deterministic equations are then solved 7000 times using the generated pools of pseudo-random numbers.

The results from the Monte Carlo calculation for the fraction of oxygen incorporated are typically normally distributed; however, distributions of the results for $\Delta\delta^{18}O_{release}$ and $\delta^{18}O_{incorporated}$ are non-normal and heavily skewed. For this reason, the medians (≈mode in this case) of the results are chosen as the more representative estimates. Error is determined using the 15.9^{th} and the 84.1^{th} percentiles as well as the 10^{th} and 90^{th} percentiles. These generate ranges that cover 68.2% and 80% of the results respectively. Best estimates for the values of $\Delta\delta^{18}O_{release}$ and $\delta^{18}O_{incorporated}$ are determined by the median of the compiled calculation results with errors as described above. The error as determined by this method only include the error of the O_2 gas measurement and the error introduced by the calculation. The Monte Carlo error determination procedure used here is similar to that in previous studies (Alper and Gelb, 1990, 1991; Shirk and Hoffman, 1985).

5. RESULTS

With the exception of ceria powders from set 8 and set 7 (Table 1), the ceria samples show a significant change in oxygen isotope composition from the initial to the final ceria. For samples with initial $\delta^{18}O$ values of ~30‰ the $\delta^{18}O$ of the final powder is lower by 2‰ to 4‰. This is in contrast to samples with initial $\delta^{18}O$ values that are closer to 0‰ which see an increase in $\delta^{18}O$ by ~2‰. With the exception of set 8, initial samples with large ^{17}O-anomalies yielded final powders with lower anomalies. The greatest percent change in $\Delta^{17}O$ is seen for set 6 with a 18.8% change. This large shift is not seen for sets 5.1 and 5.2 that use an initial powder from the same batch.

The calculated fraction, $f_{incorporated}$, is highly variable (Fig. 4). Given the uncertainties in $f_{incorporated}$, we conclude that the fraction of incorporated oxygen from air accounts for 3 to 19% (median of 6.9%) of the total oxygen in final ceria for our RTRO procedure. Large errors (>5%) are associated with experiments that have utilized initial ceria with oxygen isotope compositions that lie near the TFL. In addition, repeated analysis of ceria samples before and after storage, including the initial powders used for set 5.1/5.2 and set 6 (Table 1), indicate that the oxygen isotope composition is stable at room temperature even over long periods of storage (>1 month).

Of a total of fourteen data sets, eight have initial ceria powder oxygen isotope compositions that do not lie near the TFL. Of the fourteen experimental sets, sets 8, 9 and 10 utilize a different crucible from the other RTRO experiments. The bulkier alumina crucible used may have a significant effect on the rate of heating of the ceria powder. For this reason these samples may not be comparable to other experimental sets and are omitted from the calculation of $\delta^{18}O_{incorporated}$ and $\Delta\delta^{18}O_{reduction}$. These samples, however, are included in the calculation of the fraction of oxygen incorporated because the $f_{incorporated}$ calculation can be applied to a single

experimental set. When sets with the same initial powder values are not paired and sets that utilize an alumina crucible are omitted, there are 51 total pairs of experimental sets that can be processed for the calculation of $\delta^{18}O_{incorporated}$ and $\Delta\delta^{18}O_{reduction}$. By analyzing the errors associated with results from individual sets using the Monte Carlo method, the most likely values for $\delta^{18}O_{incorporated}$ and $\Delta\delta^{18}O_{reduction}$ are determined.

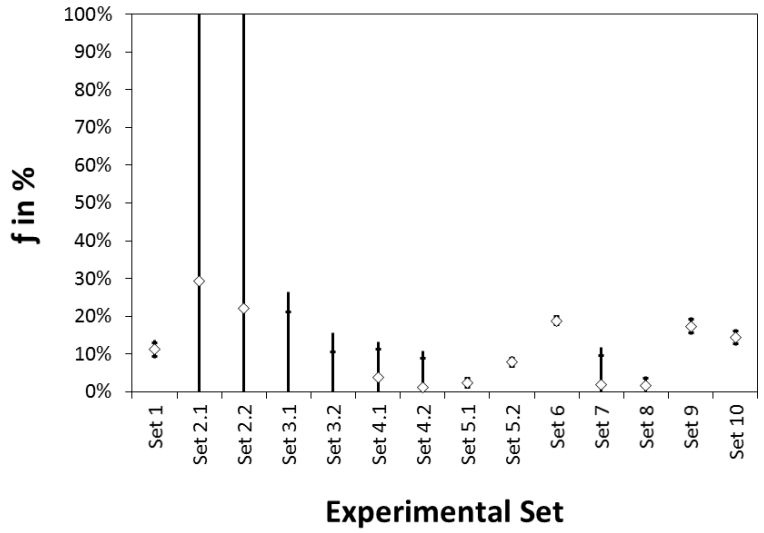

Figure 4. Results of the Monte Carlo calculation for the fraction of oxygen taken into the ceria structure during room-temperature re-oxidation, the $f_{Incorporated}$. Points are the median values of the Monte Carlo calculation results. The inner error bars are the edges of the 15.9-84.1 interpercentile range. The outer error bars are the edges of the 10-90 interpercentile range.

Owing to ideal $\delta^{18}O$ values of some initial ceria powders, some sample combinations yield particularly small errors for the determined values of $\delta^{18}O_{incorporated}$ and $\Delta\delta^{18}O_{reduction}$. This is the case for pairings involving 2.1 and 2.2. Set 2.2-3.2 yields values of $\delta^{18}O_{incorporated}$ = 2.1‰ (+0.2‰; −0.2‰) and $\Delta\delta^{18}O_{reduction}$ = 2.1‰ (+0.2‰; −0.2‰). These results fall within the range of error for most other calculations and should be valid under the assumption that the two experiments progressed identically; however, the values would be very sensitive to experimental

variability. In order to reduce the impact of random experimental variability, the best estimates for $\delta^{18}O_{incorporated}$ and $\Delta\delta^{18}O_{reduction}$ presented here are derived from the compiled calculation results (Fig. 4 and 5).

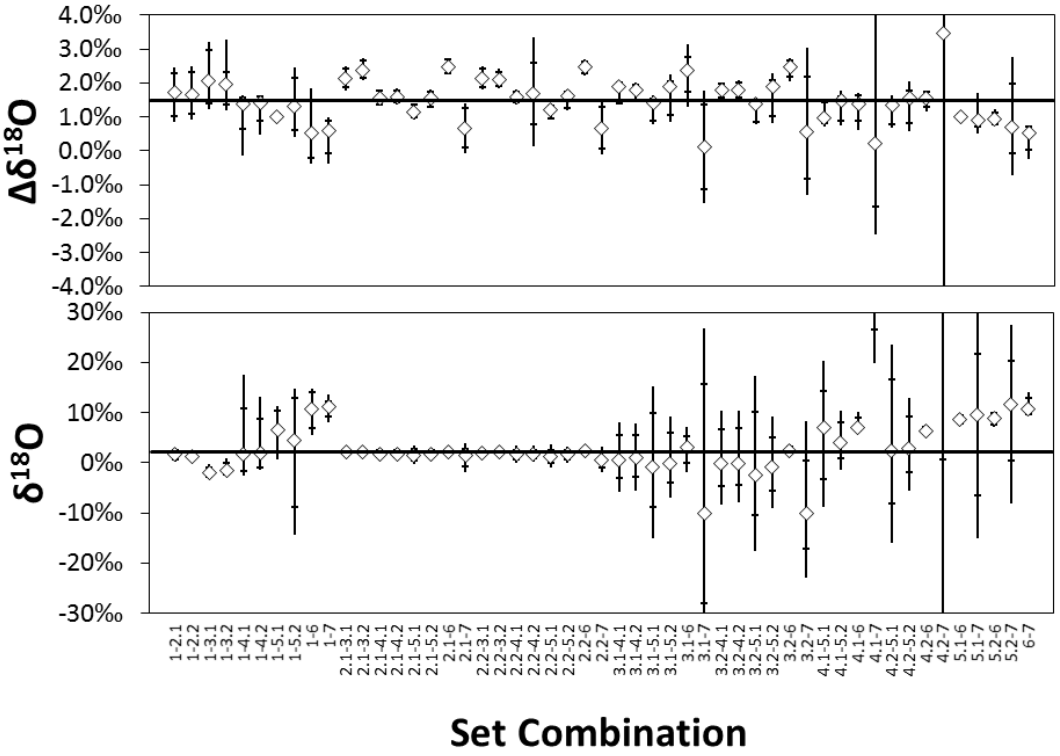

Figure 5: Plot of the Monte Carlo calculation results for $\Delta\delta^{18}O_{reduction}$ as a result of reduction (top) and the $\delta^{18}O_{incorporated}$ of the incorporated oxygen (bottom). Points are the median values of the Monte Carlo calculation results for the corresponding set combinations. The inner error bars are the edges of the 15.9-84.1 interpercentile range. The outer error bars are the edges of the 10-90 interpercentile range. Horizontal lines are plotted for the median values ($\Delta\delta^{18}O_{reduction}$=2.6‰ and $\delta^{18}O_{incorporated}$=1.5‰).

These results indicate that there is a 1.5 ±0.8‰ increase in the $\delta^{18}O$ value of the remaining ceria upon heating in vacuum. When the vacuum is broken at room temperature, the heated and cooled ceria will incorporate 3% to 19% of ceria's final oxygen from air, with a $\delta^{18}O$ of 2.1‰ (+7.7‰; −4.1‰).

6. DISCUSSION

By treating ceria at a high temperature and vacuum condition and then exposing the ceria powder to the atmosphere at room temperature, we see that the resulting ceria oxygen isotope composition has shifted from its initial value. This isotope composition shift is characterized by a trend toward a more "normal" $\Delta^{17}O$ value and is explainable by the incorporation of ^{17}O-normal ($\Delta^{17}O \approx 0‰$) oxygen from air at room temperature. This result supports our initial model of high temperature vacancy formation (reduction) followed by room-temperature vacancy infill (re-oxidation). The incorporated oxygen from air is at 3% to 19% of the resulting ceria structural oxygen. If it is assumed that the ceria was re-oxidized to the initial state (stoichiometric CeO_2) these results would indicate that at peak reduction the ceria formula could range from $CeO_{1.94}$ to $CeO_{1.62}$. Making up the ends of this range, set 5.1 demands a fraction of new oxygen incorporated to be 2.3% ±1.1% whereas set 6 demands a fraction of 18.8% ±1.0%. These two ranges are mutually exclusive, but are required to explain the individual sets. Despite the variability, these are significant fractions and cannot be discounted.

As observed, 3 to 19% of re-oxidized ceria oxygen is sourced from air, indicating high defect mobility in vacancy rich bulk ceria at room temperature. A recent study using high-resolution scanning tunneling microscopy (STM) on ceria's crystal surface (111), provides direct evidence for surface defect mobility, and therefore facile re-oxidation, at room temperature (Namai et al., 2003). However, that study suggests that a much higher temperature threshold (550K) may be required for diffusion and re-oxidation of bulk oxygen vacancies. Another STM study does not support direct surface vacancy diffusion at room temperature, citing that a minimal temperature of 400°C is required for vacancy diffusion even at the (111) crystal surface (Esch et al., 2005). STM experiments use high-purity ceria crystals and focus on the most stable

(111) surface. It is not clear if the micron-size and the uncharacterized impurities in the ceria powder could have contributed to the observed greater oxygen mobility in our experiments. However, the findings of the present study as well as other previous studies (Bevan and Kordis, 1964; Laachir et al., 1991; Namai et al., 2003; Perrichon et al., 1994; Staudt et al., 2010) do suggest that reoxidation of ceria is possible at room temperature and vacancy diffusion and oxygen mobility are fast in vacancy rich ceria for both the surface and bulk phases.

The ceria-CO_2 exchange method for the measurement of the triple oxygen isotope composition of CO_2 (Hofmann and Pack, 2010) utilizes a procedure similar to the one in the present study in order to avoid oxygen isotope exchange with air or CO_2 while the powders are cooling. Avoiding exchange during cooling is necessary to prevent air $\Delta^{17}O$ from overwriting the ceria $\Delta^{17}O$ value and to prevent less predictable non-isothermal exchange with CO_2 during cooling. Both of these scenarios have the potential to overwrite the oxygen isotope signature derived from the sample CO_2 of interest. However, the results presented here suggest that there could be a 3 to 19% air oxygen intake by the ceria powder once the reaction chamber is opened to air. Reduction of ceria during the CO_2 exchange step used in the original method as well as in this study cannot be ruled out. In the present study, this aspect was not investigated as the ceria powders after CO_2 exchange are exposed to air and accordingly assumed to be stoichiometric. The ceria-CO_2 procedure has been used in multiple studies including the original work for the determination of the slope of CeO_2-CO_2 oxygen isotope exchange (Hofmann and Pack, 2010), the measurement of $\Delta^{17}O$ for several sources of anthropogenic CO_2 (Horvath et al., 2012) and the determination of the slope of CO_2-H_2O oxygen isotope exchange (Hofmann et al., 2012). We cannot determine if a similar magnitude of oxygen incorporation to that observed within the present study is present in the ceria-CO_2 exchange procedure of Hofmann and Pack (2010)

because the degree of room-temperature incorporation of air oxygen by ceria has the potential to vary with the size, morphology , and purity of the ceria as well as experimental parameters. In order to verify the existence of and quantify the level of contamination for the ceria-CO_2 exchange procedure it will be necessary to repeat the experiments that have been presented here using ^{17}O-anomalous ceria or CO_2.

The apparent isotope fractionation factor associated with oxygen release during heating in vacuum, $\alpha_{reduction}$, can be calculated based on the fraction of oxygen released, $f_{released}$, and the $\Delta\delta^{18}O_{reduction}$. If it is assumed that $f_{released} = f_{incorporated}$, the $\alpha_{reduction}$ can be calculated for this process using equation 4. As stated above, the best estimate for the percentage of incorporated oxygen is between 3 and 19%, with a median value at 7.6%. For the lower and upper estimate, $\alpha_{reduction}$ = 0.951 ±0.025 and 0.989 ±0.006, respectively. These estimates widely differ and do not overlap. If the median value of 7.6% is used for calculating $f_{incorporated}$, then $\alpha_{reduction}$ = 0.981 (−0.01; +0.01). In addition, it is important to note that this $\alpha_{reduction}$ value is integrated over a range of temperatures during heating and should not be regarded as either the fractionation factor at the stationary high temperature (700°C) or at a lower temperature when oxygen begins to leave the ceria structure. Despite the large error range, it is apparent that the oxygen released from the ceria structure during heating is isotopically lighter than the initial ceria powder. The finding is consistent with the prediction of a kinetic isotope effect for the step of ceria reduction or oxygen release.

A similar calculation can be performed to determine the apparent fractionation factor for the re-oxidation at 22°C, $\alpha_{oxidation}$. If air O_2 ($\delta^{18}O$ at 23.5‰) is the oxygen source, $\Delta\delta^{18}O_{oxidation} = \delta^{18}O_{incorporated} - \delta^{18}O_{air\ O_2}$=−21.4‰ (−4.1‰; +7.7‰). The $\alpha_{oxidation}$ is then calculated to be at 0.979 (−0.004; +0.007).

Our proposed model predicts that the behavior of oxygen transport in and out of the ceria structure during the RTRO experiments will be effectively kinetic processes. This is consistent with the calculated fractionation factors for $\alpha_{reduction}$ and $\alpha_{oxidation}$ which are both are less than 1.000 as predicted for kinetic processes (Young et al., 2002). The stability of the ceria oxygen isotope composition during storage at room temperature suggests that once the ceria is oxidized the migration of oxygen out of and into the ceria structure is slow at 22°C.

The observed isotope effects in the two opposite processes, reduction and subsequent re-oxidation, largely reflect the kinetic isotope effects of the main rate limiting surface reaction steps. These fractionations must be caused by surface processes because the oxygen isotope composition of the entire bulk of the resulting ceria is analyzed. Knowing the isotope effect has the potential to allow for identification the rate-limiting step during a process, but for processes with multiple kinetic steps or reaction pathways it is necessary to have a prior knowledge of the intrinsic kinetic isotope effect for individual reaction steps. Up to now, we know little about the isotope effect on gas adsorption-desorption on solid oxide surfaces, O_2 or CO_2 dissociation-association on surfaces, surface oxygen species diffusion on the ceria surfaces, or oxygen bulk diffusion in ceria's structure, nor do we know extensively about the surface-, temperature- and pO_2-dependent rates of those individual steps, especially in lower temperature realms. In addition, the results from our combined mass-balance and triangulation approach have inherent errors. The use of an independent method such as thermogravimetric analysis to determine the fraction of oxygen released from the ceria structure may help to reduce error and allow for the determination of the specific λ values for both the reduction and re-oxidation steps.

Despite the shortfalls, we can speculate, on the basis of the measured apparent oxygen isotope fractionation factors, that the most likely rate-limiting step is O_2 dissociation and O-

species association on ceria surface in our RTRO experiments. The key supporting evidence is the large magnitudes of isotope effect (i.e. α is at 0.981 or 0.979) during both the reduction and re-oxidation steps. Adsorption or desorption of an O-bearing molecule onto or out of a solid surface has a much smaller degree of isotope fractionation (Abe, 2008). At higher temperature bulk oxygen diffusion is not the rate-limiting step in ceria-oxygen exchange (Trovarelli, 1996). However, the rate of oxygen diffusion in ceria versus the rate of O_2 dissociation on ceria surface at room temperature is not known and we cannot quantify their individual contribution to the overall isotope effect at this time. Nevertheless, the observed degree of isotope effect is consistent with the weakening and eventual rupture of the O-O bond. For example, the α for the O_2 reduction in bioinorganic reaction ranges from 1.005 to 1.050 (Roth, 2007), which in our terms corresponds to a range of 0.995 to 0.952. The intrinsic kinetic isotope effect for either molecular oxygen dissociation or oxygen species association in our experiment could be much larger than determined here. This is because transport or reservoir effects and back reaction fluxes, factors that tend to mask the intrinsic isotope effect (Elsner et al., 2005; Ruszczycky and Anderson, 2006), cannot be excluded in the multi-step processes in our RTRO experiments. We also expect that that variably doped ceria, which is widely used in industry, will show different activation energies for reduction and oxidation (Balducci et al., 1997) due to potential differences in surface intermediates and spectators in O_2 dissociation (Palmer et al., 2002; Wang et al., 2009). These differences may be examined by measuring kinetic isotope effects.

Ceria, a widely used solid electrolyte in solid-oxide fuel cells, readily loses its structural oxygen under reducing conditions (lower pO_2) and readily gains structural oxygen under oxidizing condition (higher pO_2), however the easy migration of oxygen in and out of a solid oxide is not restricted to ceria. Many transitional metal oxides display variable degrees of this

property. Examples include YSZ (yttria-stabilized ZrO_2) (Sasaki and Maier, 1999), TiO_2 (Van Orman and Crispin, 2010), PrO_2 (Inaba et al., 1981), In_2O_3 (Walsh et al., 2011), and many perovskite-type oxides (Sasaki and Maier, 1999). Our study, examining natural-abundance oxygen isotope variations during a simple set of ceria-gas interactions, exemplifies the promise of the isotope effect for illuminating reaction kinetics and mechanisms at a fundamental level.

7. CONCLUSION AND IMPLICATIONS

The results of this study indicate that micron-size ceria will be partially reduced at 700°C in vacuum pressures of ~10^{-4} mbar. The reduced ceria powder, after cooling to room temperature under vacuum, is re-oxidized by air after the vacuum is broken. The amount of oxygen incorporated during the re-oxidation step is estimated to be 3 to 19% of the resulting ceria structural oxygen. The experiments and data demonstrate that oxygen mobility within the ceria structure is high for vacancy-rich ceria at room temperature. Thus, efforts to use ceria as oxygen exchange medium for easy measurement of gas triple oxygen isotope composition need to be approached with caution due to ceria's susceptibility to re-oxidation at room temperature. The $\delta^{18}O$ of ceria increases by 1.5‰ ±0.8‰ as its structure loses oxygen during reduction. This is followed by the incorporation of oxygen from air with a $\delta^{18}O$ of 2.1‰ (−4.1‰; +7.7‰) during re-oxidation at 22°C. These isotope effects are equivalent to apparent kinetic fractionation factors of 0.978 and 0.979 for oxygen release from ceria heated to 700°C in vacuum and for oxygen incorporation from air at 22°C respectively. The large magnitudes of isotope effect point to oxygen dissociation and association at the ceria surface as the likely rate-limiting step in the ceria RTRO experiments.

Lastly, we shall comment on two stable isotope methods: one, which uses enriched tracers, and another, which measures the isotope effect as done in this study. When isotopes are used as an enriched tracer, the nearly identical chemical behaviors of the isotopes allow an isotope-substituted chemical to be tracked along a reaction pathway. The main analytical tools are Fourier Transform Infrared and Raman spectroscopy, electron paramagnetic resonance, nuclear magnetic resonance, and mass spectrometry; the latter is typically either a quadrupole mass spectrometer or Fourier transform ion cyclotron resonance mass spectrometer. When the focus of a study is the isotope effect, natural-abundance isotope ratios are measured using an isotope-ratio mass spectrometer that has a much higher precision of the measurement of isotope ratios than the mass spectrometer used for enriched tracer measurement. Though claimed to elucidate reaction pathways or mechanisms, the enriched tracer method mostly answers questions at a chemical level, e.g. whether or not a specific molecule is involved in a reaction path. In enriched tracer methods, the isotope effect is ignored. The isotope effect, however, reveals pathway and mechanical insights reaching the quantum level, e.g. probing the structure of the transition state, distinguishing the nature of electron transfer (Ashley et al., 2010; Purdy et al., 2006), identifying rate-limiting step, or quantifying the effect of proton tunneling (Wolfsburg et al., 2010)

APPENDICES

APPENDIX A: TABULATED OXYGEN ISOTOPE RESULTS FOR HEMATITE PRECIPITATION

Table S-1: Results from both previous $\delta^{18}O$ (converted to logarithmic definition) measurements from Bao and Koch (1999) and new $\delta'^{18}O$ and $\Delta^{17}O$ analysis from this study. $\delta^{17}O$ values for the water are calculated using the $\delta^{18}O$ values for the water measured by Bao and Koch (1999) and published $\Delta^{17}O$ values for Baltimore tap water (Li et al., 2015). Values of α are for hematite precipitation with oxygen sourced from water ($\alpha_{hematite\text{-}water}$). The method for determining uncertainties is described in the text of the Appendix C for Chapter 1.

Sample Name	T in K	Previous $\delta'^{18}O$ (‰) SMOW	$\delta'^{18}O$ (‰) VSMOW	$\delta'^{17}O$ (‰) VSMOW	$\Delta'^{17}O$ (‰) VSMOW	$1000\ln(\alpha^{18})$	$1000\ln(\alpha^{17})$	θ	$\Delta\Delta'^{17}O$ (‰) VSMOW
CH-20A	303.15	-6.9239	-6.1482	-3.369	-0.1074	1.8828±0.1067	0.8513±0.0653	0.4525 (+0.0197;-0.0207)	-0.1475±0.0398
CH-20B	303.15	-6.9239	-6.3531	-3.4352	-0.0649	1.6778±0.1067	0.785±0.0653	0.4680(+0.0226;-0.0226)	-0.105±0.0398
CH-19A	310.15	-7.7298	-6.8148	-3.6828	-0.0675	1.2161±0.1067	0.5375±0.0653	0.4428 (+0.0302;-0.033)	-0.1077±0.0398
CG-13A	323.15	-7.8305	-7.1179	-3.8504	-0.0743	0.913±0.1067	0.3699±0.0653	0.4067 (+0.0409;-0.0462)	-0.1145±0.0398
CG-13B	323.15	-7.8305	-6.9974	-3.7403	-0.0282	1.0335±0.1067	0.4799±0.0653	0.465 (+0.0361;-0.038)	-0.0683±0.0398
CG-12B	343.15	-8.5363	-8.6214	-4.5597	0.0139	-0.5904±0.1067	-0.3394±0.0653	0.5761 (+0.0689;-0.065)	-0.0262±0.0398
CH-15A	368.15	-9.9493	-9.8669	-5.2947	-0.0603	-1.8359±0.1067	-1.0744±0.0653	0.5859 (+0.0212;-0.0225)	-0.1004±0.0398
CH-17A	388.15	-10.2524	-10.0992	-5.5437	-0.1861	-2.0682±0.1067	-1.3234±0.0653	0.6404 (+0.0200;-0.0207)	-0.2262±0.0398
CH-16A	413.15	-10.5555	-10.9575	-5.8772	-0.0643	-2.9265±0.1067	-1.657±0.0653	0.5664 (+0.0131;-0.0136)	-0.1044±0.0398

APPENDIX B: EXPERIMENTAL METHODS

The iron oxide materials used for this study were originaly precipitated for a study by Bao and Koch (1999). The iron oxides were stored as dry powders for nearly a decade and a half in centrifuge tubes since their original precipitation and processing. All procesing of the samples apart from the new triple oxygen isotope analysis were conducted for the original study (Bao and Koch, 1999). From the available samples, 9 synthetic hematite samples were selected based on the process used. All selected samples were precipitated from NaOH + HCO_3^- solutions (OH / Fe ≈ 3, HCO_3^- / Fe ≈ 0.7) at various temperatures for times ranging from 24 hours to 190 days depending on reaction temperature. Samples using this precipitation procedure were chosen because this procedure consistently generated hematite (as opposed to goethite and akaganeite) over the entire temperature range. The samples were then washed in a HCl solution to eliminate amorphous phases and then dried. XRD results for the selected samples show that the samples were pure hematite with the exception of sample CH-19A which may contain trace Goethite (Bao and Koch, 1999).

In the 1999 study, hematite samples were converted to O_2 by CO_2-laser fluorination and analyzed for $\delta^{18}O$ on a Thermo Finnigan MAT 252 isotope ratio mass spectrometer at the Geophysical Laboratory, Carnegie Institute, Washington. The O_2 yields were at or near 100 % for these samples with a precision of ± 0.05‰ and duplicate analyses being within 0.3‰ for $\delta^{18}O$ (Bao and Koch, 1999). Water with a known $\delta^{18}O$ composition (-8.0 ‰ ±0.1‰) was used for all synthesis solutions. The water that was used is doubly deionized New Jersey tap water. The $\delta^{18}O$ of the water was determined by CO_2 equilibration on a Micromass Isoprep 18 automated water analysis system interfaced with an Optima isotope ratio mass spectrometer at

the Department of Geosciences, Princeton University (Bao and Koch, 1999). Further details, descriptions and notes on the above procedures can be found in Bao and Koch (1999).

New analysis of the hematite samples from Bao and Koch (1999) was conducted at Louisiana State University. Hematite samples were analyzed for triple oxygen isotope composition as O_2 on a Thermo Finnigan MAT 253 isotope ratio mass spectrometer. Precision of O_2 isotope analysis is on the order of 0.03‰ or better for both the $\delta'^{18}O$ and $\Delta'^{17}O$. Prior to conversion to O_2, hematite samples were placed in a 20 torr BrF_5 atmosphere overnight to eliminate adsorbed water. Hematite samples were converted to O_2 by laser fluorination in a ~20 torr BrF_5 atmosphere. The resulting O_2 gas was purified using a series of LN_2 cooled U-traps before being collected into 5A mollecular sieve for transfer to the mass spectrometer. The triple oxygen isotope composition of the O_2 derived from each hematite sample is initialy measured in dual inlet mode relative to a house standard, LSU-O_2 ($\delta^{18}O$ = 17.543‰; $\delta^{17}O$ = 8.84‰). The house standard was initially calibrated to VSMOW using O_2 gas derived from BrF_5 laser fluorination of a dozen of UWG-2 samples using the same procedure described above. The $\delta^{18}O$ (5.800‰) for UWG-2 is taken from Valley et al. (1995) and an assigned $\delta^{17}O$ value of 3.016‰. These values give UWG-2, according to our lab reference scale, a $\Delta'^{17}O$ (C=0.5305) of -0.057‰ which is between the reported values of -0.019‰ and -0.113‰ from Young et al. (2016)and Pack and Herwartz (2014) respectively.

APPENDIX C: CALCULATION OF PARAMETERS FOR HEMATITE WATER FRACTIONATION

Values for θ, $\Delta\delta'^{18}O$ (=1000‰ ln α^{18}), $\Delta\delta'^{17}O$ and $\Delta\Delta'^{17}O$ are calculated using the equations;

$$\delta'^{17}O_{water} = 0.528 * \delta'^{18}O_{water} + \Delta'^{17}O_{water\ (C=0.528)} \quad \text{(C.1)}$$

$$\Delta'^{17}O_{water\ (C=0.5305)} = \delta'^{17}O_{water} - 0.5305 * \delta'^{18}O_{water} \quad \text{(C.2)}$$

$$\delta'^{17}O_{hematite} = 0.5305 * \delta'^{18}O_{hematite} + \Delta'^{17}O_{hematite\ (C=0.5305)} \quad \text{(C.3)}$$

$$\Delta\delta'^{17}O_{hematite-water} = \delta'^{17}O_{hematite} - \delta'^{17}O_{water} \quad \text{(C.4)}$$

$$\Delta\delta'^{18}O_{hematite-water} = \delta'^{18}O_{hematite} - \delta'^{18}O_{water} \quad \text{(C.5)}$$

$$\theta_{hematite-water} = \frac{\Delta\delta'^{17}O_{hematite-water}}{\Delta\delta'^{18}O_{hematite-water}} \quad \text{(C.6)}$$

and;

$$\Delta\Delta'^{17}O_{hematite-water} = \Delta'^{17}O_{hematite\ (C=0.5305)} - \Delta'^{17}O_{water\ (C=0.5305)} \quad \text{(C.7)}$$

Uncertainties for each fractionation parameter are calculated using a Monte Carlo method. The method uses the above equations, inputs for each known parameter and their respective 1σ uncertainties. These input uncertainties include those for the new hematite $\delta'^{18}O$ and $\Delta'^{17}O$ measurements (±0.03‰), the uncertainty of the original water $\delta^{18}O$ measurement (±0.1‰) and an assumed uncertainty of the $\Delta^{17}O$ of the water used for precipitation (±0.02‰; C=0.528). The uncertainty for the $\Delta^{17}O$ of the water was chosen so that nearly all reported values for the $\Delta^{17}O$ for tap waters in the continental United States lie within 1σ of the central value (Li *et al.*, 2015). A distribution of 1000 values are generated for each parameter with the same statistics as the respective parameter. These values are then processed through equations 1 through 7 and the mean and standard deviation are calculated for the results. The distributions for $\Delta\delta^{17}O$, $\Delta\delta^{18}O$ and $\Delta\Delta^{17}O$ are found to be normal in all cases, but the distributions of θ are slightly skewed. For

θ, the central value is the median and the uncertainties correspond to the 84.1% and 15.9% quantiles giving the boundaries of the central 68.2% of the distribution. The median is chosen, as opposed to the mean for θ, because it gives the same result as the solution using only the central values of the inputs.

APPENDIX D: COMPUTATIONAL METHODS

We utilize a Monte Carlo approach to provide a visual representation of the results of this study (Figures 1 and 2). The Monte Carlo models use the diatomic special case for ease of calculation because the vibrational frequency can be simply described as a function of the bond force constant and reduced mass. The model uses 1,000,000 evenly distributed randomly generated values for the secondary mass (0-300 AMU), the bond force constant (0-k_{UL}), and temperature (200-1600 K). The bond force constant for carbon monoxide (CO) is used as an arbitrary upper limit (UL) for the bond force constant for diatomic oxygen species. All calculations were performed in R (R Core Team, 2012).

APPENDIX E: $\delta^{18}O$ vs. TEMPERATURE PLOTS FOR COMPARISON WITH PREVIOUS LITERATURE

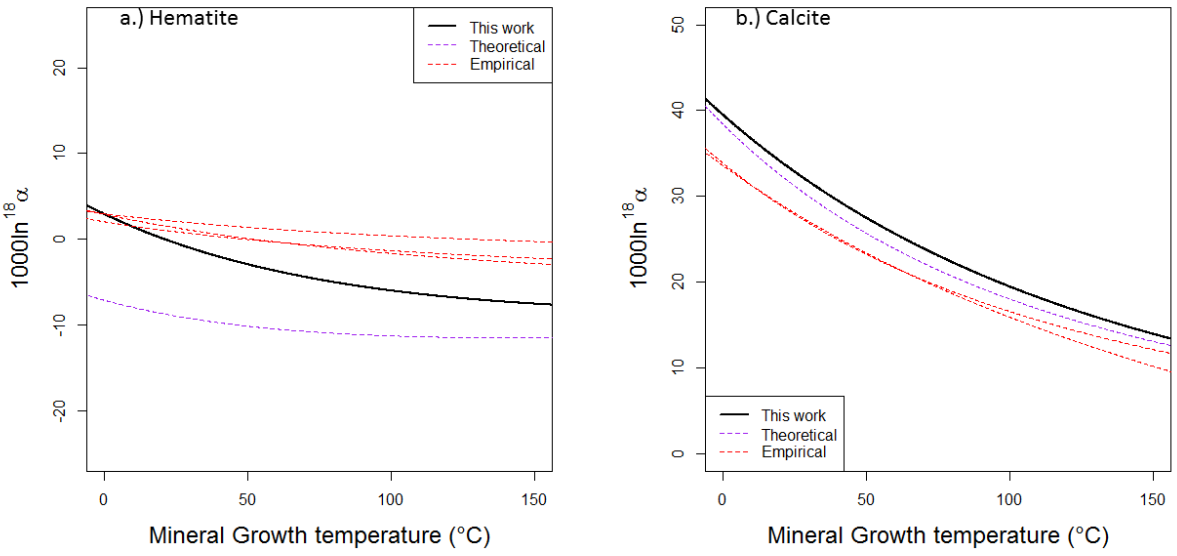

Figure 8. a. Theoretical results for 1000ln($^{18}\alpha$) temperature dependence for hematite-$H_2O_{(L)}$ equilibrium (Black solid line) with empirical curves (red dotted lines) from Bao and Koch (1999) (two lower curves) and Clayton and Epstein (1961) (upper curve) as well a theoretical curve (purple dotted line) from Zheng and Simon (1991). b. Theoretical results for 1000ln($^{18}\alpha$) temperature dependence for calcite-$H_2O_{(L)}$ equilibrium (Black solid line) with empirical curves (red dotted lines) from O'Neil et al. (1969) and Kim and O'Neil (1997)as well a theoretical curve (purple dotted line) from Zheng (1999).

APPENDIX F: STABLE ISOTOPE NOTATIONS

Two notations are commonly used to describe oxygen isotope ratios, the classical delta ($\delta^{xx}O$) notation and logarithmic "prime" ($\delta'^{xx}O$) delta notation. The standard notation is defined as:

$$\delta^{xx}O = \left(\frac{R^{xx}_{Sample}}{R^{xx}_{VSMOW}} - 1\right) \quad \text{(F.1)}$$

where:

$$R^{xx} = \frac{^{xx}O}{^{16}O} \quad \text{(F.2)}$$

R^{xx} is equal to the count of the oxygen isotope in question (^{18}O or ^{17}O) divided by the count of ^{16}O in a sample and R^{xx}_{VSMOW} is the corresponding ratio for the isotope standard VSMOW (Vienna Standard Mean Ocean Water). The classical delta notation is commonly used by researchers for the description of oxygen isotopes when only one oxygen isotope ratio is being examined. The classical notation has the advantage of allowing for a simple equation for mixing (Equation A.3).

$$\delta^{xx}O_{Total} = f * \delta^{xx}O_A + (1 - f) * \delta^{xx}O_B \quad \text{(F.3)}$$

where A and B are two oxygen bodies that are being mixed, $\delta^{xx}O_A$ is the oxygen isotope composition of body A and *f* is the mole fraction of oxygen incorporated from A into the total. This equation can easily be shown to closely approximate a more accurate mixing equation based on the percentage of each isotope as long as the percent of ^{16}O for oxygen bodies A and B are close to one another. Variations in the percent of ^{16}O are within 0.02% for isotope-labeled samples used in our experiments, thus these meet the criteria for use of this mixing equation.

The "delta prime" (δ') notation is defined as follows (Equation A.4):

$$\delta'^{xx}O = \ln\left(\frac{R^{xx}_{Sample}}{R^{xx}_{VSMOW}}\right) \quad \text{(F.4)}$$

Isotopic fractionation is defined as a preferential enrichment of an isotope over another during a chemical or physical process. This has also been referred to as the isotope effect. There are equilibrium and kinetic isotope effects. The fractionation factor α is defined as:

$$\alpha^{xx}_{a-b} = \frac{R^{xx}_a}{R^{xx}_b} \quad \text{(F.5)}$$

For any well-defined process,

$$\alpha^{17} = (\alpha^{18})^{\lambda} \quad \text{(F.6)}$$

Because almost all known thermally driven chemical and physical processes show mass dependent fractionation and the λ does not vary much for different processes beyond the value of 0.515 ±0.010, the $\Delta\delta'^{17}O/\Delta\delta'^{18}O$ ratio is nearly constant within limited range of isotope ratios. This relationship also results in most terrestrial oxygen-bearing compounds falling on the Terrestrial Fractionation Line (TFL), a line with a slope of roughly 0.515 in a $\delta'^{17}O$-$\delta'^{18}O$ space. For those that do not sit on the TFL, we measure the deviation from the TFL using "Cap Delta" notation defined as:

$$\Delta^{17}O = \delta'^{17}O - \lambda * \delta'^{18}O \quad \text{(F.7)}$$

Therefore, for a mass dependent process, the $\Delta^{17}O$ of the product will be very close to that of the reactants.

It is important to note that when isotope ratios for all components involved are very close to both each other and the VSMOW, the "classical" and "prime" delta notations are indistinguishable in values. For this reason, the classical delta notation, $\delta^{xx}O$, is used in the main text as well as in Appendix G through K.

APPENDIX G: CALCULATING $f_{incorporated}$

The mole fraction of oxygen that is incorporated into the ceria structure during the Room Temperature Reoxidation experiments (RTRO) can be described by the mixing equations:

$$\delta^{18}O_{Final} = f * \delta^{18}O_{incoporated} + (1-f) * \delta^{18}O_{reduced} \quad \text{(G.1)}$$

and;

$$\delta^{17}O_{Final} = f * \delta^{17}O_{incorporated} + (1-f) * \delta^{17}O_{reduced} \quad \text{(G.2)}$$

where f is the fraction of the final ceria structural oxygen that was derived from air during the re-oxidation process.

Combining equation Equations B.1 and B.2 using equation A.7 yields:

$$\Delta^{17}O_{Final} = f * \Delta^{17}O_{incorporated} + (1-f) * \Delta^{17}O_{reduced} \quad \text{(G.3)}$$

Because the reduction process is mass dependent, the $\Delta^{17}O$ of reduced ceria at 700°C is equal to that of the initial ceria. We also know that the $\Delta^{17}O_{incorporated}$ is approximately equal to that of air oxygen.

Therefore,

$$f_{incorporated} = \frac{\Delta^{17}O_{Final} - \Delta^{17}O_{Initial}}{\Delta^{17}O_{air} - \Delta^{17}O_{Initial}} \quad \text{(G.4)}$$

It is unknown which component or components of air are responsible for the re-oxidation. Of these components, only the oxygen isotope composition of air O_2 significantly deviates from the TFL ($\Delta^{17}O$=–0.23‰ when λ=.52) (Bao et al., 2008). The calculations as presented in the main text include the assumption that air O_2 is the sole oxidizer. Best estimates of the fraction of oxygen incorporated and their respective errors were determined using a Monte Carlo approach. Results of these calculations can be found in Appendix K.

APPENDIX H: CALCULATING $\Delta\delta^{18}O_{reduction}$ AND $\delta^{18}O_{incorporated}$

In each RTRO experiment, we expect a shift of the $\delta^{18}O$ value for the remaining ceria powder from the initial one after being heated at 700°C for an hour. This shift is described by the term $\Delta\delta^{18}O_{reduction}$. Here the corresponding shift in the $\delta^{17}O$ follows a mass-dependent trend, thus the $\Delta^{17}O$ of the reduced ceria is equal to that of the initial, which is purposely set to be deviated from the TFL. During re-oxidation, the oxygen taken into the ceria structure during room-temperature re-oxidation is sourced from air. This incorporated oxygen has a $\delta^{18}O$ value represented by $\delta^{18}O_{incorporated}$, and a $\Delta^{17}O$ value that is equal to $\Delta^{17}O_{air}$.

Because the isotope ratio variability is small and the ratios are close to that of VSMOW in all our RTRO experiments, the mixing trend will be linear in $\delta^{17}O$-$\delta^{18}O$ space. This line will contain the points representing the oxygen isotope compositions of the reduced state, the final ceria, and the incorporated oxygen. This can be stated as the geometric relationship:

$$\frac{\delta^{17}O_{Final}-\delta^{17}O_{incorporated}}{\delta^{18}O_{Final}-\delta^{18}O_{incorporated}}=\frac{\delta^{17}O_{reduced}-\delta^{17}O_{Final}}{\delta^{18}O_{reduced}-\delta^{18}O_{Final}} \quad \text{(H.1)}$$

or:

$$\frac{\delta^{17}O_{Final}-(\lambda_{incorporation}*\delta^{18}O_{incorporated}+\Delta^{17}O_{air\,O_2})}{\delta^{18}O_{Final}-\delta^{18}O_{incorporated}}=$$

$$\frac{(\lambda_{reduction}*\Delta\delta^{18}O_{reduction}+\delta^{17}O_{Initial})-\delta^{17}O_{Final}}{(\Delta\delta^{18}O_{reduction}+\delta^{18}O_{Initial})-\delta^{18}O_{Final}} \quad \text{(H.2)}$$

As with the calculation of the fraction of oxygen incorporated, air O_2 is assumed to be the sole oxidizer. The $\delta^{18}O$ and $\delta^{17}O$ values for the initial and final powders are measured.

Equation C.2 has two unknowns. Solving for these unknowns requires a second independent equation. This second equation is identical in form to the first equation (Equation C.2), but has inputs determined from another comparable experiment set.

The $\Delta\delta^{18}O_{reduction}$ may be itself a function of the fraction of oxygen that remains in the ceria structure once it has reached maximum reduction, and thus it is tied to the $f_{Incorporated}$, which we know is often not the same for the two sets. Similarly, $\delta^{18}O_{incorporated}$ may also be different between two independent experimental sets. Therefore, a fundamental assumption of our mass-balance and triangulation approach is that the multiple experimental sets conducted in the same experimental conditions have experienced the same degrees of isotope effect. The variability seen among the different sets is due to random errors occurring during the RTRO experiments that are sensitive to many factors, such as minor variations in temperature ramp, trace contamination, powder size, powder surface area, and perhaps pile shape. In consideration of the observed variability, the most representative values of $\Delta\delta^{18}O_{reduction}$ and $\delta^{18}O_{incorporated}$ for our specific experimental conditions are chosen to be the medians of the complete Monte Carlo results (see Appendix H).

APPENDIX I: DIAGRAM OF EXPERIMENTAL APPARATUS

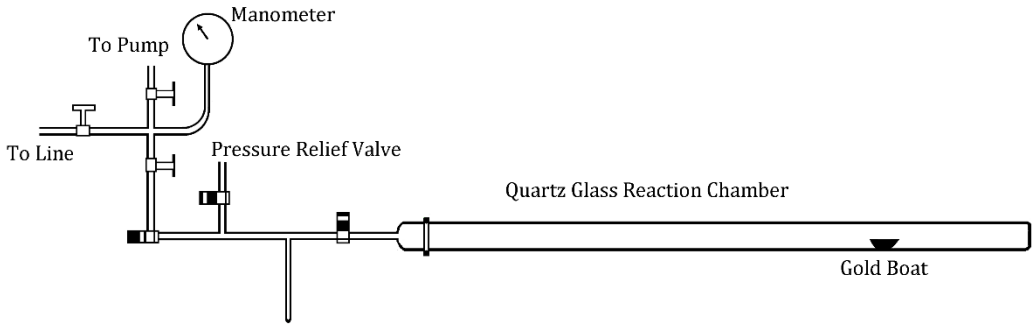

Figure D.1: Diagram of the stainless-steel vacuum line and quartz-glass reaction chamber used in the RTRO experiments.

APPENDIX J: TABULATED RESULTS FOR THE FRACTION OF OXYGEN INCORPORATED DURING RE-OXIDATION

		Middle 68.2% Error		Middle 80% Error	
Experiment Set	**median**	**-**	**+**	**-**	**+**
Set 1	11.23%	1.92%	1.83%	2.42%	2.35%
Set 2-1	29.40%	112.08%	108.23%	197.65%	182.26%
Set 2-2	22.05%	144.13%	145.34%	252.31%	242.84%
Set 3-1	-0.08%	28.77%	21.11%	41.40%	26.55%
Set 3-2	-11.24%	33.11%	21.75%	47.75%	26.80%
Set 4-1	3.73%	8.11%	7.59%	10.50%	9.45%
Set 4-2	1.22%	8.32%	7.63%	10.81%	9.54%
Set 5-1	2.33%	1.15%	1.16%	1.48%	1.46%
Set 5-2	7.82%	1.12%	1.13%	1.44%	1.42%
Set 6	18.81%	1.06%	1.06%	1.34%	1.34%
Set 7	1.79%	8.63%	7.85%	11.30%	9.94%
Set 8	1.71%	1.96%	1.91%	2.48%	2.42%
Set 9	17.39%	1.84%	1.78%	2.34%	2.24%
Set 10	14.49%	1.74%	1.67%	2.20%	2.15%

APPENDIX K: TABULATED RESULTS FOR $\delta^{18}O_{incorporated}$ AND $\Delta\delta^{18}O_{reduction}$

$\delta^{18}O$ Incorporated		Middle 68.2% Error		Middle 80% Error	
Experimental set	Median	-	+	-	+
1-2.1	1.8‰	1.1‰	0.7‰	1.5‰	1.1‰
1-2.2	1.3‰	0.5‰	0.9‰	0.7‰	1.2‰
1-3.1	-2.1‰	0.8‰	1.2‰	1.3‰	1.8‰
1-3.2	-1.5‰	0.8‰	1.4‰	1.1‰	2.3‰
1-4.1	1.7‰	3.3‰	9.2‰	4.4‰	15.8‰
1-4.2	1.9‰	2.8‰	6.9‰	3.4‰	11.3‰
1-5.1	6.6‰	4.4‰	3.7‰	5.9‰	4.6‰
1-5.2	4.5‰	13.4‰	8.4‰	18.9‰	10.3‰
1-6	10.8‰	3.9‰	3.2‰	5.2‰	4.0‰
1-7	11.2‰	1.9‰	1.1‰	3.2‰	2.3‰
2.1-3.1	2.1‰	0.4‰	0.2‰	0.5‰	0.3‰
2.1-3.2	2.1‰	0.2‰	0.2‰	0.2‰	0.4‰
2.1-4.1	1.8‰	0.8‰	0.7‰	1.2‰	1.2‰
2.1-4.2	1.8‰	0.7‰	0.6‰	1.2‰	1.2‰
2.1-5.1	1.6‰	1.1‰	1.1‰	1.9‰	1.9‰
2.1-5.2	1.7‰	0.7‰	0.7‰	1.3‰	1.2‰
2.1-6	2.2‰	0.1‰	0.3‰	0.2‰	0.4‰
2.1-7	1.4‰	2.2‰	1.3‰	3.4‰	2.5‰
2.2-3.1	1.9‰	0.3‰	0.3‰	0.3‰	0.4‰
2.2-3.2	2.1‰	0.2‰	0.2‰	0.3‰	0.3‰
2.2-4.1	1.6‰	0.9‰	0.9‰	1.6‰	1.7‰
2.2-4.2	1.7‰	0.9‰	0.9‰	1.6‰	1.7‰
2.2-5.1	1.3‰	1.3‰	1.3‰	2.2‰	2.4‰
2.2-5.2	1.6‰	1.0‰	0.8‰	1.6‰	1.5‰
2.2-6	2.3‰	0.1‰	0.1‰	0.2‰	0.2‰
2.2-7	0.5‰	1.5‰	1.9‰	2.3‰	2.7‰
3.1-4.1	0.6‰	3.7‰	4.9‰	6.5‰	7.4‰
3.1-4.2	0.9‰	3.7‰	4.5‰	6.4‰	6.9‰
3.1-5.1	-0.9‰	8.0‰	10.9‰	14.3‰	16.2‰
3.1-5.2	-0.1‰	3.9‰	6.2‰	6.8‰	9.2‰
3.1-6	3.1‰	3.1‰	2.3‰	5.0‰	4.1‰
3.1-7	-10.2‰	17.9‰	25.8‰	31.4‰	37.0‰
3.2-4.1	-0.2‰	4.4‰	6.8‰	8.2‰	10.6‰
3.2-4.2	-0.1‰	4.4‰	7.0‰	7.9‰	10.5‰
3.2-5.1	-2.5‰	8.0‰	12.6‰	15.1‰	19.8‰
3.2-5.2	-0.9‰	4.7‰	6.0‰	8.2‰	10.1‰
3.2-6	2.5‰	0.3‰	0.7‰	0.4‰	1.2‰
3.2-7	-10.1‰	7.1‰	10.6‰	12.8‰	18.4‰
4.1-5.1	6.9‰	10.2‰	7.3‰	15.7‰	13.4‰
4.1-5.2	4.0‰	3.1‰	4.1‰	5.5‰	6.4‰
4.1-6	7.1‰	0.7‰	1.8‰	0.9‰	3.1‰
4.1-7	46.4‰	19.7‰	18.2‰	26.4‰	27.1‰
4.2-5.1	2.3‰	10.3‰	14.3‰	18.2‰	21.3‰
4.2-5.2	2.9‰	4.8‰	6.3‰	8.5‰	10.1‰
4.2-6	6.3‰	0.4‰	0.9‰	0.6‰	1.4‰
4.2-7	-95.3‰	170.2‰	96.0‰	286.0‰	281.1‰
5.1-6	8.7‰	0.9‰	0.7‰	1.2‰	0.9‰
5.1-7	9.6‰	16.1‰	12.1‰	24.7‰	21.1‰
5.2-6	9.0‰	1.4‰	1.0‰	1.8‰	1.2‰
5.2-7	11.7‰	11.3‰	8.7‰	19.8‰	15.8‰
6-7	10.7‰	1.1‰	2.3‰	1.3‰	3.4‰
Grand	2.1‰	4.1‰	7.7‰	7.8‰	10.1‰

$\Delta\delta^{18}O$ Reduction		Middle 68.2% Error		Middle 80% Error	
Experimental set	Median	-	+	-	+
set 1-2.1	1.7‰	0.7‰	0.5‰	0.9‰	0.7‰
set 1-2.2	1.7‰	0.6‰	0.7‰	0.7‰	0.8‰
set 1-3.1	2.0‰	0.6‰	0.9‰	0.8‰	1.2‰
set 1-3.2	2.0‰	0.6‰	0.4‰	0.8‰	1.3‰
set 1-4.1	1.4‰	0.7‰	0.2‰	1.5‰	0.3‰
set 1-4.2	1.4‰	0.6‰	0.2‰	1.0‰	0.2‰
set 1-5.1	1.0‰	0.1‰	0.1‰	0.1‰	0.1‰
set 1-5.2	1.3‰	0.7‰	0.8‰	0.9‰	1.1‰
Set 1-6	0.5‰	0.7‰	1.0‰	0.9‰	1.3‰
Set 1-7	0.6‰	0.7‰	0.3‰	1.0‰	0.4‰
Set 2.1-3.1	2.1‰	0.3‰	0.3‰	0.4‰	0.3‰
Set 2.1-3.2	2.4‰	0.2‰	0.3‰	0.3‰	0.4‰
set 2.1-4.1	1.5‰	0.2‰	0.2‰	0.2‰	0.3‰
set 2.1-4.2	1.6‰	0.2‰	0.2‰	0.2‰	0.2‰
set 2.1-5.1	1.2‰	0.2‰	0.2‰	0.2‰	0.2‰
set 2.1-5.2	1.5‰	0.2‰	0.2‰	0.3‰	0.2‰
Set 2.1-6	2.5‰	0.2‰	0.2‰	0.2‰	0.3‰
Set 2.1-7	0.7‰	0.6‰	0.6‰	0.7‰	0.7‰
Set 2.2-3.1	2.1‰	0.2‰	0.3‰	0.3‰	0.4‰
Set 2.2-3.2	2.1‰	0.2‰	0.2‰	0.3‰	0.3‰
set 2.2-4.1	1.6‰	0.2‰	0.2‰	0.2‰	0.2‰
set 2.2-4.2	1.7‰	0.9‰	0.9‰	1.6‰	1.7‰
set 2.2-5.1	1.2‰	0.2‰	0.1‰	0.3‰	0.2‰
set 2.2-5.2	1.6‰	0.4‰	0.1‰	0.4‰	0.2‰
Set 2.2-6	2.5‰	0.2‰	0.2‰	0.3‰	0.2‰
Set 2.2-7	0.7‰	0.6‰	0.6‰	0.8‰	0.8‰
set 3.1-4.1	1.9‰	0.5‰	0.1‰	0.5‰	0.2‰
set 3.1-4.2	1.8‰	0.3‰	0.2‰	0.3‰	0.2‰
set 3.1-5.1	1.4‰	0.6‰	0.1‰	0.6‰	0.2‰
set 3.1-5.2	1.9‰	0.8‰	0.2‰	1.0‰	0.3‰
Set 3.1-6	2.4‰	0.6‰	0.4‰	1.1‰	0.8‰
Set 3.1-7	0.1‰	1.2‰	1.2‰	1.7‰	1.7‰
set 3.2-4.1	1.8‰	0.2‰	0.2‰	0.3‰	0.2‰
set 3.2-4.2	1.8‰	0.2‰	0.2‰	0.3‰	0.3‰
set 3.2-5.1	1.4‰	0.5‰	0.1‰	0.6‰	0.2‰
set 3.2-5.2	1.9‰	0.9‰	0.2‰	1.1‰	0.4‰
Set 3.2-6	2.5‰	0.3‰	0.2‰	0.4‰	0.3‰
Set 3.2-7	0.5‰	1.4‰	1.7‰	1.8‰	2.5‰
set 4.1-5.1	1.0‰	0.2‰	0.4‰	0.3‰	0.5‰
set 4.1-5.2	1.5‰	0.6‰	0.1‰	0.8‰	0.3‰
Set 4.1-6	1.4‰	0.5‰	0.3‰	0.8‰	0.3‰
Set 4.1-7	0.2‰	1.9‰	3.8‰	2.7‰	5.3‰
set 4.2-5.1	1.3‰	0.6‰	0.1‰	0.7‰	0.3‰
set 4.2-5.2	1.6‰	0.8‰	0.2‰	1.0‰	0.5‰
Set 4.2-6	1.6‰	0.3‰	0.2‰	0.4‰	0.2‰
Set 4.2-7	3.5‰	12.3‰	7.5‰	19.7‰	15.4‰
Set 5.1-6	1.0‰	0.1‰	0.1‰	0.1‰	0.1‰
Set 5.1-7	0.9‰	0.2‰	0.6‰	0.4‰	0.8‰
Set 5.2-6	0.9‰	0.1‰	0.2‰	0.2‰	0.3‰
Set 5.2-7	0.7‰	0.8‰	1.3‰	1.4‰	2.1‰
Set 6-7	0.5‰	0.5‰	0.2‰	0.8‰	0.2‰
Grand	1.5‰	0.8‰	0.8‰	1.1‰	1.0‰

APPENDIX L: PERMISSIONS

License Number	3917241179136
License date	Jul 27, 2016
Licensed Content Publisher	Elsevier
Licensed Content Publication	Geochimica et Cosmochimica Acta
Licensed Content Title	The reduction and oxidation of ceria: A natural abundance triple oxygen isotope perspective; DOI:10.1016/j.gca.2015.03.030
Licensed Content Author	Justin Hayles, Huiming Bao
Licensed Content Date	15 June 2015
Licensed Content Volume Number	159
Licensed Content Issue Number	n/a
Licensed Content Pages	11
Start Page	220
End Page	230
Type of Use	reuse in a thesis/dissertation
Portion	full article
Format	electronic
Are you the author of this Elsevier article?	Yes
Will you be translating?	No
Order reference number	
Title of your thesis/dissertation	Theory and Utility of the Three Isotope Fractionation Relationship
Expected completion date	Aug 2016
Estimated size (number of pages)	104
Elsevier VAT number	GB 494 6272 12
Requestor Location	Justin A Hayles E235 Howe Russell BATON ROUGE, LA 70803 United States Attn: Justin A Hayles
Total	0.00 USD
Terms and Conditions	

INTRODUCTION

1. The publisher for this copyrighted material is Elsevier. By clicking "accept" in connection with completing this licensing transaction, you agree that the following terms and conditions apply to this transaction (along with the Billing and Payment terms and conditions established by Copyright Clearance Center, Inc. ("CCC"), at the time that you opened your Rightslink account and that are available at any time at http://myaccount.copyright.com).

GENERAL TERMS

2. Elsevier hereby grants you permission to reproduce the aforementioned material subject to the terms and conditions indicated.

3. Acknowledgement: If any part of the material to be used (for example, figures) has appeared in our publication with credit or acknowledgement to another source, permission must also be sought from that source. If such permission is not obtained then that material may not be included in your publication/copies. Suitable acknowledgement to the source must be made, either as a footnote or in a reference list at the end of your publication, as follows:

"Reprinted from Publication title, Vol /edition number, Author(s), Title of article / title of chapter, Pages No., Copyright (Year), with permission from Elsevier [OR APPLICABLE SOCIETY COPYRIGHT OWNER]." Also Lancet special credit - "Reprinted from The Lancet, Vol. number, Author(s), Title of article, Pages No., Copyright (Year), with permission from Elsevier."

4. Reproduction of this material is confined to the purpose and/or media for which permission is hereby given.

5. Altering/Modifying Material: Not Permitted. However figures and illustrations may be altered/adapted minimally to serve your work. Any other abbreviations, additions, deletions and/or any other alterations shall be made only with prior written authorization of Elsevier Ltd. (Please contact Elsevier at permissions@elsevier.com)

6. If the permission fee for the requested use of our material is waived in this instance, please be advised that your future requests for Elsevier materials may attract a fee.

7. Reservation of Rights: Publisher reserves all rights not specifically granted in the combination of (i) the license details provided by you and accepted in the course of this licensing transaction, (ii) these terms and conditions and (iii) CCC's Billing and Payment terms and conditions.

8. License Contingent Upon Payment: While you may exercise the rights licensed immediately upon issuance of the license at the end of the licensing process for the transaction, provided that you have disclosed complete and accurate details of your proposed use, no license is finally effective unless and until full payment is received from you (either by publisher or by CCC) as provided in CCC's Billing and Payment terms and conditions. If full payment is not received on

a timely basis, then any license preliminarily granted shall be deemed automatically revoked and shall be void as if never granted. Further, in the event that you breach any of these terms and conditions or any of CCC's Billing and Payment terms and conditions, the license is automatically revoked and shall be void as if never granted. Use of materials as described in a revoked license, as well as any use of the materials beyond the scope of an unrevoked license, may constitute copyright infringement and publisher reserves the right to take any and all action to protect its copyright in the materials.

9. Warranties: Publisher makes no representations or warranties with respect to the licensed material.

10. Indemnity: You hereby indemnify and agree to hold harmless publisher and CCC, and their respective officers, directors, employees and agents, from and against any and all claims arising out of your use of the licensed material other than as specifically authorized pursuant to this license.

11. No Transfer of License: This license is personal to you and may not be sublicensed, assigned, or transferred by you to any other person without publisher's written permission.

12. No Amendment Except in Writing: This license may not be amended except in a writing signed by both parties (or, in the case of publisher, by CCC on publisher's behalf).

13. Objection to Contrary Terms: Publisher hereby objects to any terms contained in any purchase order, acknowledgment, check endorsement or other writing prepared by you, which terms are inconsistent with these terms and conditions or CCC's Billing and Payment terms and conditions. These terms and conditions, together with CCC's Billing and Payment terms and conditions (which are incorporated herein), comprise the entire agreement between you and publisher (and CCC) concerning this licensing transaction. In the event of any conflict between your obligations established by these terms and conditions and those established by CCC's Billing and Payment terms and conditions, these terms and conditions shall control.

14. Revocation: Elsevier or Copyright Clearance Center may deny the permissions described in this License at their sole discretion, for any reason or no reason, with a full refund payable to you. Notice of such denial will be made using the contact information provided by you. Failure to receive such notice will not alter or invalidate the denial. In no event will Elsevier or Copyright Clearance Center be responsible or liable for any costs, expenses or damage incurred by you as a result of a denial of your permission request, other than a refund of the amount(s) paid by you to Elsevier and/or Copyright Clearance Center for denied permissions.

LIMITED LICENSE

The following terms and conditions apply only to specific license types:

15. **Translation**: This permission is granted for non-exclusive world **English** rights only unless your license was granted for translation rights. If you licensed translation rights you may only

translate this content into the languages you requested. A professional translator must perform all translations and reproduce the content word for word preserving the integrity of the article.

16. **Posting licensed content on any Website**: The following terms and conditions apply as follows: Licensing material from an Elsevier journal: All content posted to the web site must maintain the copyright information line on the bottom of each image; A hyper-text must be included to the Homepage of the journal from which you are licensing at http://www.sciencedirect.com/science/journal/xxxxx or the Elsevier homepage for books at http://www.elsevier.com; Central Storage: This license does not include permission for a scanned version of the material to be stored in a central repository such as that provided by Heron/XanEdu.

Licensing material from an Elsevier book: A hyper-text link must be included to the Elsevier homepage at http://www.elsevier.com . All content posted to the web site must maintain the copyright information line on the bottom of each image.

Posting licensed content on Electronic reserve: In addition to the above the following clauses are applicable: The web site must be password-protected and made available only to bona fide students registered on a relevant course. This permission is granted for 1 year only. You may obtain a new license for future website posting.

17. **For journal authors:** the following clauses are applicable in addition to the above:

Preprints:

A preprint is an author's own write-up of research results and analysis, it has not been peer-reviewed, nor has it had any other value added to it by a publisher (such as formatting, copyright, technical enhancement etc.).

Authors can share their preprints anywhere at any time. Preprints should not be added to or enhanced in any way in order to appear more like, or to substitute for, the final versions of articles however authors can update their preprints on arXiv or RePEc with their Accepted Author Manuscript (see below).

If accepted for publication, we encourage authors to link from the preprint to their formal publication via its DOI. Millions of researchers have access to the formal publications on ScienceDirect, and so links will help users to find, access, cite and use the best available version. Please note that Cell Press, The Lancet and some society-owned have different preprint policies. Information on these policies is available on the journal homepage.

Accepted Author Manuscripts: An accepted author manuscript is the manuscript of an article that has been accepted for publication and which typically includes author-incorporated changes suggested during submission, peer review and editor-author communications.

Authors can share their accepted author manuscript:

- – immediately
    - via their non-commercial person homepage or blog
    - by updating a preprint in arXiv or RePEc with the accepted manuscript
    - via their research institute or institutional repository for internal institutional uses or as part of an invitation-only research collaboration work-group
    - directly by providing copies to their students or to research collaborators for their personal use
    - for private scholarly sharing as part of an invitation-only work group on commercial sites with which Elsevier has an agreement
- – after the embargo period
    - via non-commercial hosting platforms such as their institutional repository
    - via commercial sites with which Elsevier has an agreement

In all cases accepted manuscripts should:

- – link to the formal publication via its DOI
- – bear a CC-BY-NC-ND license - this is easy to do
- – if aggregated with other manuscripts, for example in a repository or other site, be shared in alignment with our hosting policy not be added to or enhanced in any way to appear more like, or to substitute for, the published journal article.

Published journal article (JPA): A published journal article (PJA) is the definitive final record of published research that appears or will appear in the journal and embodies all value-adding publishing activities including peer review co-ordination, copy-editing, formatting, (if relevant) pagination and online enrichment.

Policies for sharing publishing journal articles differ for subscription and gold open access articles:

Subscription Articles: If you are an author, please share a link to your article rather than the full-text. Millions of researchers have access to the formal publications on ScienceDirect, and so links will help your users to find, access, cite, and use the best available version.

Theses and dissertations which contain embedded PJAs as part of the formal submission can be posted publicly by the awarding institution with DOI links back to the formal publications on ScienceDirect.

If you are affiliated with a library that subscribes to ScienceDirect you have additional private sharing rights for others' research accessed under that agreement. This includes use for classroom teaching and internal training at the institution (including use in course packs and courseware programs), and inclusion of the article for grant funding purposes.

Gold Open Access Articles: May be shared according to the author-selected end-user license and should contain a CrossMark logo, the end user license, and a DOI link to the formal publication on ScienceDirect.

Please refer to Elsevier's posting policy for further information.

18. **For book authors** the following clauses are applicable in addition to the above: Authors are permitted to place a brief summary of their work online only. You are not allowed to download and post the published electronic version of your chapter, nor may you scan the printed edition to create an electronic version. **Posting to a repository:** Authors are permitted to post a summary of their chapter only in their institution's repository.

19. **Thesis/Dissertation**: If your license is for use in a thesis/dissertation your thesis may be submitted to your institution in either print or electronic form. Should your thesis be published commercially, please reapply for permission. These requirements include permission for the Library and Archives of Canada to supply single copies, on demand, of the complete thesis and include permission for Proquest/UMI to supply single copies, on demand, of the complete thesis. Should your thesis be published commercially, please reapply for permission. Theses and dissertations which contain embedded PJAs as part of the formal submission can be posted publicly by the awarding institution with DOI links back to the formal publications on ScienceDirect.

Elsevier Open Access Terms and Conditions

You can publish open access with Elsevier in hundreds of open access journals or in nearly 2000 established subscription journals that support open access publishing. Permitted third party re-use of these open access articles is defined by the author's choice of Creative Commons user license. See our open access license policy for more information.

Terms & Conditions applicable to all Open Access articles published with Elsevier:

Any reuse of the article must not represent the author as endorsing the adaptation of the article nor should the article be modified in such a way as to damage the author's honour or reputation. If any changes have been made, such changes must be clearly indicated.

The author(s) must be appropriately credited and we ask that you include the end user license and a DOI link to the formal publication on ScienceDirect.

If any part of the material to be used (for example, figures) has appeared in our publication with credit or acknowledgement to another source it is the responsibility of the user to ensure their reuse complies with the terms and conditions determined by the rights holder.

Additional Terms & Conditions applicable to each Creative Commons user license:

REFERENCES

Abe, O. (2008) Isotope fractionation of molecular oxygen during adsorption/desorption by molecular sieve zeolite. Rapid Communications in Mass Spectrometry 22, 2510-2514.

Alper, J.S. and Gelb, R.I. (1990) Standard errors and confidence-intervals in nonlinear-regression - comparison of monte-carlo and parametric statistics. Journal of Physical Chemistry 94, 4747-4751.

Alper, J.S. and Gelb, R.I. (1991) Monte-Carlo method for the determination of confidence-intervals - analysis of non-normally distributed errors in sequential experiments. Journal of Physical Chemistry 95, 104-108.

Anan'ev, M.V., Kurumchin, E.K., Vdovin, G.K. and Bershitskaya, N.M. (2012) Kinetics of interaction of gas phase oxygen with cerium-gadolinium oxide. Russ. J. Electrochem. 48, 871-878.

Ashley, D.C., Brinkley, D.W. and Roth, J.P. (2010) Oxygen isotope effects as structural and mechanistic probes in inorganic oxidation chemistry. Inorganic Chemistry 49, 3661-3675.

Assonov, S.S. and Brenninkmeijer, C.A.M. (2001) A new method to determine the ^{17}O isotopic abundance in CO_2 using oxygen isotope exchange with a solid oxide. Rapid Communications in Mass Spectrometry 15, 2426-2437.

Balducci, G., Kaspar, J., Fornasiero, P., Graziani, M., Islam, M.S. and Gale, J.D. (1997) Computer simulation studies of bulk reduction and oxygen migration in CeO2-ZrO2 solid solutions. J. Phys. Chem. B 101, 1750-1753.

Bao, H., Cao, X. and Hayles, J.A. (2015) The confines of triple oxygen isotope exponents in elemental and complex mass-dependent processes. Geochimica Et Cosmochimica Acta 170, 39-50.

Bao, H.M., Cao, X.B. and Hayles, J. (2016) Triple Oxygen Isotopes: Fundamental Relationships and Applications. Annual Review of Earth and Planetary Sciences 44.

Bao, H.M. and Koch, P.L. (1999) Oxygen isotope fractionation in ferric oxide-water systems: Low temperature synthesis. Geochimica Et Cosmochimica Acta 63, 599-613.

Bao, H.M., Lyons, J.R. and Zhou, C.M. (2008) Triple oxygen isotope evidence for elevated CO(2) levels after a Neoproterozoic glaciation. Nature 453, 504-506.

Bao, H.M. and Thiemens, M.H. (2000) Generation of O-2 from BaSO4 using a CO2-laser fluorination system for simultaneous analysis of delta O-18 and delta O-17. Anal. Chem. 72, 4029-4032.

Bedrane, S., Descorme, C. and Duprez, D. (2005) O-16/O-18 isotopic exchange: A powerful tool to investigate oxygen activation on M/CexZr1-xO2 catalysts. Applied Catalysis a-General 289, 90-96.

Bevan, D.J.M. (1955) Ordered Intermediate Phases in the System CeO2-Ce2O3. Journal of Inorganic & Nuclear Chemistry 1, 49-&.

Bevan, D.J.M. and Kordis, J. (1964) Mixed oxides of the type MO2 (FLUORITE)-M2O3 .1. oxygen dissociation pressures and phase relationships in the system CeO2-Ce2O3 at high temperatures. Journal of Inorganic & Nuclear Chemistry 26, 1509-1523.

Bigeleisen, J. and Goeppert-Mayer, M. (1947) Calculation OF Equilibrium Constants for Isotopic Exchange Reactions. J. Chem. Phys. 15, 261-267.

Bigeleisen, J. and Wolfsberg, M. (1958) Theoretical and Experimental Aspects of Isotope Effects in Chemical Kinetics. Advances in Chemical Physics 1, 15-76.
Blanchard, M., Poitrasson, F., Meheut, M., Lazzeri, M., Mauri, F. and Balan, E. (2009) Iron isotope fractionation between pyrite (FeS2), hematite (Fe2O3) and siderite (FeCO3): A first-principles density functional theory study. Geochimica Et Cosmochimica Acta 73, 6565-6578.
Blum, J.D., Sherman, L.S. and Johnson, M.W. (2014) Mercury Isotopes in Earth and Environmental Sciences, in: Jeanloz, R. (Ed.), Annual Review of Earth and Planetary Sciences, Vol 42. Annual Reviews, Palo Alto, pp. 249-269.
Bouwmeester, H.J.M., Song, C.L., Zhu, J.J., Yi, J.X., Annaland, M.V. and Boukamp, B.A. (2009) A novel pulse isotopic exchange technique for rapid determination of the oxygen surface exchange rate of oxide ion conductors. Phys. Chem. Chem. Phys. 11, 9640-9643.
Cao, X.B. and Liu, Y. (2011) Equilibrium mass-dependent fractionation relationships for triple oxygen isotopes. Geochimica Et Cosmochimica Acta 75, 7435-7445.
Chueh, W. (2011) Electrochemical and Thermochemical Behavior of $CeO_{2-\delta}$. California Institute of Technology, Pasadena California, p. 172.
Chueh, W.C., Falter, C., Abbott, M., Scipio, D., Furler, P., Haile, S.M. and Steinfeld, A. (2010) High-flux solar-driven thermochemical dissociation of CO2 and H2O using nonstoichiometric ceria. Science 330, 1797-1801.
Chueh, W.C. and Haile, S.M. (2010) A thermochemical study of ceria: exploiting an old material for new modes of energy conversion and CO2 mitigation. Philos. Trans. R. Soc. A-Math. Phys. Eng. Sci. 368, 3269-3294.
Clayton, R.N. and Epstein, S. (1961) The Use of Oxygen Isotopes in High-Temperature Geological Thermometry. Journal of Geology 69, 447-452.
Cunningham, J., Cullinane, D., Farrell, F. and Gibson, C. (1999a) Oxygen isotope equilibration and exchange as probes for differing dioxygen interactions with pure and rhodia-promoted CeO2 and Al2O3. Top. Catal. 8, 179-187.
Cunningham, J., Farrell, F., Gibson, C. and McCarthy, J. (1999b) Oxygen-18 isotope exchange and equilibration processes over preoxidised and promoted ceria. Part I. (15)N(18)O((g)) or ((18)O(2)+(16)O(2(g))). Catal. Today 50, 429-443.
De Souza, R.A., Zehnpfenning, J., Martin, M. and Maier, J. (2005) Determining oxygen isotope profiles in oxides with Time-of-Flight SIMS. Solid State Ion. 176, 1465-1471.
Deines, P. (2003) A note on intra-elemental isotope effects and the interpretation of non-mass-dependent isotope variations. Chem. Geol. 199, 179-182.
Demoulin, O., Navez, M., Mugabo, J.L. and Ruiz, P. (2007) The oxidizing role of CO2 at mild temperature on ceria-based catalysts. Appl. Catal. B-Environ. 70, 284-293.
Dong, F., Suda, A., Tanabe, T., Nagai, Y., Sobukawa, H., Shinjoh, H., Sugiura, A., Descorme, C. and Duprez, D. (2004) Characterization of the dynamic oxygen migration over Pt/CeO_2-ZrO_2 catalysts by $^{18}O/^{16}O$ isotopic exchange reaction. Catal. Today 90, 223-229.
Duprez, D. (2006) Study of surface reaction mechanisms by $^{16}O/^{18}O$ and H/D isotopic exchange. Catal. Today 112, 17-22.
Elsner, M., Zwank, L., Hunkeler, D. and Schwarzenbach, R.P. (2005) A new concept linking observable stable isotope fractionation to transformation pathways of organic pollutants. Environmental Science & Technology 39, 6896-6916.

Esch, F., Fabris, S., Zhou, L., Montini, T., Africh, C., Fornasiero, P., Comelli, G. and Rosei, R. (2005) Electron localization determines defect formation on ceria substrates. Science 309, 752-755.
Farquhar, J., Bao, H.M. and Thiemens, M. (2000) Atmospheric influence of Earth's earliest sulfur cycle. Science 289, 756-758.
Fielitz, P. and Borchardt, G. (2001) On the accurate measurement of oxygen self-diffusivities and surface exchange coefficients in oxides via SIMS depth profiling. Solid State Ion. 144, 71-80.
Flynn, J.H. (1997) The 'temperature integral' - Its use and abuse. Thermochimica Acta 300, 83-92.
Galdikas, A., Duprez, D. and Descorme, C. (2004) A novel dynamic kinetic model of oxygen isotopic exchange on a supported metal catalyst. Appl. Surf. Sci. 236, 342-355.
Gibbs, G.V. (1982) Molecules as Models for Bonding in Silicates. American Mineralogist 67, 421-450.
Gorelov, G.P. and Kurumchin, E.K. (1987) Investigation of cerium dioxide by isotope exchange with molecular oxygen. Journal Name: Kinet. Catal. (Engl. Transl.); (United States); Journal Volume: 27:6; Other Information: Translated from Kinet. Katal.; 27: No. 6, 1346-1351(Nov-Dec 1986), Medium: X; Size: Pages: 1167-1173.
Graciani, J., Marquez, A.M., Plata, J.J., Ortega, Y., Hernandez, N.C., Meyer, A., Zicovich-Wilson, C.M. and Sanz, J.F. (2011) Comparative Study on the Performance of Hybrid DFT Functionals in Highly Correlated Oxides: The Case of CeO2 and Ce2O3. J. Chem. Theory Comput. 7, 56-65.
Heidenreich, J.E. and Thiemens, M.H. (1983) A Non-Mass-Dependent Isotope Effect in the Production of Ozone From Molecular-Oxygen. J. Chem. Phys. 78, 892-895.
Hirschi, J. and Singleton, D.A. (2005) The normal range for secondary Swain-Schaad exponents without tunneling or kinetic complexity. J. Am. Chem. Soc. 127, 3294-3295.
Hofmann, M.E.G., Horvath, B. and Pack, A. (2012) Triple oxygen isotope equilibrium fractionation between carbon dioxide and water. Earth and Planetary Science Letters 319, 159-164.
Hofmann, M.E.G. and Pack, A. (2010) Technique for High-Precision Analysis of Triple Oxygen Isotope Ratios in Carbon Dioxide. Anal. Chem. 82, 4357-4361.
Holmgren, A. and Andersson, B. (1998) Oxygen storage dynamics in Pt/CeO2/Al2O3 catalysts. J. Catal. 178, 14-25.
Holmgren, A., Duprez, D. and Andersson, B. (1999) A model of oxygen transport in Pt/ceria catalysts from isotope exchange. J. Catal. 182, 441-448.
Horvath, B., Hofmann, M.E.G. and Pack, A. (2012) On the triple oxygen isotope composition of carbon dioxide from some combustion processes. Geochimica Et Cosmochimica Acta 95, 160-168.
Huang, F., Chen, L.J., Wu, Z.Q. and Wang, W. (2013) First-principles calculations of equilibrium Mg isotope fractionations between garnet, clinopyroxene, orthopyroxene, and olivine: Implications for Mg isotope thermometry. Earth and Planetary Science Letters 367, 61-70.
Hulston, J.R. and Thode, H.G. (1965) Variations In S33 S34 And S36 Contents of Meteorites and Their Relation To Chemical and Nuclear Effects. Journal of Geophysical Research 70, 3475-&.

Inaba, H., Navrotsky, A. and Eyring, L. (1981) A thermochemical study of the phase reaction (1/7)Pr7O12 + (1/7 - X-2)O2 = PrO2-X. J. Solid State Chem. 37, 67-76.
Kamber, B.S. (2010) Archean mafic-ultramafic volcanic landmasses and their effect on ocean atmosphere chemistry. Chem. Geol. 274, 19-28.
Katsuki, M., Wang, S.R., Yasumoto, K. and Dokiya, M. (2002) The oxygen transport in Gd-doped ceria. Solid State Ion. 154, 589-595.
Killingsworth, B.A., Hayles, J.A., Zhou, C.M. and Bao, H.M. (2013) Sedimentary constraints on the duration of the Marinoan Oxygen-17 Depletion (MOSD) event. Proceedings of the National Academy of Sciences of the United States of America 110, 17686-17690.
Kilner, J.A., Skinner, S.J. and Brongersma, H.H. (2011) The isotope exchange depth profiling (IEDP) technique using SIMS and LEIS. Journal of Solid State Electrochemistry 15, 861-876.
Kim, S.T. and O'Neil, J.R. (1997) Equilibrium and nonequilibrium oxygen isotope effects in synthetic carbonates. Geochimica Et Cosmochimica Acta 61, 3461-3475.
Klier, K., Novakova, J. and Jiru, P. (1963) Exchange reactions of oxygen between oxygen molecules and solid oxides. J. Catal. 2, 479-484.
Klinman, J.P. (2003) Dynamic barriers and tunneling. New views of hydrogen transfer in enzyme reactions. Pure Appl. Chem. 75, 601-608.
Knauth, L.P. and Epstein, S. (1976) Hydrogen and Oxygen Isotope Ratios In Nodular And Bedded Cherts Geochimica Et Cosmochimica Acta 40, 1095-1108.
Knauth, L.P. and Lowe, D.R. (2003) High Archean climatic temperature inferred from oxygen isotope geochemistry of cherts in the 3.5 Ga Swaziland Supergroup, South Africa. Geological Society of America Bulletin 115, 566-580.
Kotaka, M., Okamoto, M. and Bigeleisen, J. (1992) Anomalous Mass Effects In Isotopic Exchange Equilibria J. Am. Chem. Soc. 114, 6436-6445.
Laachir, A., Perrichon, V., Badri, A., Lamotte, J., Catherine, E., Lavalley, J.C., Elfallah, J., Hilaire, L., Lenormand, F., Quemere, E., Sauvion, G.N. and Touret, O. (1991) Reduction of CeO2 by hydrogen - magnetic-susceptibility and Fourier-transform infared, ultraviolet and x-ray photoelecrton-spectroscopy measurements. J. Chem. Soc.-Faraday Trans. 87, 1601-1609.
Lahaye, J., Boehm, S., Chambrion, P. and Ehrburger, P. (1996) Influence of cerium oxide on the formation and oxidation of soot. Combust. Flame 104, 199-207.
Lane, J.A. and Kilner, J.A. (2000) Oxygen surface exchange on gadolinia doped ceria. Solid State Ion. 136, 927-932.
Lecuyer, C., Amiot, R., Touzeau, A. and Trotter, J. (2013) Calibration of the phosphate delta O-18 thermometer with carbonate-water oxygen isotope fractionation equations. Chem. Geol. 347, 217-226.
Levin, N.E., Raub, T.D., Dauphas, N. and Eiler, J.M. (2014) Triple oxygen isotope variations in sedimentary rocks. Geochimica Et Cosmochimica Acta 139, 173-189.
Li, S.N., Levin, N.E. and Chesson, L.A. (2015) Continental scale variation in O-17-excess of meteoric waters in the United States. Geochimica Et Cosmochimica Acta 164, 110-126.
Li, X.F. and Liu, Y. (2015) A theoretical model of isotopic fractionation by thermal diffusion and its implementation on silicate melts. Geochimica Et Cosmochimica Acta 154, 18-27.
Longinel.A and Nuti, S. (1973) Revised Phosphate-Water Isotopic Temperature Scale Earth and Planetary Science Letters 19, 373-376.

Madier, Y., Descorme, C., Le Govic, A.M. and Duprez, D. (1999) Oxygen mobility in CeO2 and CexZr(1-x)O2 compounds: Study by CO transient oxidation and O-18/O-16 isotopic exchange. J. Phys. Chem. B 103, 10999-11006.
Mahata, S., Bhattacharya, S.K., Wang, C.H. and Liang, M.C. (2012) An improved CeO2 method for high-precision measurements of 17O/16O ratios for atmospheric carbon dioxide. Rapid Communications in Mass Spectrometry 26, 1909-1922.
Manning, P.S., Sirman, J.D. and Kilner, J.A. (1997) Oxygen self-diffusion and surface exchange studies of oxide electrolytes having the fluorite structure. Solid State Ion. 93, 125-132.
Matatov-Meytal, Y.I. and Sheintuch, M. (1998) Catalytic abatement of water pollutants. Ind. Eng. Chem. Res. 37, 309-326.
Meheut, M., Lazzeri, M., Balan, E. and Mauri, F. (2007) Equilibrium isotopic fractionation in the kaolinite, quartz, water system: Prediction from first-principles density-functional theory. Geochimica Et Cosmochimica Acta 71, 3170-3181.
Namai, Y., Fukui, K. and Iwasawa, Y. (2003) Atom-resolved noncontact atomic force microscopic observations of CeO2(111) surfaces with different oxidation states: Surface structure and behavior of surface oxygen atoms. J. Phys. Chem. B 107, 11666-11673.
O'Neil, J.R., Clayton, R.N. and Mayeda, T.K. (1969) Oxygen Isotope Fractionation in Divalent Metal Carbonates. J. Chem. Phys. 51, 5547-&.
Otake, T., Lasaga, A.C. and Ohmoto, H. (2008) Ab initio calculations for equilibrium fractionations in multiple sulfur isotope systems. Chem. Geol. 249, 357-376.
Pack, A., Gehler, A. and Sussenberger, A. (2013) Exploring the usability of isotopically anomalous oxygen in bones and teeth as paleo-CO2-barometer. Geochimica Et Cosmochimica Acta 102, 306-317.
Pack, A. and Herwartz, D. (2014) The triple oxygen isotope composition of the Earth mantle and understanding Delta O-17 variations in terrestrial rocks and minerals. Earth and Planetary Science Letters 390, 138-145.
Pack, A. and Herwartz, D. (2015) Observation and interpretation of Delta O-17 variations in terrestrial rocks - Response to the comment by Miller et al. on the paper by Pack & Herwartz (2014). Earth and Planetary Science Letters 418, 184-186.
Palmer, M.S., Neurock, M. and Olken, M.M. (2002) Periodic density functional theory study of the dissociative adsorption of molecular oxygen over La2O3. J. Phys. Chem. B 106, 6543-6547.
Paparazzo, E., Ingo, G.M. and Zacchetti, N. (1991) X-ray-induced reduction effects at CeO2 surfaces - an x-ray photoelectron-spectroscopy study. J. Vac. Sci. Technol. A 9, 1416-1420.
Park, H.J. and Choi, G.M. (2008) The electrical conductivity and oxygen permeation of ceria with alumina addition at high temperature. Solid State Ion. 178, 1746-1755.
Passey, B.H., Hu, H.T., Ji, H.Y., Montanari, S., Li, S.N., Henkes, G.A. and Levin, N.E. (2014) Triple oxygen isotopes in biogenic and sedimentary carbonates. Geochimica Et Cosmochimica Acta 141, 1-25.
Perkins, C.L., Henderson, M.A., Peden, C.H.F. and Herman, G.S. (2001) Self-diffusion in ceria. J. Vac. Sci. Technol. A 19, 1942-1946.
Perrichon, V., Laachir, A., Bergeret, G., Frety, R., Tournayan, L. and Touret, O. (1994) Reduction of cerias with different textures by hydrogen and their reoxidation by oxygen. J. Chem. Soc.-Faraday Trans. 90, 773-781.

Purdy, M.M., Koo, L.S., de Montellano, P.R.O. and Klinman, J.P. (2006) Mechanism of O-2 activation by cytochrome P450cam studied by isotope effects and transient state kinetics. Biochemistry 45, 15793-15806.
R Core Team (2012) R: A Language and Environment for Statistical Computing. R Foundation for Statistical Computing.
RCoreTeam (2012) R: a language and environment for statistical computing. R Foundation for Statistical Computing.
Richet, P., Bottinga, Y. and Javoy, M. (1977) Review of Hydrogen, Carbon, Nitrogen, Oxygen, Sulfur, and Chlorine Stable Isotope Fractionation Among Gaseous Molecules Annual Review of Earth and Planetary Sciences 5, 65-110.
Rustad, J.R., Casey, W.H., Yin, Q.Z., Bylaska, E.J., Felmy, A.R., Bogatko, S.A., Jackson, V.E. and Dixon, D.A. (2010) Isotopic fractionation of Mg2+(aq), Ca2+(aq), and Fe2+(aq) with carbonate minerals. Geochimica Et Cosmochimica Acta 74, 6301-6323.
Ruszczycky, M.W. and Anderson, V.E. (2006) Interpretation of V/K isotope effects for enzymatic reactions exhibiting multiple isotopically sensitive steps. Journal of Theoretical Biology 243, 328-342.
Sadovskaya, E.M., Ivanova, Y.A., Pinaeva, L.G., Grasso, G., Kuznetsova, T.G., van Veen, A., Sadykov, V.A. and Mirodatos, C. (2007) Kinetics of oxygen exchange over CeO2-ZrO2 fluorite-based catalysts. Journal of Physical Chemistry A 111, 4498-4505.
Salazar-Villalpando, M.D. (2012) Syn-gas generation in the absence of oxygen and isotopic exchange reactions over Rh & Pt/doped-ceria catalysts. Int. J. Hydrog. Energy 37, 2121-2128.
Sasaki, K. and Maier, J. (1999) Low temperature defect chemistry of oxides. J. European Ceram. Soc. 19, 741-745.
Schauble, E.A. (2011) First-principles estimates of equilibrium magnesium isotope fractionation in silicate, oxide, carbonate and hexaaquamagnesium(2+) crystals. Geochimica Et Cosmochimica Acta 75, 844-869.
Sharma, S., Hilaire, S., Vohs, J.M., Gorte, R.J. and Jen, H.W. (2000) Evidence for oxidation of ceria by CO2. J. Catal. 190, 199-204.
Sharp, Z.D., Gibbons, J.A., Maltsev, O., Atudorei, V., Pack, A., Sengupta, S., Shock, E.L. and Knauth, L.P. (2016) A calibration of the triple oxygen isotope fractionation in the SiO2–H2O system and applications to natural samples. Geochimica et Cosmochimica Acta 186, 105-119.
Sharp, Z.D. and Kirschner, D.L. (1994) Quartz-Calcite Oxygen-Isotope Thermometry - A Calibrtion Based on Natural Isotopic Variations. Geochimica Et Cosmochimica Acta 58, 4491-4501.
Shirk, D.G. and Hoffman, N.M. (1985) Monte-Carlo error analysis in x-ray spectral deconvolution. Review of Scientific Instruments 56, 809-811.
Singh, P. and Hegde, M.S. (2010) Ce0.67Cr0.33O2.11: a new low-temperature O-2 evolution material and H-2 generation catalyst by thermochemical splitting of water. Chemistry of Materials 22, 762-768.
Skaron, S. and Wolfsberg, M. (1980) Anomalies In The Fractionation By Chemical-Equilibrium of O-18-O-16 Relative To O-17-O-16 J. Chem. Phys. 72, 6810-6811.
Stan, M., Zhu, Y.T., Jiang, H. and Butt, D.P. (2004) Kinetics of oxygen removal from ceria. J. Appl. Phys. 95, 3358-3361.
Staudt, T., Lykhach, Y., Tsud, N., Skala, T., Prince, K.C., Matolin, V. and Libuda, J. (2010) Ceria reoxidation by CO2: A model study. J. Catal. 275, 181-185.

Swain, C.G., Stivers, E.C., Reuwer, J.F. and Schaad, L.J. (1958) Use of Hydrogen Isotope Effects To Identify the Attacking Nucleophile In The Enolization of Ketones Catalyzed By Acetic Acid. J. Am. Chem. Soc. 80, 5885-5893.
Trovarelli, A. (1996) Catalytic properties of ceria and CeO2-containing materials. Catal. Rev.-Sci. Eng. 38, 439-520.
Trovarelli, A., Boaro, M., Rocchini, E., de Leitenburg, C. and Dolcetti, G. (2001) Some recent developments in the characterization of ceria-based catalysts. J. Alloy. Compd. 323, 584-591.
Trovarelli, A., de Leitenburg, C., Boaro, M. and Dolcetti, G. (1999) The utilization of ceria in industrial catalysis. Catal. Today 50, 353-367.
Urey, H.C. (1947) The Thermodynamic Properties of Isotopic Substances Journal of the Chemical Society, 562-581.
Valley, J.W., Kitchen, N., Kohn, M.J., Niendorf, C.R. and Spicuzza, M.J. (1995) UWG-2, a garnet standard for oxygen isotope ratios: Strategies for high precision and accuracy with laser heating. Geochimica Et Cosmochimica Acta 59, 5223-5231.
Van Orman, J.A. and Crispin, K.L. (2010) Diffusion in oxides, in: Zhang, Y.X., Cherniak, D.J. (Eds.), Diffusion in Minerals and Melts. Mineralogical Soc Amer, Chantilly, pp. 757-825.
Viney, I.E. (1933) Asymptotic expansions of the expressions for the partition function and the rotational specific heat of a rigid polyatomic molecule for high temperatures. Proceedings of the Cambridge Philosophical Society 29, 142-148.
Vyazovkin, S. and Wight, C.A. (1998) Isothermal and non-isothermal kinetics of thermally stimulated reactions of solids. International Reviews in Physical Chemistry 17, 407-433.
Waldhausl, J., Preis, W. and Sitte, W. (2012) Electrochemical characterization of gadolinia-doped ceria using impedance spectroscopy and dc-polarization. Solid State Ion. 225, 453-456.
Walsh, A., Woodley, S.M., Catlow, C.R.A. and Sokol, A.A. (2011) Potential energy landscapes for anion Frenkel-pair formation in ceria and india. Solid State Ion. 184, 52-56.
Wang, H.Y., Schneider, W.F. and Schmidtt, D. (2009) Intermediates and spectators in O_2 dissociation at the RuO_2(110) surface. J. Phys. Chem. C 113, 15266-15273.
Wang, Y.L., Wang, Y. and Xia, C.R. (2012) Surface process of doped ceria reduction by electrical conductivity relaxation. J. Electrochem. Soc. 159, F570-F576.
Wang, Z., Schauble, E.A. and Eiler, J.M. (2004) Equilibrium thermodynamics of multiply substituted isotopologues of molecular gases. Geochimica et Cosmochimica Acta 68, 4779-4797.
Wolfsburg, M. (1969) Correction To Effect of Anharmonicity on Isotopic Exchange Equilibria Advances in Chemistry Series, 185-&.
Wolfsburg, M. (1972) Theoretical Evaluation of Experimentally Observed Isotope-Effects. Accounts of Chemical Research 5, 225-&.
Wolfsburg, M., Van Hook, A.W., Paneth, P. and Rebelo, L.P.N. (2010) Isotope effects: in the chemical, geological, and bio sciences. Springer.
Yashiro, K., Onuma, S., Kaimai, A., Nigara, Y., Kawada, T., Mizusaki, J., Kawamura, K., Horita, T. and Yokokawa, H. (2002) Mass transport properties of Ce0.9Gd0.1O2-delta at the surface and in the bulk. Solid State Ion. 152, 469-476.
Young, E.D., Galy, A. and Nagahara, H. (2002) Kinetic and equilibrium mass-dependent isotope fractionation laws in nature and their geochemical and cosmochemical significance. Geochimica Et Cosmochimica Acta 66, 1095-1104.

Young, E.D., Kohl, I.E., Warren, P.H., Rubie, D.C., Jacobson, S.A. and Morbidelli, A. (2016) Oxygen isotopic evidence for vigorous mixing during the Moon-forming giant impact. Science 351, 493-496.
Zhang, F., Wang, P., Koberstein, J., Khalid, S. and Chan, S.W. (2004) Cerium oxidation state in ceria nanoparticles studied with X-ray photoelectron spectroscopy and absorption near edge spectroscopy. Surf. Sci. 563, 74-82.
Zheng, Y.F. (1993) Calculation of Oxygen Isotope Fractionation in Anhydrous Silicate Minerals. Geochimica Et Cosmochimica Acta 57, 1079-1091.
Zheng, Y.F. (1999) On calculations of oxygen isotope fractionation in minerals. Episodes 22, 99-106.
Zheng, Y.F. and Simon, K. (1991) Oxygen Isotope Fractionation In Hematite and Magnetite - A Theoretical Calculation and Application To Geothermometry of Metamorphic Iron-Formations European Journal of Mineralogy 3, 877-886.

VITA

Justin Hayles, a resident of Metairie, Louisiana, completed a Bachelors of Science in Geology at University of South Alabama. Afterwards Justin attended Louisiana State University to work under Huiming Bao where he earned a M.S. in Geology and decided to continue his work toward earning a PhD. During graduate school Justin maintained a 3.7 GPA. Justin has been an author on 6 studies and has presented his research at the AGU and Goldschmidt conferences. Justin has accepted a postdoctoral researcher position working on clumped isotopes at Rice University with Dr. Laurence Yeung.